

Università degli Studi Roma Tre

Dottorato di Ricerca in Fisica
XXII Ciclo (2006-2009)

***Ab initio* investigation of the structural and
electronic properties of TiO_2 nanostructures.**

Thesis for Doctor of Philosophy degree
submitted by Amilcare Iacomino

Supervisors:

Chia.mo Prof. Florestano Evangelisti

Chia.mo Prof. Domenico Ninno

Dr. Giovanni Cantele

Coordinator:

Chia.mo Prof. Guido Altarelli

Contents

Introduction	3
1 Theoretical framework of first-principles calculations	9
1.1 The quantum many-body problem	10
1.2 Density Functional Theory	12
1.2.1 The electron density as fundamental variable	13
1.2.2 The Kohn-Sham equations	15
1.2.3 Approximations for the exchange-correlation energy	17
1.3 Basis representation and pseudopotentials	18
1.3.1 The pseudopotentials technique	20
1.4 Structural optimization	22
1.5 Modeling low dimensional systems	24
2 An overview of experimental techniques and measurements	27
2.1 Synthesis of TiO ₂ nanostructures	27
2.2 Structural determinations	31
2.2.1 X-ray electron diffraction on powders	31
2.2.2 Extended X-ray absorption fine structure	33
2.2.3 Transmission electron microscopy	36
2.2.4 Infrared spectroscopy	38
2.3 Electronic determinations	40
2.3.1 Ultraviolet-visible absorption measurements	41
2.3.2 Electron paramagnetic spectroscopy	43
2.4 Conclusion	45

3	TiO₂ 0D nanocrystals	47
3.1	Methodology	50
3.2	Results and discussion: structure	52
3.2.1	NCs volume	53
3.2.2	The bond lengths in the octahedron and distances of atomic pairs	54
3.3	Results and discussion: electronic properties	57
3.3.1	From crystal to NC	57
3.3.2	Effects of the surface coverage	60
3.3.3	Band gap	63
3.3.4	HOMO-LUMO states	65
3.4	Formation energies	68
3.5	Conclusions	70
4	TiO₂ 1D nanowires	73
4.1	Methodology	76
4.1.1	Computational details	76
4.1.2	NWs definition	77
4.2	Results and discussion: structure	80
4.2.1	Section area variations	81
4.2.2	Variations of the atomic distances	83
4.3	Results and discussion: electronic properties	85
4.3.1	Effects of the size reduction	85
4.3.2	Bands line-up	90
4.3.3	Pathways of reactions at the surface of the NWs	93
4.3.4	Hydrogen sensing ability of the NWs	96
4.4	Relative stability analysis	98
4.5	Conclusions	101
	Conclusions	105
	Bibliography	111

Introduction

Nanoscience constitutes a rapidly evolving branch of the modern scientific research due to the contemporary convergence of different interests. Firstly, the technological capabilities are nowadays at pace to constantly carry out new and unprecedented nanobased devices, nanoscaled assemblies of heterogeneous materials, and stand-alone nanostructures in a variety of arrangements. At the same time, state-of-the-art measurement techniques progressively succeed in revealing several properties of the nanomaterials thus drawing a general portrait of their features. Secondly, the evidence of the new and peculiar properties that materials show at the nanoscale with respect to their macroscopic counterparts opens up fascinating expectations to employ more and more optimized nanodevices in many fields of social and commercial relevance. Thirdly, the current theoretical research is developing practical tools to investigate reliable models of feasible nanostructures, thus standing as an effective asset to integrate, support, and organize the experimental bunch of results.

In this thesis we focused on the study of low dimensional titanium dioxide (TiO_2), which is worldwide acknowledged as an outstanding example of the deep impact that nanoscale manipulation can induce into the daily life and society. In fact, TiO_2 is a cheap and biocompatible semiconductor, well known for its striking photocatalytic performances in many reactions. The possibility to synthesize TiO_2 based materials in the nanometer scale paves the way to design new devices with enhanced efficiencies for, e.g. solar energy conversion of light (dye synthesized solar cells or DSSCs) [1], water splitting process for large scale hydrogen production (sustainable fuel) [2], selective inactivation of diseased tissues (decrement of side effects) [3, 4], manageable employment of self-cleaning coatings (art protection and ambient sterilization) [5, 6], efficient photodegradation of organic pollutants in waste water and air [7]. The list

is far to be completed since new applications show up with the progress in research [8, 9, 10, 11]. All these achievements rely on the efficient control and tuning of the peculiar properties emerging at nanoscale to ultimately enhance specific processes of interest.

Within the above mentioned general framework, this thesis is meant to contribute to a comprehensive study of the fundamental properties of TiO_2 zero-dimensional nanocrystals (0D NCs) and one-dimensional nanowires (1D NWs), through the analysis of the connection between our theoretical results and experimental findings available in the literature. We have performed first-principles calculations on both 0D NCs and 1D NWs based on the density functional theory (DFT), which is a powerful tool to obtain both structural and electronic informations from an ab-initio approach. Some properties of TiO_2 nanomaterials are still debated, since their unanimous understanding is subordinate to the ability to isolate and identify single processes in a variety of phenomena taking place at the same time, which is obviously a challenging task for the modern probing instruments and technology. Hence, one goal of this thesis is to shed light on some controversial properties of TiO_2 nanostructures. Furthermore, the second goal of this thesis is to outline a theoretical background of knowledge, readily available for the experimental designing of new TiO_2 nanomaterials and devices.

The first class of TiO_2 systems that we will consider is constituted by 0D NCs. There are many open questions about nanostructured TiO_2 , some of which will be addressed in this thesis. The reduction of sample size produces an unavoidable variation of the structural arrangement. Lattice parameters of the anatase crystal phase have been observed to expand in some cases or to contract in others [12], while the rutile phase and other metal oxides show a linear expansion on decreasing the particle size. The bulk coordination of Ti is preserved in internal NC cells but the surface truncation produces undercoordination, dangling bonds and surface tension whose effect is a local disorder [14]. Some experimental works have observed in the smallest nanosamples (< 5 nm) the variation of bond lengths and coordination numbers upon decreasing the NC size [14, 15, 16, 17, 18]. This suggests an influence of the surface on the overall structure. Reactive compounds in solution can change the NC morphology as proved by the restoring of the octahedral coordination for the surface Ti atoms after adsorption of radicals [15, 19]. Modern instruments face

a challenging task when dealing with the dislocation of atoms at the surface of nanoparticles, since usual methods, like XRD and LEED, are unable to handle such size confined samples. On the other hand, our DFT approach have already proved to give reliable results in describing TiO_2 atomic arrangements and dislocations [20], thus we will address the structural deformations by total energy optimizations of our model systems. We will show the influence that surface termination has in determining the overall crystallinity of the NCs and its effects on the local order of the bonds geometry, thus suggesting an interpretation of the experimental findings.

The anatase TiO_2 crystal is an indirect semiconductor. On a theoretical general ground, a decrease of the dimensions down to the nanometer scale makes the electron mean free path comparable with system size; thus, one would expect a quantum size effect to be measurable through the band gap blue shift. This shift is not always detectable in nanostructured TiO_2 : (i) some authors [21, 22, 23] observed the bulk gap for sample diameters down to 1.5 nm; (ii) others [10, 24, 25] measured a blue shift already in the range 5 – 10 nm; (iii) red shifts are also observed and mainly ascribed to the presence of surface oxygen vacancies, to adsorbates or dopants producing electronic states in the forbidden region [10]. The nature of the first allowed transition is still under debate as well, since a direct radiative decay blue shift of the band gap is advised [11, 22, 26]. We will show through the analysis of the electronic properties, that the structural arrangement and the surface coverage can deeply influence the overall electronic structure, thus hindering or highlighting the effects of size confinement.

TiO_2 is the best candidate for photovoltaic solar cell conversion of light and for water splitting with consequent hydrogen production on a large scale [1, 27]. These ambitious goals need a deep understanding of the interaction of TiO_2 with water and its constituents. The presence of a large hydration sphere surrounding TiO_2 nanoparticles is usually detected [28] and may play a fundamental role in photocatalysis. This hydration sphere is built up of different and non equivalent bonds between water and the TiO_2 surface, forming a multilayered wet sphere. On the other hand, early works directly focused on the TiO_2 -H surface interaction and doping of NCs have been reported very recently [29, 30]. Hence we decided to cover our bare systems with simple adsorbates (H_2 and H_2O), modeling surface configurations in presence of hydrogens and hydration. It is evident that the very numerous experi-

mental data on TiO_2 NCs produced a large variety of, often conflicting, results. The lack of a satisfactory and organic comprehension of many of the measured properties can certainly be ascribed to the TiO_2 own nature - very high reactivity toward the external environment, ability to sustain complex surface chemistry, O vacancies, etc. Our DFT approach is functional to consider single representative configurations of the NCs, thus allowing a direct characterization of the effects induced by one phenomenon at a time (i.e. oxygen desorption, hydrogen adsorption, etc.), accordingly to which we will show the trends of the overall properties.

The second class of TiO_2 systems that we will consider is constituted by 1D NWs. Actually, TiO_2 0D NCs and 1D NWs share the same benefits from having larger surface area, more active sites, and quantum confinement related properties which eventually lift the rates of their activity [31, 32, 33]. 1D nanotubes, nanorods, and NWs are sometimes polycrystalline assemblies of NCs [34], hence the elementary physical properties can overlap. The main feature that can distinguish TiO_2 1D nanostructures from their 0D counterpart is a better ability to transport (photo)generated charges away from possible (recombination) reaction sites, thus revealing the heavy attention they are receiving for applications in photovoltaic cells, sensors, electrodes, and optoelectronics [35].

Our theoretical investigation may fill the gap through the atomistic modeling of TiO_2 nanostructures, by proposing the fundamental understanding of the physical properties behind the observed mechanisms at the nanoscale. Despite the example of the well characterized 1D nanomaterials like silicon and carbon, a very scarce literature is directly focused on the study of TiO_2 1D nanostructures up to now [36, 37, 38, 39]. The aim of this thesis is to investigate the dependence of the structural, electronic, and stability properties of anatase TiO_2 NWs as functions of the surface coverage, of the diameter size, and of the morphology, within the framework of first-principles DFT calculations. We will define two types of NWs with different growth direction and exposed surfaces to account for the morphological dependent properties. For a given type of NW we will consider four diameter sizes to address the trends of the properties with the dimension and, at last, we will cover the surface of the NWs as in the case of 0D NCs to study the influence of adsorbates on the overall properties of the NWs. We will study some issues that are in common with 0D NCs, that is the structural deformations at the nanoscale, the expected size confinement

through the blue shift of the band gap, and the effects of the interaction with water derived adsorbates. Moreover, we will address specific aspects of 1D NWs that are still under investigation due to the actuality of the research in this field. The band gap blue shift due to the scaling of the dimension down to the nanometer range could contribute to improve the charge transfer between the NW and the reactive species if a proper line-up of the valence band maximum for holes or conduction band minimum for electrons, with respect to the redox couple potentials, is satisfied. We will elucidate the effect of the size, of the surface configuration, and of the morphology on the NW ability to photocatalyze reactions through the calculation of a unique line-up of the bands energies.

Another issue discussed in this thesis is related with the efficiency of TiO_2 NWs to support photocatalytic reactions and the charge transport of photoelectrons to external circuits (for photosensing and solar cells applications). Both mechanisms are linked to the nature of the charge density distribution of the states involved in the transfer of charges. In fact the probability of the charge transfer increases with the overlap between the donor/acceptor wave functions of the NW and the reactant. To support the transport of photoelectrons throughout the external circuit it is also necessary that conduction band channels flow inside the NW to lengthen the lifetime of charges by avoiding recombination centers, i.e. structural distortions, defects, and charge traps which are mainly located at the surface. We will address this issue through calculations of the density of states and of the charge density distribution of the states in the NWs.

The last important application under investigation deals with the possibility to employ TiO_2 NWs as hydrogen sensors. Experiments reveal that TiO_2 nanotubes [40, 41] and mesowires [42] show an increase of the conductance upon exposure to hydrogen gas, which can be of some orders of magnitude [43] and can lead to the highest variation of the electrical properties of a material, to any gas, ever shown [44]. The main mechanism is ascribed to the adsorption of the dissociated hydrogen molecules at the surface due to the high electrical variation, velocity, and reversibility of the sensing process [45]. We will study the effect of the hydrogen surface coverage on the electronic structure of our TiO_2 NWs to identify and predict their ability to detect hydrogen gas. We will also relate our results to the size and the morphology of the NWs, thus giving useful informations to take into account

when designing new TiO_2 nanodevices.

The thesis is organized as follows. In chapter 1, we present the main features of ab-initio calculations based on DFT, with an emphasis to the ability of modeling bulk structures as well as confined systems like nanostructures, through an opportune setting of the periodic conditions imposed to the system. In chapter 2, we give an overview of some experimental techniques (and related results) used to synthesize and characterize TiO_2 nanosamples. We pay particular attention to those findings that are still debated and to the works that have been compared and relied on throughout the thesis. In chapter 3, we present our ab-initio calculations on TiO_2 0D NCs, focusing on the variations of the structural and electronic properties induced by modeling different surface configurations. In chapter 4, we analyze the effects of the size reduction, surface coverage, and morphological arrangement on the structural and electronic properties of TiO_2 1D NWs, through first-principles calculations. Conclusive remarks and possible developments are discussed in the last section.

Chapter 1

Theoretical framework of first-principles calculations

In this chapter we summarize the fundamental aspects of the theoretical framework for the study of the structural and electronic properties of the nanostructures investigated in this thesis. The main properties of condensed matter are determined by the electrons whose cloud envelops much heavier nuclei. For the very simultaneous interaction of a large number of particles it is necessary to develop a powerful theoretical model which satisfies both the request of reliable approximations and of practicality. In this regard, the classical approximation of Born-Oppenheimer [46], simplifies the solution of the total Hamiltonian by decoupling the ionic and electronic degrees of freedom due to their large mass difference. We thus have to solve a Schrödinger equation for the electronic ground state where the ions are kept fixed and their positions are parameters. On the other hand the electronic total energy is an effective potential of the ionic Hamiltonian. However, at this stage, we have still the problem to handle a quantum many-body electronic system which can be hard not only to solve but also to store in the current advanced machine memories. To this purpose, the Density Functional Theory (DFT), introduced in the 60's by Hohenberg and Kohn [47, 48], allows to recast the electronic Hamiltonian in a more practical, self-consistent, and one-electron formulation which is based on an exact result even if resembling a Hartree mean-field calculation [49]. In the DFT the ground state density of a bound system of interacting electrons in an external

potential is proved to uniquely determine the potential. Hence, the ground state values of all the observables are uniquely determined by the exact ground state electron density. This result busts the possibility to develop an efficient method to study systems with a huge number of particles because we are left with the search of just one fundamental function (the electronic total density), depending on three total variables (the spatial coordinates), from which all the informations of interest can be extracted. This squeezes the much far complicated computational effort to solve the Schrödinger equations depending on all the electronic variables. There is only one problem still to be overcome which is an exact expression for the exchange-correlation functional, whose knowledge would give a complete exact self-consistent theory. Many formulations have been developed to approximate this term and the one used in this thesis will be discussed, namely the generalized gradient approximation. More practical approximations are needed to use the DFT in real calculations which however go beyond the theory in itself, as the basis representation of the functions. In this thesis we chose to use a plane-wave based code which is suited for extended crystal materials, but it brings a simple way to improve and control the accuracy of the calculations, that is the solely number of plane waves of the basis set. At last, the pseudopotential approximation allows to scale down the computational cost thanks to the fact the chemical bonds in real materials are essentially determined by the valence electrons. In the following we will illustrate the DFT framework and the plane-wave pseudopotential technique.

1.1 The quantum many-body problem

Nanostructures are considered quantum many-body systems (nuclei and electrons) within the condensed matter physics. A rigorous way of treating the Hamiltonian of a system of interacting bodies has been a problem for the scientific community before the advent of the quantum mechanics. A set of equations of motion that exactly solves the dynamics of such systems has been never introduced because of the simultaneous and independent effects produced by the forces. Quantum mechanics borrows and worsens this difficulty introducing non classical interactions. We need

to solve a nonrelativistic Hamiltonian of the general form¹

$$H = -\frac{\hbar^2}{2m} \sum_i \nabla_i^2 - \sum_\alpha \frac{\hbar^2}{2M_\alpha} \nabla_\alpha^2 + \sum_{i < j} \frac{e^2}{|r_i - r_j|} - \sum_{\alpha, i} \frac{Z_\alpha e^2}{|r_i - R_\alpha|} + \sum_{\alpha < \beta} \frac{Z_\alpha Z_\beta e^2}{|R_\alpha - R_\beta|}$$

where m and M_α are the electronic and ionic mass respectively, r_i and R_α are the positions of the i electron and the α ion, Z_α is the atomic number of the α ion. The total many-particle wave function of the system Ψ depends, simultaneously in general, on both the electronic coordinates $\mathbf{r} = \{r_1, r_2, \dots, r_N\}$ and the nuclear coordinates $\mathbf{R} = \{R_1, R_2, \dots, R_M\}$:

$$\Psi = \Psi(\mathbf{r}, \mathbf{R}) = \Psi(r_1, r_2, \dots, r_N, R_1, R_2, \dots, R_M).$$

There is no method to calculate the exact solution of this Hamiltonian, which in turn is gradually and differently approximated. The classical approximation of Born-Oppenheimer [46] is the most common and widely used assumption that allows to treat separately the ionic and electronic motions. It is based on the large mass difference between electrons and ions. From this simple consideration it follows that the motion of the ions is so slow on the electronic time scale that the latter can always be considered in their ground state for the given ionic positions at each instant. The ions can then be thought as being fixed while the electron move relatively to them and the total Hamiltonian can be adiabatically splitted in the sum of an electronic and an ionic part. The electronic Hamiltonian reads

$$H_e = -\frac{\hbar^2}{2m} \sum_i \nabla_i^2 + \sum_{i < j} \frac{e^2}{|r_i - r_j|} - \sum_{\alpha, i} \frac{Z_\alpha e^2}{|r_i - R_\alpha|}$$

whose eigenvalue problem is given by

$$H_e \Phi_n(\mathbf{r}, \mathbf{R}) = \varepsilon_n(\mathbf{R}) \Phi_n(\mathbf{r}, \mathbf{R}) \quad (1.1)$$

where all the ionic positions \mathbf{R} are parameters for the electronic eigenvalues and eigenfunctions. On the other hand, the ionic wave function $F(\mathbf{R})$ must satisfy the eigenvalue equation

¹For the sack of simplicity we will discard the vectorial notation (e.g. r instead of \vec{r}) and the spin variable will not be explicitly considered as it does not substantially affect the dissertation.

$$\left[-\sum_{\alpha} \frac{\hbar^2}{2M_{\alpha}} \nabla_{\alpha}^2 + \sum_{\alpha < \beta} \frac{Z_{\alpha} Z_{\beta} e^2}{|R_{\alpha} - R_{\beta}|} + \varepsilon_n(\mathbf{R}) \right] F(\mathbf{R}) = EF(\mathbf{R}) \quad (1.2)$$

where E is the eigenvalue of the total Hamiltonian H . Eq. (1.2) is obtained by neglecting the first and second derivative terms of $\Phi_n(\mathbf{r}, \mathbf{R})$ with respect to the ionic variables which determine the coupling between the ionic and electronic motion. The total wave function $\Psi(\mathbf{r}, \mathbf{R})$ of H can thus be written as a direct product of the electronic and ionic wave functions

$$\Psi(\mathbf{r}, \mathbf{R}) \approx \Phi_n(\mathbf{r}, \mathbf{R}) F(\mathbf{R})$$

and the problem is now shifted to the separate solution of the eigenvalue problems (1.1) and (1.2). Since the terms neglected in Eq. (1.2) are of the order of m/M_{α} the Born-Oppenheimer approximation is expected to be reliable for many materials and by separating the electronic and ionic motions it brings a useful simplification of the whole problem. The ionic Hamiltonian can be treated in a classical formalism while in the electronic Hamiltonian the effects of electron-ion interaction can be seen as the result of an external potential to the electronic cloud.

1.2 Density Functional Theory

There are three different approaches to solve the electronic Hamiltonian defined in Eq. (1.1): the Hartree-Fock method, the Thomas-Fermi theory [49], and the Density Functional Theory (DFT) [47]. It is possible to define an energy functional for each of them and obtain the respective equations within the variational formulation of Rayleigh-Ritz. Among these methods DFT excels because it is in principle an exact theory with the only source of error given by the explicit formulation of the unknown exchange-correlation functional. Although the DFT can be considered a generalization of the Thomas-Fermi theory it is defined in an independent and self-consistent formulation, which is nowadays the most accurate and spread method to obtain reliable results in the study of atomic, molecular, and crystalline systems.

1.2.1 The electron density as fundamental variable

Let us consider a system of N electrons moving in an external potential $v(r)$ and subjected to their reciprocal coulombian repulsion U . The Hamiltonian of the system can be written as $H = T + U + V$, where $V(r_1, \dots, r_N) = \sum_{i=1}^N v(r_i)$. If $\Psi(r_1, \dots, r_N)$ is the (normalized and, for simplicity, non degenerate) ground state then the density can be written as

$$n(r) = N \int \Psi^*(r, r_1, \dots, r_{N-1}) \Psi(r, r_1, \dots, r_{N-1}) dr_1 \dots dr_{N-1}$$

where both Ψ and $n(r)$ are obviously functional of $v(r)$. Thus the following relation stands

$$\int \Psi^*(r, r_1, \dots, r_{N-1}) v(r) \Psi(r, r_1, \dots, r_{N-1}) dr dr_1 \dots dr_{N-1} = \int v(r) n(r) dr.$$

The most important result of DFT is that **$v(r)$ and Ψ are uniquely determined by the knowledge of $n(r)$** (more precisely $v(r)$ is known within a trivial constant) as follows from the traditional formulation of the theorems of Hohenberg and Kohn (HK):

First theorem of Hohenberg and Kohn

The ground state density² $\rho(r)$ of a many-electron system (atom, molecule, solid) in presence of an external potential V_{ext} uniquely determines the external potential. An immediate consequence is that the ground-state expectation value of any observable \hat{O} is a unique functional of the exact ground-state electron density:

$$\langle \psi | \hat{O} | \psi \rangle = O[\rho].$$

Second theorem of Hohenberg and Kohn

For \hat{O} being the Hamiltonian \hat{H}_e , the ground-state total energy functional $H_e[\rho] \equiv E_{V_{ext}}[\rho]$ is of the form:

²The density $\rho(r)$ is obtained as the expectation value of the density operator $\hat{\rho}$, defined as $\hat{\rho} = \sum_{i=1}^k \delta(r_i - r)$. In this way, the ground-state density $\rho(r)$ becomes $\rho(r) = \langle \psi | \hat{\rho} | \psi \rangle = \sum_{i=1}^k \int \psi^*(r_1, r_2, \dots, r_i \equiv r, \dots, r_k) \psi(r_1, r_2, \dots, r_i \equiv r, \dots, r_k) dr_1 dr_2 \dots \cancel{dr_i} \dots dr_k$

$$E_{ext}[\rho] = \langle \Psi | \hat{T} + \hat{V}_{e-e} | \Psi \rangle + \langle \Psi | \hat{V}_{ext} | \Psi \rangle = F[\rho] + \int \rho(r) V_{ext}(r) dr$$

where the HK density functional $F[\rho]$ is universal for any many-electron system. E_{ext} reaches its minimal value (equal to the ground-state total energy) for the ground-state density corresponding to V_{ext} .

We stress here some interesting points that follow from these theorems. (i) The request of non degeneracy of the ground state can be easily removed. (ii) The electronic density must be v -representable, that is given a $v(r)$ there must exist at least a potential $v(r)$ and hence an Hamiltonian H whose ground state density is right $n(r)$. (iii) The one-to-one correspondence between the ground state density and the external potential contains the great potentiality of the theory. Intuitively we could be inclined to assert that the total electronic density brings less informations than the set of wave functions of the electrons. DFT proves that this is not the case. In the ground state, the electronic wave functions are functionals of the whole electronic density. Hence if we can obtain the density we can extract all the informations we need. (iv) The functional $F[\rho]$ does not contain information on the nuclei and their positions. Thus a universal expression must exist which can be used regardless of the particular system under investigation, that is for any atom, molecule, solid. Furthermore, it follows that the contribution to the total energy of the external potential can be calculated exactly. (v) A variational access to the ground state density follows from the second theorem. The true ground state density must minimize the total energy $E_{V_{ext}}[\rho]$ of the system with an external potential V_{ext} . Thus, if we were able to formalize $F[n(r)]$, defined by the sum of the kinetic and the coulombian interaction,

$$F[n(r)] \equiv \langle \Psi | T + U | \Psi \rangle \tag{1.3}$$

as a simple function of $n(r)$ then the search for the ground state of a system subjected to a given external potential would be reduced to the minimization of a functional of the density. The goal to give an operative form to the, otherwise useless, DFT was achieved by Kohn and Sham [48].

1.2.2 The Kohn-Sham equations

In 1965 Kohn and Sham(KS) were intended to obtain, starting from the HK formalism, a set of equations on the Hartree model style but also including all the many-body effects in a formally exact way. They extracted from the universal functional $F[n(r)]$ in Eq. (1.3) the classical coulombian energy

$$G[n] \equiv F[n] - \frac{1}{2} \int \frac{n(r)n(r')}{|r - r'|} dr dr' \quad (1.4)$$

and defined the exchange-correlation energy functional as

$$E_{xc}[n(r)] \equiv G[n(r)] - T_s[n(r)] \quad (1.5)$$

where $T_s[n(r)]$ is the kinetic energy functional of a noninteracting system of electrons. The total energy functional can thus be written as

$$E_v[n'(r)] = T_s[n'(r)] + \int v_{ext}(r)n'(r)dr + \frac{1}{2} \int \frac{n'(r)n'(r')}{|r - r'|} dr dr' + E_{xc}[n'(r)]. \quad (1.6)$$

Although $T_s[n'(r)]$ is not the true kinetic energy of the interacting system, it is of the same order of magnitude and it is also treated in a exact way following its definition in Eq. (1.5). If we neglect the last term of Eq. (1.6), the problem of minimizing E_v with respect to n' would be equivalent to the minimization of a Hartree energy. It is known that the Hartree method gives a better description of atomic systems than the Thomas-Fermi. This is due to the different treatment of the kinetic term. Hence it is clear that the underlying idea of Eq. (1.6) is to produce reliable estimates of the kinetic and electron-electron interaction energies, in so doing retaining all the error in the exchange-correlation part and allowing an exact treatment of all the terms apart the exchange-correlation one. If we now minimize the total energy $E_v[n'(r)]$ with the charge conservation condition

$$\int n'(r)dr = N, \quad (1.7)$$

we obtain the following equation

$$\frac{\delta T_s[n'(r)]}{\delta n'(r)} + \phi(r) + v_{xc}(r) - \mu = 0, \quad (1.8)$$

where $\phi(r)$ is the classical potential energy

$$\phi(r) \equiv v_{ext}(r) + \int \frac{n'(r')}{|r - r'|} dr', \quad (1.9)$$

$v_{xc}(r)$ is the functional derivative

$$v_{xc}(r) \equiv \frac{\delta E_{xc}[n'(r)]}{\delta n'(r)}, \quad (1.10)$$

and μ is the Lagrange multiplier associated to Eq. (1.7). If the particles were non interacting then Eq. (1.7) and (1.8) would be solved with respect to the density by extracting the latter from a set of independent and single particle Schrödinger equations, subjected to an external potential $v_{ext}(r)$. On the other hand, for interacting electrons we can still retain such a set of equations if we identify the external potential with an effective potential $v_{eff} = \phi(r) + v_{xc}(r)$. Hence, given $\phi(r)$ and $v_{xc}(r)$, the density that satisfies Eq. (1.7) and (1.8) is the same as the one obtained by solving the single particle Schrödinger equations

$$\left[-\frac{\hbar^2}{2m} \nabla^2 + v_{eff}(r) \right] \Psi_i(r) = \varepsilon_i \Psi_i(r) \quad (1.11)$$

with the constrain

$$n(r) = \sum_{i=1}^N |\Psi_i(r)|^2, \quad (1.12)$$

for N total numbers of electrons. Eq. (1.11) and (1.12) are the so called **Kohn-Sham self-consistent equations**. The potential $v_{eff}(r)$ can be seen as the only external (fictitious) potential of a system of noninteracting electrons which gives rise to the same potential of a system of interacting electrons subjected to the external potential $v(r)$. Therefore, if $n(r)$ was independently known (for instance, based on experiments or on accurate wave functions calculations of simple molecules) then $v_{eff}(r)$ and so $v_{xc}(r)$ would be directly derivable from $n(r)$. The many-electron problem is thus reduced to a single particle one with an appropriate choice of the functional $F[n(r)]$. This is in practice a notably computational simplification, not that different from a Hartree calculation. At variance with the latter, the KS equations

introduce the exchange-correlation term in a formally exact way through $v_{eff}(r)$. At last, to obtain the total energy from the KS equations it is possible to note that

$$\sum_i \varepsilon_i = \sum_i \langle \Psi_i | \left[-\frac{1}{2} \nabla^2 + v_{eff}(r) \right] | \Psi_i \rangle = T_s[n(r)] + \int v_{eff}(r) n(r) dr \quad (1.13)$$

thus, from Eq. (1.6) it follows that

$$E = \sum_i \varepsilon_i - \frac{1}{2} \int \frac{n(r)n(r')}{|r - r'|} dr dr' + E_{xc}[n(r)] - \int v_{xc}(r) n(r) dr. \quad (1.14)$$

The KS equations can be iteratively and self-consistently solved. The solution of the KS equations gives the occupied and empty states eigenvalues ε_i . In general nor the KS eigenvalues nor the eigenfunctions have proved physical meanings. The only exception to this statement is the highest occupied eigenvalue of the extended state of an infinite system, which is equal to the chemical potential of the system¹. The only physically meaningful quantity is the total electron density defined in Eq. (1.12).

1.2.3 Approximations for the exchange-correlation energy

The DFT is still exactly defined up to this point but its practical use depends on an explicit definition of the exchange-correlation energy, which is currently unknown. Hence we need to approximate the exchange-correlation functional in the KS equations starting from reasonable assumptions. The simplest definition of $E_{xc}[n(r)]$ is based on the assumption that the density in a given point in space r is a smooth function around this point. This is strictly true for a homogeneous electron gas for which the potential $v_{xc}(r)$ can be seen to depend on the local density but for a inhomogeneous electron gas it becomes a local density approximation (LDA), which is equivalent to cut E_{xc} at the first order of a functional Taylor expansion:

$$E_{xc}^{LDA} n(r) = \int \varepsilon(n(r)) n(r) dr, \quad (1.15)$$

¹This situation represents the analogous of the Koopmans theorem in the Hartree-Fock method.

where $\varepsilon(n(r))$ represents the exchange-correlation energy, per particle, of a homogeneous electron gas of density $n(r)$. In Eq. (1.15) the functional dependence has been substituted by a function dependence on the density because $v_{xc}(r)$ has been assumed to depend only on the value of the density at the point r :

$$v_{xc}^{LDA}(r) = \frac{d}{dn} \{ \varepsilon(n(r)) n(r) \}. \quad (1.16)$$

Although LDA is based on the assumption that the real density of the interacting electron system is a slowly varying function in space, it performs satisfactory well for many materials. Structural and vibrational properties are reproduced in agreement with experiments and even covalently bonded materials as well as some transition metals can be studied. An improvement over the LDA is given by considering the dependence of the exchange-correlation energy also on density variations, that is on the approximation of the density gradient (GGA):

$$E_{xc}^{GGA} = \int \varepsilon(n(r)) n(r) dr + \int f_{xc}(n(r), |\nabla n(r)|) n(r) dr, \quad (1.17)$$

where f_{xc} is a function of the two independent variables $n(r)$ and $|\nabla n(r)|$. GGA is found to improve the binding energy estimates and the description of more inhomogeneous materials, giving reliable results also in some cases where LDA completely fails. There is a certain arbitrariness in the explicit definition of the f_{xc} , among others the Perdew-Wang GGA functional (PW91) [50] has been used throughout the calculations of this thesis.

1.3 Basis representation and pseudopotentials

In practical computations the KS equations must be recast in a more algebraic form in order to be handled by the codes which actually perform the calculations. One way to achieve an efficient representation of all the operators and quantities to explicitly calculate is constituted by their expansion with an appropriate basis set of functions. Among all the available possibilities, we chose a plane waves representation as implemented in the Quantum-ESPRESSO package [51]. Although the system models presented in this thesis are low dimensional TiO_2 nanostructures, the choice to use such a code is based on two main advantages: (i) the possibility to

control the accuracy of the calculated quantities in a simple way through the number of plane wave functions of the basis set; (ii) the possibility to compare, within the same computational framework, the low dimensional models on one hand and the extended TiO₂ bulk on the other hand. If the system to calculate is periodic in at least one dimension it is possible to take advantage of its symmetry properties to reduce the amount of calculations to be performed. In fact, we can use the Bloch theorem [49] to express a wave function in terms of periodic functions. For example, in the case of a crystal, the electron wave function in the i^{th} band, eigenfunction of the KS equations, can be written as

$$\Psi_i(r) = e^{ik \cdot r} u_i(r) \quad (1.18)$$

where k is the crystal momentum of the electron and $u_i(r)$ is a periodic function satisfying the relation $u_i(r) = u_i(r + R)$, R being a generic vector of the corresponding Bravais lattice. The periodic function $u_i(r)$ can be expanded by using a discrete basis set of plane waves whose wave vectors G are also vectors of the crystalline reciprocal lattice. Hence $R \cdot G = 2m\pi$ for integer m and for each R giving

$$u_i(r) = \sum_G c_{i,G} e^{iG \cdot r} \quad (1.19)$$

and the electron wave function reads

$$\Psi_i(r) = \sum_G c_{i,k+G} e^{i(k+G) \cdot r}. \quad (1.20)$$

The Bloch theorem transforms the problem of searching for an infinite number of electron wave functions (of an ideal crystal) into the problem of searching for a finite number of electron wave functions on an infinite number of k points. Furthermore, the expansion coefficients $c_{i,G}$ are typically more important for wave functions with low kinetic energy (hence with low $k + G$, being $T = (\hbar^2/2m)|k + G|^2$) such that it is possible to introduce a truncation of the G points of the plane waves basis set. The plane waves basis set becomes a finite ensemble within an appropriate cutoff energy. This procedure allows a simple control over the convergence of the meaningful physical quantities which is based on the increase of the number of k points in the reciprocal space and the increase of plane waves of the basis set.

By inserting expression (1.20) in the KS equations (1.11) and by integrating in real space, the KS equations get the simple form

$$\sum_{G'} \left[\frac{\hbar^2}{2m} |k + G|^2 \delta_{GG'} + v_{eff}(G - G') \right] c_{i,k+G'} = \varepsilon_i c_{i,k+G'}. \quad (1.21)$$

In this expression the kinetic energy is a diagonal term and the single particle effective potential v_{eff} is described by its Fourier transform in the reciprocal space. The solutions of Eq. (1.21) can be found by the diagonalization of the Hamiltonian matrix whose elements are enclosed in the square brackets. The availability of Fast Fourier Transform algorithms ensures a speed up of the calculation, resulting in another advantage of this procedure. The dimension of the matrix depends upon the number of plane waves of the basis set, thus upon the kinetic energy cutoff. At this stage, the number of plane waves necessary to get a satisfactory convergence of the important quantities can quickly become prohibitive for most of the systems of interest. This difficulty is actually overcome by using the pseudopotential method.

1.3.1 The pseudopotentials technique

Within the plane wave representation all the spatial regions in which we can think to divide the periodic cell have the same resolution. Thus around the nuclei, where we expect the functions to undergo notably variations, we have to consider a huge number of plane waves to get an acceptable convergence. To overcome this difficulty we can rely on the well known observation that many physical and chemical properties of materials are determined by the valence electrons much more than the core electrons. We can subtract to the explicit solution of the KS equations the core electrons by replacing their effects on the valence electrons with ionic potentials (given by the sum of the nuclei and their core electrons). Thus a generic coulomb potential $-Z/|r - R|$ felt by a valence electron is replaced by a more complicated expression which must include all the effects induced by the core electrons, which can be thought to be *frozen* in their atomic configuration around the nuclei. The effective potential felt by the valence electrons is a pseudopotential for two reasons: (i) it must reproduce the core-valence electrons interaction and the nucleus-valence electron one in the single particle scheme of the KS equations; (ii) it must also give smoother

wavefunctions in the region where core and valence electrons mostly overlap, that is around the nuclei. Since core and valence wavefunctions are required to be orthogonal, a region exists around the nuclei where the valence wavefunctions have many nodes. Hence we can divide the pseudopotential into two regions at an appropriate cutoff radius. In the inner part the valence wavefunctions are replaced by smoother pseudo-wavefunctions and outside the cutoff radius the pseudo-wavefunction and the single particle wavefunction must match. This is accomplished by a pseudopotential of the type

$$V^{ps}(r, r') = V_{loc}^{ps}(r)\delta(r - r') + \sum_i |\phi_i^{ps}\rangle V_i^{ps} \langle \phi_i^{ps}|, \quad (1.22)$$

where V_{loc}^{ps} accounts for the local part of the pseudopotential and V_i^{ps} is an operator dependent upon the angular momentum of the pseudo-wavefunction $|\phi_i^{ps}\rangle$ which gives rise to the nonlocality of the pseudopotential.

There are several procedures to define a pseudopotential, but they are all based on the same assumptions. In all the case we need an accurate all-electron calculation of the reference atomic configuration, whose spectrum and electron wavefunctions outside the core region must be reproduced by the pseudopotential based calculation. In this thesis we used pseudopotentials of the Vanderbilt type [52]. They are known as *ultrasoft* pseudopotentials since the charge conservation inside the core region is relaxed, thus allowing an arbitrary smoothness of the valence pseudo-wavefunction in this region. To increase the *transferability* of the pseudopotential (its ability to give reliable results regardless of the specific atomic configuration in the system) the energetic range of the occupied states is sampled by more than one reference atomic energy, thus in the nonlocal part of Eq. (1.22) the scattering properties of the pseudo-wavefunctions are improved by using more than one energy per given i . The resulting accuracy of the ultrasoft Vanderbilt pseudopotentials is practically equivalent to other much heavier pseudopotentials, but without the constrain of the charge conservation inside the core region it becomes possible to considerably decrease the number of plane waves of the basis set.

1.4 Structural optimization

In the previous sections we described the theory and some practical approximations to solve the electron Hamiltonian defined by Eq. (1.1). This is accomplished by an iterative and self-consistent procedure which is inserted into the searching for the ionic configuration of the ground state. In fact, as pointed out in Sec. 1.1, we have to solve the eigenvalue problem for the ions given by Eq. (1.2). Following the Born-Oppenheimer approximation and Eq. (1.2), the ions (nuclei and their respective core electrons) move on the potential energy surface (PES)

$$V^{BO}(\mathbf{R}) = \sum_{\alpha < \beta} \frac{Z_{\alpha} Z_{\beta} e^2}{|R_{\alpha} - R_{\beta}|} + \varepsilon_n(\mathbf{R}). \quad (1.23)$$

The ground state geometry of the system is obtained by minimizing the forces acting on the ions, that is by searching for the minimum of the PES. Hence we can calculate the forces acting on each ion by the energy gradient with respect to the ionic positions and construct an algorithm to find the ground state geometry by using the Hellman-Feynman theorem [53]:

Theorem of Hellman-Feynman *Let η be a parameter in the Hamiltonian \hat{H} , Ψ_{η} an eigenfunction of \hat{H} of energy E . Then,*

$$\frac{\partial E}{\partial \eta} = \left\langle \Psi_{\eta} \left| \frac{\partial \hat{H}}{\partial \eta} \right| \Psi_{\eta} \right\rangle. \quad (1.24)$$

In this case the parameter η is given by the set of ionic positions \mathbf{R} . Different techniques have been implemented to actually find the ground state geometry of the systems, all based on the Hellman-Feynman theorem. In this thesis we chose the Broyden-Fletcher-Goldfarb-Shanno (BFGS) procedure [54], which is a quasi-Newton method based on the calculation of an approximate Hessian matrix.

In Fig. 1.4 we show the flow-chart of the entire calculation, which summarizes the fundamental steps of the self-consistent approach in solving the total Hamiltonian and its electron and ionic parts. Starting from a given set of atomic positions in the unit cell and an initial guess of the electron density (generally obtained by a superposition of atomic orbitals), the electronic Hamiltonian is solved self-consistently due to the dependence of the effective potential on the density. The convergence of the

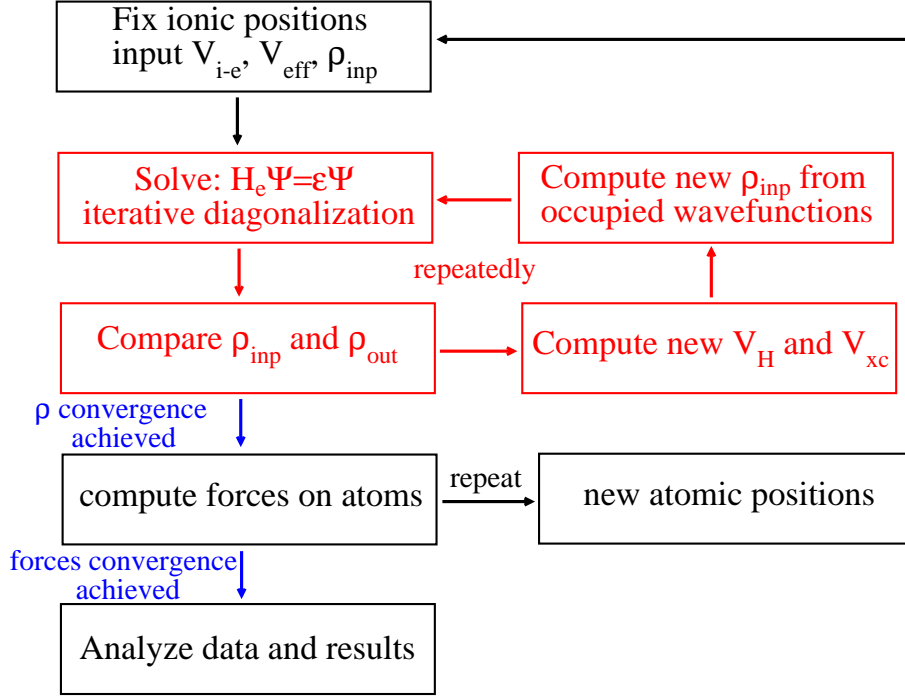


Figure 1.1: Self-consistent calculation flow chart. The electronic Hamiltonian is solved self-consistently and a new charge density is computed until convergence (red scheme). The structural optimization is achieved through the calculation of the forces acting on atoms. They are moved until the total force is less than the required threshold (black scheme).

electronic Hamiltonian is reached when the charge density difference between two consecutive steps is less than a given threshold. At this point, the ionic Hamiltonian is solved and the forces acting on atoms are computed. If these forces are higher than a given threshold, the ions are moved and a new set of coordinates determines the input ionic potential for a further electronic self-consistent calculation. When the forces acting on atoms are sufficiently low the computational process comes to end so that it is possible to extract the physical quantities of interest.

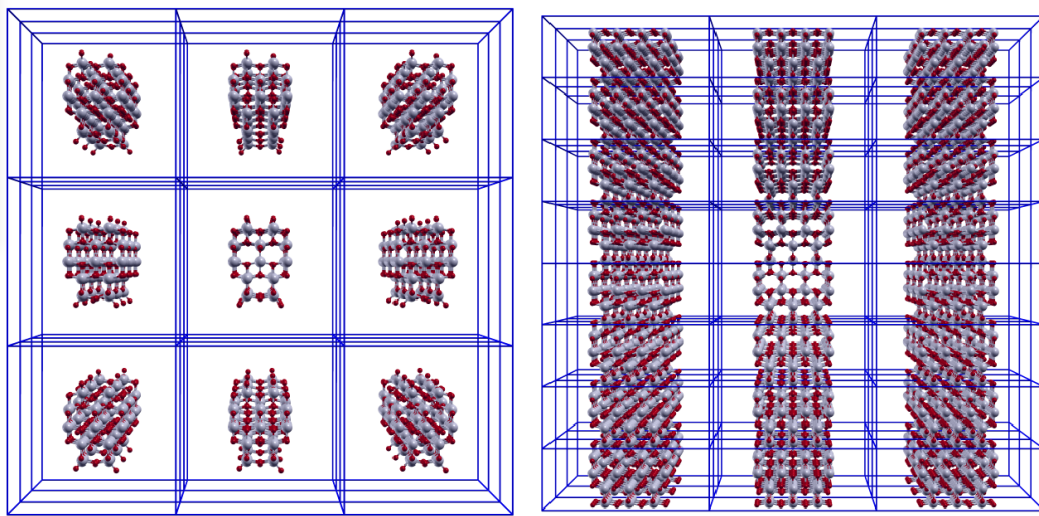


Figure 1.2: Pictures of the supercell approach. A vacuum region is introduced to avoid the interaction among the replica in neighbour cells. On the left a 0D TiO_2 cluster is surrounded by vacuum in each direction whereas on the right a 1D TiO_2 nanowire is surrounded by vacuum in the plane orthogonal to the growth direction.

1.5 Modeling low dimensional systems

The aim of this thesis is to present a detailed theoretical analysis of the properties of TiO_2 nanostructures, namely zero-dimensional clusters and one-dimensional nanowires (see Fig. 1.5). Thus their periodicity in real space is only present in the growth direction of the nanowires and absent in the clusters. In molecular chemistry, and within an *ab initio* framework, such systems are predominantly calculated by means of codes which do not require the periodicity properties to simplify the computational demand. A given system is calculated as a whole and all the atoms (and their valence electrons) are explicitly treated. However, this approach brings some limitations to the size of the system that can be practically handled. Most of the calculations are actually performed on molecules of less than two-three hundreds atoms (this number rapidly decreasing with increasing number of electrons per atom). Furthermore, the accuracy of the calculation is often based on a skilful treatment of the basis set of the wave functions that represent the physical quan-

tities. Each atom has usually its specific set of localized wave functions, that can be modified according to the system and/or environment in which the atoms are placed. Hence the control over the convergence of the calculated quantities is not straightforward and sometimes becomes tricky.

On the contrary, our choice to use a plane wave based code allows a simple control of the convergence of the calculated physical quantities by increasing the number of the vectors in the basis set. When a three dimensional crystal is modeled, it is possible to uptake the Bloch theorem and thus to extract from a macroscopic ensemble of atoms its irreducible basis. It is made up of far less atoms (in a typical range of one-two tens) than the real crystal, but the latter is completely reproduced by the periodic replication in space of the irreducible basis. In the case of low dimensional systems it is possible to retain this approach if a vacuum region in the directions of non periodicity of the system is introduced into the unit cell (see Fig. 1.5). This vacuum gap must ensure that the atoms in the unit cell (or *supercell*) do not interact with the neighbour replica, such that the system can actually be isolated.

Chapter 2

An overview of experimental techniques and measurements

In this chapter, we summarize the basic aspects of the experimental methods used to synthesized TiO_2 nanostructures through the description of those works we have relied on in this thesis. We also treat the experimental techniques used to measure both the structural and the electronic properties of these nanomaterials, paying particular attention to those works which have introduced still argued issues in the low dimensional physics of TiO_2 .

2.1 Synthesis of TiO_2 nanostructures

The synthesis of TiO_2 nanostructures can be achieved following different techniques. New methods and variations on the existing procedures are constantly introduced, essentially to optimize the control over the parameters involved in the reactions and the quality of the final nanosample. On one hand, the main general efforts are to speed up the whole process, to obtain stable nanomaterials, and to keep the production costs low. On the other hand, it is necessary to control the features of the products in terms of their crystallinity, morphology, optical properties, photocatalytic activity, and more generally to optimize those properties that are mandatory for a good outcome of the final application the nanosample are made for. These aspects are often contrasting since a sufficient control of a given feature

of the nanostructure (e.g. blue shift of the band gap) can be linked with the effort in controlling a specific parameter of the synthesis process (e.g. size). In the following we summarize the most implemented and spread synthesis techniques of TiO_2 , advising the reader to refer to specialized publications for a deeper understanding of these techniques [11, 8, 35, 55, 56]. An accurate description of the large variety of works in this field goes beyond the purpose of the thesis.

- *Sol-gel Method* is the most used technique to synthesize TiO_2 nanostructures. Generally, a colloidal suspension (sol) is formed from the hydrolysis and polymerization of reacting precursors, which are typically inorganic metal salts or metal alkoxides. After a complete polymerization takes place the solvent is lost, leading to the transition from the sol to the gel phase. In the case of TiO_2 nanoparticles (NCs) it is possible to obtain a thin film on a substrate by coating. When the sol is cast into a mold a wet gel will form and then converted into a dense ceramic with further heat treatment. On the other hand, by removing the solvent in the wet gel, a porous and low-density aerogel is obtained. In the case of TiO_2 one-dimensional nanostructures (1D NWs), an anodic aluminum oxide template is immersed into the sol suspension, so that the sol will aggregate on the template surface and fill the channels to form high aspect ratio structures. With this technique, it is possible to exploit the variations of the many parameters involved (reaction time, temperature, precursors, etc.) to vary the properties of the final nanosamples (shape, size, morphology, etc.). In Fig. 2.1 (a-c) we show the effect of varying the heating temperature and adsorbate species on the final morphology of the nanosamples.

- *Solution Method* is a nonhydrolytic sol-gel process that usually involves the reaction of titanium chloride with different oxygen donor molecules, as metal alkoxide and organic ether. As example, in the method used by Polleux *et al.* [57], TiCl_4 was slowly added to a mixture of anhydrous benzyl alcohol and a ligand under vigorous stirring at room temperature and was kept at 80 °C for 24 hours in the reaction vessel. The resulting suspension was centrifugated and the precipitate was washed with chloroform. The collected material was left to dry in air at 600 °C and finally ground into a fine powder. The NCs were then assembled to form TiO_2 NWs in distilled water and by refluxing for 24 hours under stirring, see Fig. 2.2 (a-c). C. Liu and S. Yang [58] have very recently modified this method to synthesize the thinnest TiO_2 NWs. They divided the process in a first step where the formation of the

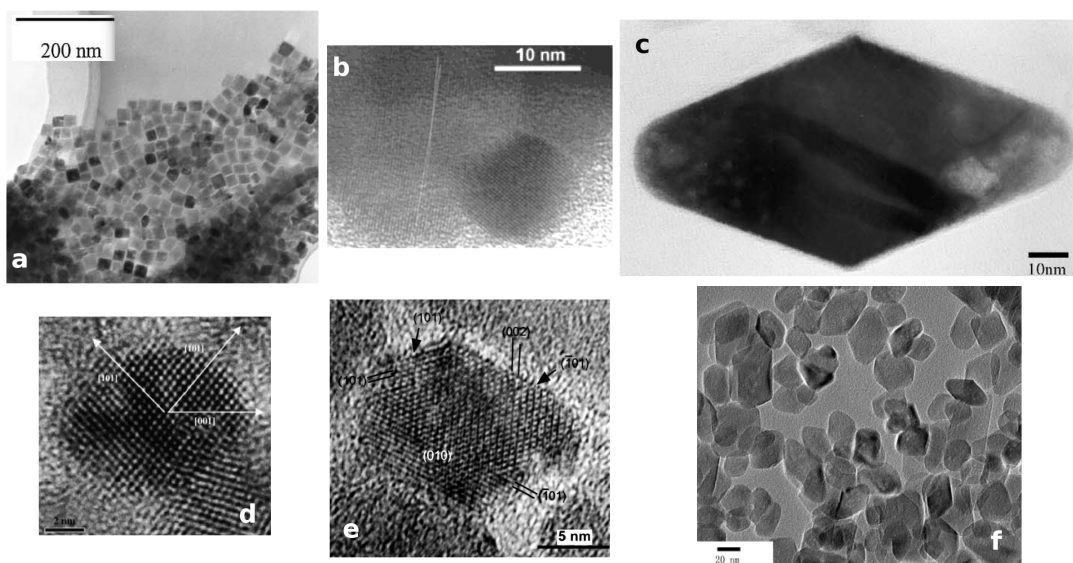


Figure 2.1: a) TEM image of a cubic anatase TiO_2 nanoparticles formed in a solution of 0.10 mol dm^{-3} Ti(IV)-TEOA (1:2) compound at initial pH 10.5 and with 0.02 mol dm^{-3} sodium oleate [59]. b) TEM image of a spherical anatase nanoparticle obtained by heating at 375°C for 3 hours [60]. c) HRTEM image of a bipyramidal anatase nanoparticle obtained heating at 240°C for 64 hours [61]. d) HRTEM image of a spherical anatase nanoparticle synthesized with NaCl [62]. d) TEM image of a truncated tetragonal nanocrystal hydrothermally treated at 120 and 190°C , then diluted in presence of tetramethylammonium hydroxide [63]. f) TEM image of nanoparticles obtained by hydrothermal treatment at 180°C for 12 hours in double-distilled water [64].

precursors takes place and a second step in which the growth of the atomic wires is allowed by the presence of surfactants, see Fig. 2.2 (B-D).

- *Hydrothermal method* is usually performed in steel pressure vessels (autoclaves) with the optional use of Teflon liners under controlled temperature and pressure with the reaction in aqueous solutions. The temperature can be elevated above the boiling point of water, reaching the pressure of vapor saturation. The temperature and the amount of solution added to the autoclave largely determine the internal pressure produced. This method is widely used for the production of small particles in the ceramics industry. The *Solvothermal method* is almost identical to the hydrothermal one apart for the substitution of the water with another solvent.

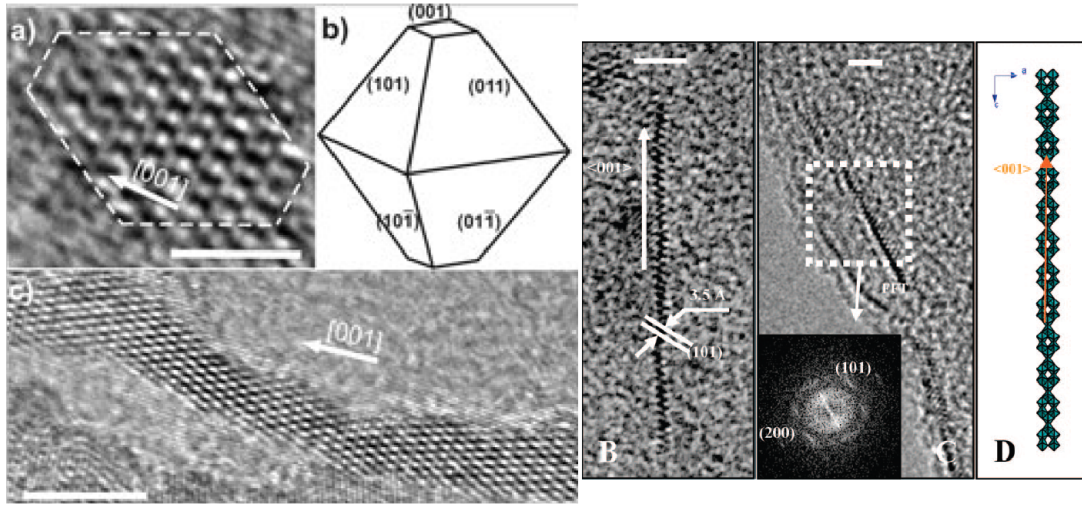


Figure 2.2: On the left, a) HRTEM image of a trizma-functionalized truncated bipyramidal domain; b) proposed morphology of the anatase nanocrystal; c) a chain of nanoparticles forming an anatase nanowire in the $[001]$ direction [57], scale bar 2 nm. On the right, B) HRTEM micrograph of a single atomic wire with a diameter of around 4.3 Å and lattice fringes spaced at about 3.5 Å, corresponding to the spacing between the (101) planes of anatase TiO_2 ; C) HRTEM image of atomic wires with the corresponding FFT pattern in the inset; D) Model structure of an anatase atomic wire growing along (001) direction [58].

However, the temperature can be elevated much higher than that in hydrothermal method, since a variety of organic solvents with high boiling points can be chosen. The solvothermal method usually has better control of the size and shape distributions and crystallinity of the TiO_2 nanoparticles than the hydrothermal ones, as shown in Fig. 2.1 (d-f).

Another well developed method deals with the direct oxidation of titanium metal using oxidants (peroxide) or under anodization (*Direct oxidation method*). If materials in a vaporate state are condensed to form a solid-phase material within a vacuum chamber through chemical reactions, the process is called chemical vapor deposition (*CVD method*). In absence of chemical reactions the process is a physical vapor deposition (*PVD method*). In CVD processes, thermal energy heats the gases in the coating chamber and drives the deposition reaction. Thick crystalline TiO_2 films with grain sizes below 30 nm as well as TiO_2 nanoparticles with sizes below 10

nm have been obtained with these techniques [8]. Other, more recent, techniques are the electrodeposition, the sonochemical method, and the microwave method.

2.2 Structural determinations

2.2.1 X-ray electron diffraction on powders

X-ray diffraction powder patterns come from the interference pattern of elastically dispersed X-ray beams by atomic cores and, in the case of materials with moderate to long-range order, contain information that arises from both the atomic structure and the particle characteristics (for example, size, strain). Alternatively, the radial distribution of the atomic pair distances in the material can be determined by the appropriate Fourier transform of the diffraction pattern independent of any requirement of long-range coherence. This is an advantage in the study of nanoparticles or nanostructures in which there is reduced long-range order [11].

The lattice spacing (d) between crystal planes can be extracted using the Bragg law: $2d\sin\theta = n\lambda$, where λ is the X-ray radiation wavelength, n is an integer number, θ is the reflection angle set equal to the incidence angle, d depends on the particular set of planes considered, as classified according to the Miller scheme [49]. The crystal lattice parameters can be measured by the above relation. In the $\omega - 2\theta$ (or $\theta - 2\theta$) scan diffraction measurements, incidence and reflection angle ω and θ are changed simultaneously so that the condition $\omega = 2\theta/2$ is always satisfied (symmetrical configuration: here 2θ is the angle between the incident source ray and emerging ray, while ω is the angle between the sample surface and the incident ray). In Fig.2.3 the apparatus is schematically represented. When the reflection angle catches up the value for which the relation of constructive interference is satisfied, a strong signal is observed at the detector corresponding to a peak in the intensity vs. 2θ spectrum. When the measurement is carried out on a randomly oriented powder, the peak intensity depends on the intrinsic details of the crystal structure. Ideally, every possible crystalline orientation is represented equally in a powdered sample. The resulting orientational averaging causes the three dimensional reciprocal space that is studied in single crystal diffraction to be projected onto a single dimension. The three dimensional space can be described in spherical coordinates q , φ , χ . In

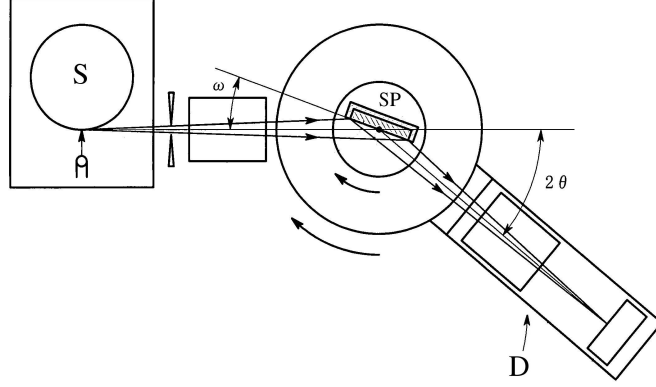


Figure 2.3: Schematic representation of an automatic diffractometer in the Bragg-Brentan geometry. S is the X-ray source, D the detector of diffracted ray, SP the sample holder.

powder diffraction, intensity is homogeneous over φ and χ and only q remains as an important measurable quantity. In practice, it is sometimes necessary to rotate the sample to eliminate the effects of texturing and achieve true randomness. When the scattered radiation is collected on a flat plate detector, the rotational averaging leads to smooth diffraction rings around the beam axis rather than the discrete Laue spots as observed for single crystal diffraction. The angle between the beam axis and the ring is the scattering angle 2θ . In accordance with Bragg's law, each ring corresponds to a particular reciprocal lattice vector G in the sample crystal ($G = 2\pi n/d$). Powder diffraction data are usually presented as a diffractogram in which the diffracted intensity I is shown as function either of the scattering angle 2θ or as a function of the scattering vector q .

Li *et al.* [65] observed a contraction of the volume of anatase nanoparticle as function of decreasing size, by applying a standard least square method to calculate the cell parameters. On the other hand, Swamy *et al.* [13] found that the volume and the lattice parameter a of TiO_2 nanosamples shorter than 10 nm underwent an increase with the size decrease, whereas the parameter c was found to contract. X-ray diffraction has been widely used to characterize the crystal phase of TiO_2 nanosamples, from which it has been found that the anatase phase is thermodynamically favoured with respect to the rutile phase under 11 nm [8, 66]. From X-ray

diffraction it also possible to estimate the nanosample grain size according to the Scherrer equation

$$D = \frac{K\lambda}{\beta \cos(\theta)} \quad (2.1)$$

where K is a dimensionless constant and β is the full width at half-maximum of the diffraction peak. Nanocrystalline size is determined by measuring the broadening of a particular peak in the diffraction pattern associated with a particular planar reflection from within the crystal unit cell. Nanoparticles are synthesized with diameters as small as 1 nm [67] and NWs with a diameter of 4.3 Å [58].

2.2.2 Extended X-ray absorption fine structure

This spectroscopy technique provide structural information about a sample by way of the analysis of its X-ray absorption spectrum. It allows determining the chemical environment of a single element in terms of the number and type of its neighbours, inter-atomic distances and structural disorders. This determination is confined to a distance given by the mean free path of the photoelectron in the condensed matter, in the Angstrom length scale. These characteristics make the extended X-ray absorption fine structure spectroscopy (EXAFS) a powerful structural local probe, which does not require a long-range order. Furthermore, EXAFS does not require any particular experimental conditions, such as vacuum (at least in principle). There are several types of sample-holders that allow collecting experimental data under varying temperature and pressure, or while the sample is undergoing a chemical reaction (*in-situ* analysis) [69].

The X-ray absorption coefficient for an atom, indicated as μx , is directly proportional to the probability of absorption of one photon and is a monotone decreasing function of energy. It shows several discontinuities known as absorption edges, that occur when the energy of the incident photons equals the binding energy of one electron of the atom (classified as K, L, M... according to the principal quantum number $n= 1, 2, 3...$). The edge energy is characteristic of each atom. When the incident photon excite an electron with energy above the edge, it becomes an extracted photoelectron that will be scattered by the atoms around the absorber. The

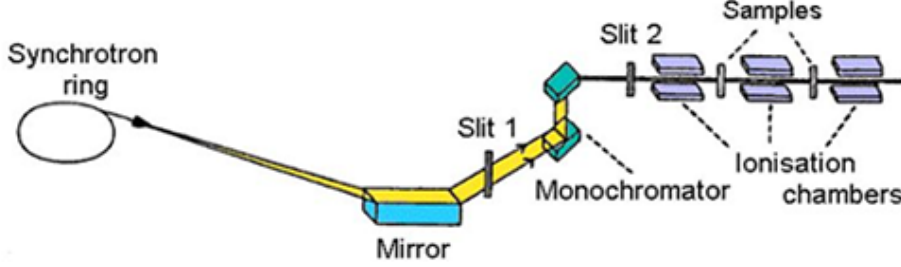


Figure 2.4: Schematic view of a X-ray beamline with synchrotron.

final state of the photoelectron can be described by the sum of the original and scattered waves. This leads to an interference phenomenon that modifies the interaction probability between core electrons and incident photons. The absorption coefficient will increase with constructive interference. Most importantly, the interference phenomenon, for a given energy of the photoelectron, depends on the distance between emitting and scattering atoms, and their atomic numbers. The EXAFS signal $\chi(k)$ is defined as a function of the wave vector \mathbf{k} . It is mathematically defined as:

$$\chi(k) = \frac{\mu x - \mu_I x}{\mu_I x} = \frac{\mu x}{\mu_I x} - 1 \quad (2.2)$$

where μx is the experimental absorption coefficient and $\mu_I x$ is the intrinsic atomic absorption coefficient. Such a definition means that $\chi(k)$ contains only the oscillatory part of the absorption coefficient.

In a typical experimental set-up (Fig. 2.4) ionization cells monitor the intensity of incident (I_0) and transmitted (I_1) monochromatic photon beam through the sample, while scanning energy using a crystal monochromator (200 eV below to 1000 eV above the edge energy). The Lambert-Beer law relates intensities I_0 and I to the absorption coefficient: $\ln(I_0/I) = \mu x$. Because of the angular rotation of the crystals inside the monochromator, the beam can shift up or down. Light must pass through the sample always at the same position, so either the sample follows the beam by placing it on a micrometric table, or it is necessary to change the monochromator mechanism to obtain a fixed beam.

For analyzing the EXAFS spectrum, we must separate the useful information (oscillation part) from the total raw spectrum. Then convert the oscillation part

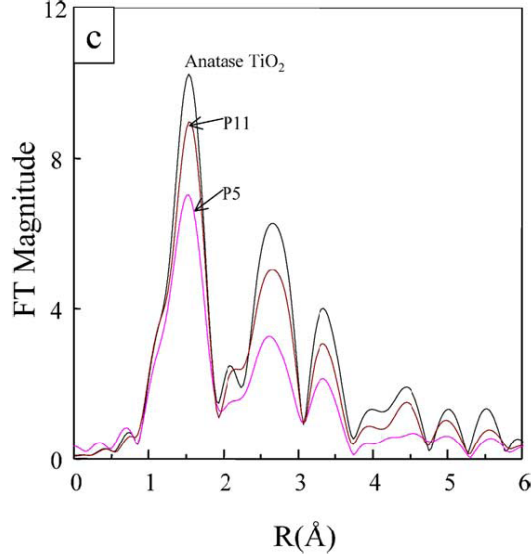


Figure 2.5: EXAFS spectra of bulk anatase TiO_2 (black), a nanoparticle with a diameter of 5 nm (P5, red curve), and a nanoparticle with a diameter of 11 nm (P11, violet curve) [18].

into k space by using the equation $k = [0.263(EE_0)]^{1/2}$, where E_0 is the absorption edge. At last, the oscillation signal is filtered by Fast Fourier Transform and then fitted by the theoretical equation

$$\chi(k) = \sum_j \frac{N_j}{kr_j^2} |f_j(k)| e^{-k^2\sigma_j^2} e^{-2r_j/\lambda} \sin \left[2kr_j + \varphi(k) + \frac{0.2625r_j\Delta E_0}{k} \right] \quad (2.3)$$

where $\chi(k)$ is the filtered oscillation signal multiplied by a factor k^3 , j is the number of the coordination shells, $f_j(k)$ is the amplitude value that can be obtained from handbook, $\varphi(k)$ is the phase displacement of scattering, ΔE_0 is the difference between the theoretical value and the experimental value of the E_0 , N is coordination number, r is coordination distance, σ is Debye-Waller factor, and λ is electron mean-free path [70]. Fig. 2.5 shows an example of FT EXAFS spectra of TiO_2 nanoparticles compared to the bulk anatase phase. The aim is to obtain the structural parameters N , r , σ , and λ . Generally, the cubic spline interpolation method is used for the background removal and the least-squares method is used for the curve fitting. EXAFS is usually combined with X-ray absorption near edge spectroscopy

(XANES), the only difference being in the energy range of the final electronic state, which is lower than 50 eV in the latter case. XANES spectra also give purely electronic informations (e.g. chemical bonding). With these techniques experimentalists found the distortion of the octahedral coordination of titanium atoms in TiO_2 nanoparticles, resulting in variations of Ti-O atomic bond lengths, distances between atoms, and coordination numbers [14, 15, 16, 17, 18].

2.2.3 Transmission electron microscopy

If electrons are emitted in vacuum from a heated filament and accelerated through a potential difference of 50kV, their wavelength is about $1/20 \text{ \AA}$ so that they can penetrate distances of several microns into a solid. If the solid is crystalline, the electrons are diffracted by atomic planes inside the material, as in the case of x-rays. It is therefore possible to form a transmission electron diffraction pattern from electrons that have passed through a thin specimen. By focusing the transmitted electrons with electric or magnetic fields, the specimen can be imaged with a high spatial resolution [68].

In a transmission electron microscope (TEM), electrons penetrate a thin specimen and are then imaged by appropriate lenses. These are stacked in a vertical column, as shown in Fig. 2.6. The source of electrons is a V-shaped filament made from tungsten wire, which emits electrons when heated in vacuum tube and transistors control the lens currents and the voltage. The lenses of a TEM allow for beam convergence. Typically a TEM consists of condensor lenses that are responsible for primary beam formation, of objective lenses that focus the beam down onto the sample itself, and projector lenses that are used to expand the beam onto the phosphor screen or other imaging device. The magnification of the TEM is due to the ratio of the distances between the specimen and the objective lens' image plane. The vacuum system for evacuating a TEM to an operating pressure level consists of several stages. It is necessary to allow for the voltage difference between the cathode and the ground without generating an arc and to reduce the collision frequency of electrons with gas atoms to negligible levels. The most common mode of operation for a TEM is the bright field imaging mode. In this mode the contrast formation, when considered classically, is formed directly by occlusion and absorption of elec-

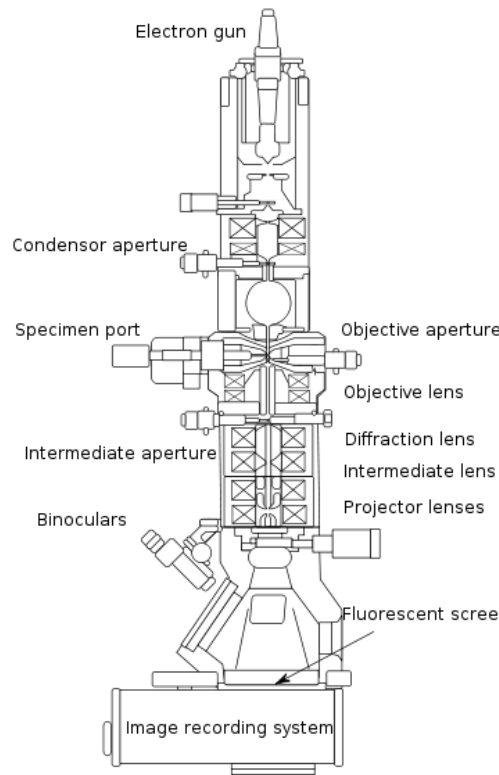


Figure 2.6: Schematic representation of the basic components of a TEM.

trons in the sample. Thicker regions of the sample, or regions with a higher atomic number will appear dark, while regions with no sample in the beam path will appear bright. The image is in effect assumed to be a simple two dimensional projection of the sample down the optic axis, and to a first approximation may be modelled via Beer's law, more complex analyses require the modelling of the sample to include phase information.

Another imaging (usually bright field) mode of the TEM is the high-resolution transmission electron microscopy (HRTEM). It allows the imaging of the crystallographic structure of a sample at an atomic scale. Because of its high resolution, it is an invaluable tool to study nanoscale properties of crystalline material such as semiconductors and metals. HRTEM does not use amplitudes, i.e. absorption by the sample, for image formation. Instead, contrast arises from the interference in the image plane of the electron wave with itself. Due to our inability to record the

phase of these waves, the amplitude resulting from this interference are generally measured, however the phase of the electron wave still carries the information about the sample and generates contrast in the image. Both TEM and HRTEM techniques allow to have readily informations on the structure of nanosamples like size, crystal orientation, defects, and shape as previously shown in Fig. 2.1 and Fig. 2.2.

2.2.4 Infrared spectroscopy

Infrared (IR) spectroscopy exploits the fact that molecules have specific frequencies at which they rotate or vibrate corresponding to discrete energy levels (vibrational modes). The infrared region of the electromagnetic spectrum extends from 14.000 to 10 cm^{-1} , but the region of major interest for chemical analysis is the mid-infrared (4.000 to 400 cm^{-1}), which corresponds to changes in vibrational energies within molecules. In order for a vibrational mode in a molecule to be IR active, it must be associated with changes in the permanent dipole. It can be used to identify compounds or to investigate sample composition. Nevertheless, the resonant frequencies can be in a first approach related to the strength of the bond, and the mass of the atoms at either end of it.

The infrared spectrum of a sample is collected by passing a beam of infrared light through the sample, see Fig. 2.7. Examination of the transmitted light reveals the quantity of energy absorbed at each wavelength. This can be done with a monochromatic beam, which changes in wavelength over time, or by using a Fourier transform instrument to measure all wavelengths at once. From this, a transmittance or absorbance spectrum can be produced, showing at which IR wavelengths the sample absorbs. Analysis of these absorption characteristics reveals details about the molecular structure of the sample. Solid samples can be prepared in four major ways. In the case of TiO_2 nanoparticles, the sample is ground to give a very fine powder. A small amount is then mixed to give a paste and several drops of this paste are then applied between two sodium chloride plates (these do not absorb infrared in the region of interest). The plates are then placed in the instrument sample holder ready for scanning.

A beam of infrared light is produced and split into two separate beams. One is passed through the sample, the other passed through a reference which is often the

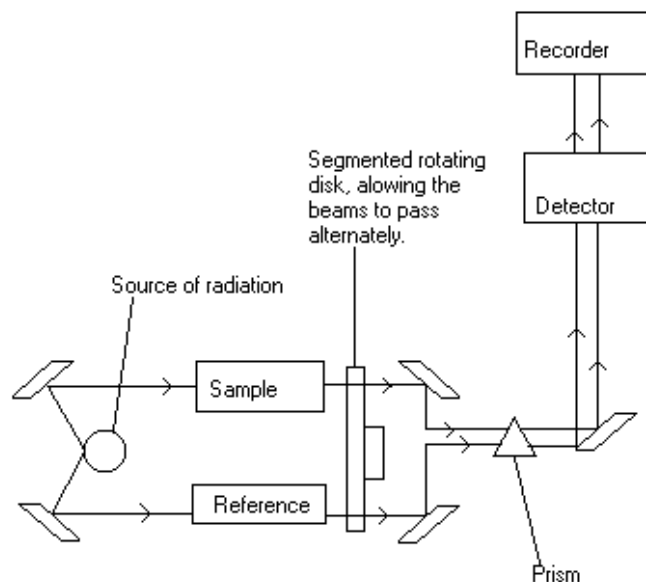


Figure 2.7: Schematic representation of an IR spectrometer.

substance the sample is dissolved in. The beams are both reflected back towards a detector, however first they pass through a splitter which quickly alternates which of the two beams enters the detector. The two signals are then compared and a printout is obtained.

Fourier transform infrared (FTIR) spectroscopy is most frequently used for TiO_2 nanoparticles. Instead of recording the amount of energy absorbed when the frequency of the infrared light is varied (monochromator), the IR light is guided through an interferometer. After passing through the sample, the measured signal is the interferogram. Performing a mathematical Fourier transform on this signal results in a spectrum identical to that from conventional (dispersive) infrared spectroscopy. FTIR spectrometers are cheaper than conventional spectrometers because building of interferometers is easier than the fabrication of a monochromator. In addition, measurement of a single spectrum is faster for the FTIR technique because the information at all frequencies is collected simultaneously. This allows multiple samples to be collected and averaged together resulting in an improvement in sensitivity. In

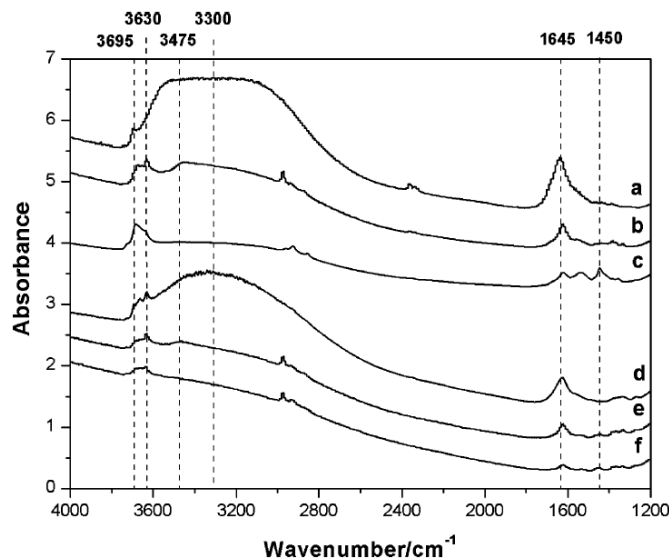


Figure 2.8: . FTIR spectra of anatase nanoparticles with a diameter of 11 nm (a, b, and c) and 16 nm (d, e, and f): hydrated, (a and d), evacuated at room temperature (b and e), and evacuated at 373 K (c and f) [28].

general, to obtain a more detailed interpretation of an IR spectrum it is necessary to refer to correlation charts and tables of infrared data. Since there are many different vibrations even within relatively simple molecules, the infrared spectrum of a compound usually contains a large number of peaks, many of which will be impossible to confidently assign to vibration of a particular group. In Fig. 2.8, an example of FTIR spectra of TiO_2 nanoparticles is shown. TiO_2 nanoparticles are found to adsorb water at surface in a large variety of configurations and strength of bonds. A multilayered hydration sphere is usually detected and can play an important role in stabilizing the system and participate in the photocatalytic activity of TiO_2 [28, 71, 72, 73, 74].

2.3 Electronic determinations

We report the basic aspects of two techniques which are mainly used in the electronic characterization of TiO_2 nanostructures, namely ultraviolet-visible absorption mea-

measurements for the determination of the optical band gap of TiO_2 at the nanoscale, and electron paramagnetic resonance for the determination of the charge trap sites of photoexcited, charged, or doped nanosamples.

2.3.1 Ultraviolet-visible absorption measurements

The spectrophotometer used in ultraviolet-visible (UV-vis) spectroscopy measures the intensity of light passing through a sample (I), and compares it to the intensity of light before it passes through the sample (I_0). The ratio I/I_0 is called the transmittance, and is usually expressed as a percentage ($\%T$). Important quantities are the absorbance A , defined as $A = \log(\%T/100\%)$ and the absorption coefficient $\alpha(\lambda)$, which is related to the transmittance through the relation

$$T = \frac{(1 - R)^2}{1 - R^2} e^{(-\alpha(\lambda)d)}, \quad (2.4)$$

where R is the reflectance and d is the optical path length. The absorption coefficient α depends on the energy:

$$\alpha(\lambda) = B(\hbar\nu - E_g)^n(\hbar\nu)^{-1} \quad (2.5)$$

where B is a constant and E_g is the band gap energy. The basic parts of a spectrophotometer are a light source, a holder for the sample, a diffraction grating or monochromator to separate the different wavelengths of light, and a detector. The radiation source is often a Tungsten filament (300-2500 nm), a deuterium arc lamp which is continuous over the ultraviolet region (190-400 nm), and more recently light emitting diodes and Xenon Arc Lamps for the visible wavelengths. The detector is typically a photodiode or a CCD. Photodiodes are used with monochromators, which filter the light so that only light of a single wavelength reaches the detector. Diffraction gratings are used with CCDs, which collects light of different wavelengths on different pixels. Samples are typically placed in a transparent cell made of quartz glass.

The optical band gap of TiO_2 at the nanoscale has become an intriguing issue, since its determination gave contrasting results. The onset radius of nanoparticles at which the band gap blue shift expected for size confined systems, as well as the nature

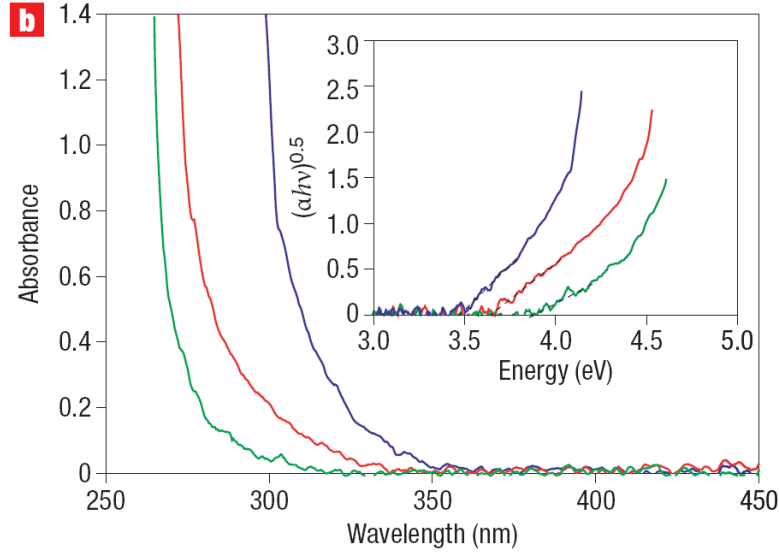


Figure 2.9: Absorbance of three TiO_2 nanoparticles of increasing size (from the blue to the green curve). The inset shows the Tauc plots for these thermolysed nanosamples [67].

of the transition, has been a matter of debate [22, 23]. The exciton radius is reported in the range 0.35 – 1.9 nm [22, 75] while the effective mass for hole and electron is not unambiguously determined [22], such that even the effective mass approximation has been considered arguable for small TiO_2 nanoparticles [23]. It follows that some nanocrystals are blueshifted in the range 1 – 10 nm [76, 77, 78, 67], while others show the bulk band gap down to 1.5 nm [22, 23]. In Fig. 2.9 we report the absorbance and the absorption coefficient as measured by Satoh *et al.* [67] in a very recent work. They reported a blue shift of the order of 0.7 eV for nanoparticles with a diameter of 1 nm synthesized by finely controlled metal assembly on dendrimer templates, which ensured a high degree of crystallinity to the thermolysed nanosamples.

The same controversy stands for 1D NWs, whose diameter acts as the confinement direction. However, a better crystallinity should preserve a more ideal behaviour against the effects of the preparation methods and surface environment, hence blue shifts of 0.1 – 0.5 eV are reported for TiO_2 1D nanostructures in the diameter range of 2 – 9 nm [33, 79, 80, 81].

2.3.2 Electron paramagnetic spectroscopy

Electron paramagnetic resonance (EPR) spectroscopy is a technique for studying chemical species that have one or more unpaired electrons, such as inorganic complexes possessing a transition metal ion. The basic physical concept is based on the excitation of electron spin. In the presence of an external magnetic field with strength B_0 , the electron magnetic moment aligns itself either parallel ($m_s = -1/2$) or antiparallel ($m_s = +1/2$) to the field, each alignment having a specific energy. The parallel alignment corresponds to the lower energy state, and the separation between it and the upper state is $\Delta E = g_e \mu_B B_0$, where g_e is the g-factor and μ_B is the Bohr magneton. This equation implies that the splitting of the energy levels is directly proportional to the strength of the magnetic field.

An unpaired electron can pass between the two energy levels by either absorbing or emitting electromagnetic radiation of energy $\Delta E = h\nu$, from which $h\nu = g_e \mu_B B_0$. Knowledge of the g-factor can give information about the electronic structure of a paramagnetic center. An unpaired electron responds not only to the magnetic field but also to any local magnetic fields of atoms or molecules. The effective field B_{eff} experienced by an electron is thus written as $B_{\text{eff}} = B_0(1 - \sigma)$, where σ includes the effects of local fields. Experimentally, this equation permits a large combination of frequency and magnetic field values, but the great majority of EPR measurements are made with microwaves in the 9000–10000 MHz (9–10 GHz) region, with fields corresponding to about 3500 G (0.35 T). In practice EPR spectra are generated by varying the magnetic field while holding constant the photon frequency incident on a sample. A collection of paramagnetic centers, such as free radicals, is exposed to microwaves at a fixed frequency. By increasing an external magnetic field, the gap between energy states is widened until it matches the energy of the microwaves. Due to the Maxwell-Boltzmann distribution, there is a net energy absorption from the lower state, which is monitored and converted into a spectrum.

Berger *et al.* [30] used EPR measurements to demonstrate that electron transfers spontaneously from atomic hydrogen to dehydroxylated TiO₂ nanoparticles at 77 K and produces a charge separation state which is characterized by surface adsorbed protons and trapped electrons forming paramagnetic Ti³⁺ (d¹) states (see Fig. 2.10). For the EPR measurements a Suprasil quartz glass tube was connected to a high

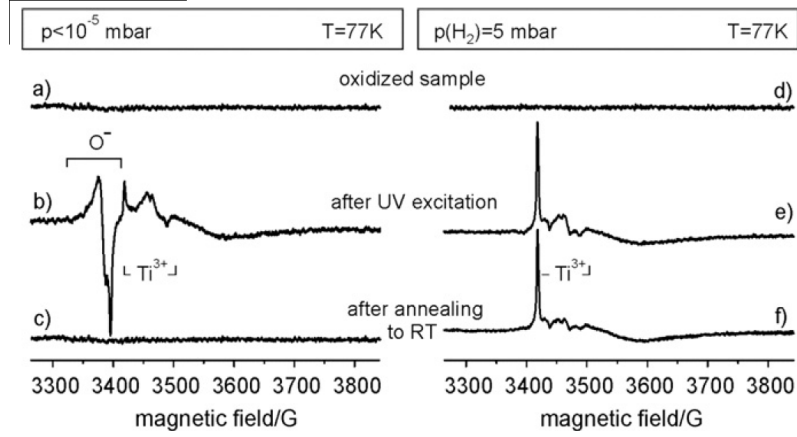


Figure 2.10: EPR spectra of anatase nanoparticles before (a/d) and after (b/e) UV exposure carried out in different gas atmospheres. While at $p < 10^{-5}$ mbar (a-c) warming to 298 K induces complete annihilation of the charge separation state (c), at $p(\text{H}_2) = 5$ mbar trapped and localized electron centers remain persistently trapped even after warming to $T = 298$ K (df). The spectra related to (e) and (f) are compressed by a factor of 0.2 in comparison to those of (a-c) [30].

vacuum pumping system which allows thermal sample activation at $p = 10^{-6}$ mbar. Hydrogen atoms were produced in situ in a 2.45 GHz microwave discharge under static conditions. Typical hydrogen pressure was 0.3 mbar. The sample (typically 15 mg) was kept at 77 K during the plasma treatment to avoid local heating. EPR spectra were then recorded at 77 K and 1 mW microwave power.

In another work, Berger *et al.* [82] studied UV light-induced electron-hole pair excitations in anatase TiO_2 nanoparticles by EPR and IR spectroscopy. The localized states such as holes trapped at oxygen anions (O^-) and electrons trapped at coordinatively unsaturated cations (Ti^{3+} formation) were accessible to EPR spectroscopy. Delocalized and EPR silent electrons in the conduction band may be traced by their IR absorption, which results from their electronic excitation within the conduction band in the infrared region. They found that, during continuous UV irradiation, photogenerated electrons were either trapped at localized sites, giving paramagnetic Ti^{3+} centers, or remained in the conduction band as EPR silent species which may be observed by their IR absorption and that the EPR-detected holes produced by photoexcitation were O^- species, produced from lattice O^{2-} ions. It was also found that,

under high-vacuum conditions, the majority of photo- excited electrons remained in the conduction band. At 298 K, all stable hole and electron states were lost [8]. An unsolved problem in the photocatalytic activity of TiO_2 , i.e. the nature of the h^+ trap responsible for the oxidation of reactants [83], came out also by using EPR measurements. There is consensus on the fact that recombination of photocharges is delayed by trapping in localized states, from which photocharges are transferred to dissolved reactants [83, 84]. However the hole trap site is not yet unambiguously determined, since it has been assigned to terminal hydroxyl radicals [84, 85], lattice oxygens [82], subsurface oxygens [86], surface oxygen radicals [87, 88].

2.4 Conclusion

In this chapter we have described experimental techniques commonly used to obtain information on the properties of TiO_2 nanostructures. Different methods are used to measure quantitative structural and electronic properties or to draw a qualitative picture of the local structural reconstructions and nature of the bonds occurring at the surface of TiO_2 containing complexes. We have focused our attention in particular on XRD, EXAFS, TEM, and IR spectroscopy for the study of the structure of TiO_2 nanomaterials and adsorbed molecules, at an atomic scale. Electronic properties have been presented through the description of UV-vis absorption and EPR measurements giving interesting results, although there are many works which use other techniques (ultraviolet photoelectron spectroscopy, photoluminescence, etc.) in the growing experimental literature of nanostructured TiO_2 . In the followings, we discuss theoretical models which complement such results and give new insight into the physics of low dimensional TiO_2 .

Chapter 3

TiO₂ 0D nanocrystals

The aim of this chapter is to give an insight into the structural and electronic properties of TiO₂ NCs with differently covered surfaces, using ab-initio Density Functional Theory (DFT) calculations. TiO₂ NCs are mostly synthesized with sol-gel methods showing a high degree of crystallinity [21]. Crystal phase and morphology are strongly affected by synthesis conditions, however both theoretical and experimental results proved the anatase polymorph to be favoured for the smallest samples (< 14 nm) and acidic pH to stabilize truncated tetragonal bipyramidal NCs with [101], [011], [010] and [001] facets [89, 66, 63, 61, 57]. Following the suggestions proposed by Polleux *et al.* [57], we consider truncated bipyramidal systems with [101] and [011] as lateral surfaces and [001] as the truncation surface, to model the experimentally observed nanostructures. An analogous morphology has been recently proposed by Wu *et al.* [90] as preferable for dye-sensitized solar cells.

The request of smallness of the systems due to computational effort, of stoichiometry to avoid problems of charging, of the highest coordination for each atom to support their formal oxidation state (i.e. O²⁻ and Ti⁴⁺), were not an easy task to be simultaneously fulfilled, as previously reported by Persson *et al.* [91]. Moreover the pure, or bare, anatase NC presented in this chapter are somehow connected with the NC studied in a recent work by Barnard *et al.* [92]. At the end we retained bipyramids with truncation along the [001] direction so eliminating most of the undercoordinated atoms, whose number raises coming closer to the NC tip. This choice meets the experimental evidence that bipyramids are always truncated

or smoothed at tips due to growing dynamics, surface tension and functionalizing adsorbates [61, 57]. Indeed our choice is also suitable for aligning and assembling NCs in longer chains, since tipped bipyramids would produce too narrow necks.

There are many open questions about nanostructured TiO_2 , some of which are object of this chapter and are summarized in the following.

Structural properties. The reduction of sample size produces an unavoidable variation of the structural arrangement. Lattice parameters have been observed to expand in some cases [13] or to contract in others [65], while rutile and other metal oxides show a linear expansion on decreasing the particle size. A dependence on the preparation method is also observed: sol-gel/hydrolysis methods lead to lattice strain, expansion and Ti deficiency, whereas nonhydrolytic sol-gel routes lead to pure and stoichiometric samples with nonlinear volume contraction [13].

In the bulk anatase, a titanium (Ti) atom is in the center of an octahedron whose vertices are occupied by six oxygens (O). This coordination is preserved in internal NC cells but the surface truncation produces undercoordination, dangling bonds and surface tension whose effect is a local disorder [14]. Some experimental works have observed the variation of bond lengths and coordination numbers upon decreasing the NC size, in the smallest samples (< 5 nm) [14, 15, 16, 17, 18]. This suggests an influence of the surface on the overall structure. Reactive compounds in solution can change the NC morphology as proved by the restoring of the octahedral coordination for the surface Ti atoms after adsorption of radicals [15, 19].

Electronic properties. The anatase TiO_2 crystal is an indirect semiconductor with an energy gap of 3.2 eV [9]. On a theoretical general ground, a decrease of the dimensions down to the nanometer scale makes the electron mean free path comparable with system size; thus, one would expect a quantum-size (Q-size) effect to be measurable through the band gap blue shift. This shift is not always detectable in nanostructured TiO_2 : (i) some authors [21, 22, 23] observed the bulk gap for sample diameters down to 1.5 nm; (ii) others [10, 24, 25] measured a blue shift already in the range 5 – 10 nm (just recently, a clear detection of the blue shift, for both anatase and rutile polymorphs, has been observed [67]); (iii) a red shift is also observed and mainly ascribed to the presence of surface oxygen vacancies [93, 94] (behaving as shallow traps for photogenerated charge carriers), to adsorbates or dopants producing electronic states in the forbidden region [10]. The nature of the

first allowed transition is still under debate as well, since a direct radiative decay blue shift of the band gap is advised [11, 22, 26].

Surface functionalization. TiO_2 is the best candidate for photovoltaic solar cell conversion of light and for water splitting, with consequent hydrogen production on a large scale [9, 95]. These ambitious goals need a deep understanding of the interaction of TiO_2 with water and its constituents. The presence of a large hydration sphere surrounding TiO_2 nanoparticles is usually detected [28], for example by infrared spectrum analysis [71], and may play a fundamental role in photocatalysis. This hydration sphere is built up of different and non equivalent bonds between water and the TiO_2 surface [72] and of weak hydrogen bonds among water molecules [71] (thus forming a multilayered wet sphere [28]). The first water coverage can be made of both a dissociative and a molecular chemisorption [73] on the NC surface, but the dissociative adsorption seems to be favoured [74], being capable to fill possible oxygen vacancies in the synthesis process. Early works directly focused on the TiO_2 -H surface interaction and doping of NCs have been reported very recently [29, 30]. Keeping this in mind we decided to cover our bare systems with simple adsorbates (H_2 and H_2O), modelling simple and stable surface configurations in presence of hydrogens and hydration.

It is evident that the very numerous experimental data on TiO_2 NCs produced a large variety of, often conflicting, results. The lack of a satisfactory and organic comprehension of many of the measured properties can certainly be ascribed to the TiO_2 own nature - very high reactivity toward the external environment, ability to sustain complex surface chemistry, O vacancies, etc. The aim of this chapter is to shed light, at least partially, on some of these aspects. First principles calculations based on DFT will be applied to NCs with different surface coverages. Structural and electronic properties will be analyzed and compared to experiments.

In Sec. 3.1 we summarize the method and computational details and we define the NCs studied in this chapter. In Sec. 3.2 we discuss the results on the NC reconstruction in presence of different surface coverages. In Sec. 3.3 we study the NC electronic properties. The nature of the electronic levels is elucidated from density of states (DOS) calculations and plots of the highest occupied and lowest unoccupied molecular orbitals (HOMO and LUMO respectively). In Sec. 3.4 we discuss the formation energy of the NCs. We will show that the hydrated NC is the

most stable, whereas the hydrogen covered NC (representative of an extreme acidic condition) is the most unstable one.

3.1 Methodology

All first-principles calculations are carried out within the DFT framework, employing the QUANTUM-ESPRESSO package [51] based on plane waves and pseudopotentials. We used the generalized gradient approximation (GGA) parametrized with the Perdew-Wang (PW91) exchange-correlation functional [96] and Vanderbilt ultrasoft pseudopotentials [52]. The reciprocal space is sampled using a plane-wave basis set up to a kinetic energy cutoff of 30 Ry for the wave functions. The NC geometries are optimized with the direct energy minimization technique of Broyden-Fletcher-Goldfarb-Shanno [97], which is a quasi-Newton method based on the construction of an approximated Hessian matrix at each system relaxation step. The optimization is stopped when each Cartesian component of the force acting on each atom is less than 0.026 eV/Å and the total energy difference between consecutive steps is less than 10^{-4} eV. All properties presented in the next sections are referred to the optimized systems. A vacuum gap of at least 6 Å separates each NC from its periodic replica in neighbour supercells to avoid spurious interactions. The convergence of the geometry, the electronic properties, the formation and total energy with respect to the above parameters has been carefully checked.

The structural optimization of the tetragonal three-dimensional anatase crystal gave lattice constants $a=3.809$ Å and $c=9.604$ Å, whereas the internal dimensionless parameter is $u=0.208$. All three numbers compare well to the experimental values (at 15 K) 3.782 Å, 9.502 Å and 0.208 respectively [98]. The starting geometry of the bare TiO₂ NC is defined with atoms at the ideal crystal positions. The atomic positions were then randomized by 1% breaking symmetries and thus ensuring an unconstrained and more physical relaxation.

The bare stoichiometric NC (sc29) presented in this chapter is made of 87 atoms with chemical formula (TiO₂)₂₉ (see Fig. 3.1). Its morphology derives from a perfect bipyramid with [101] and [011] lateral surfaces, then truncated along [001], [100] and [010] directions. To ensure the stoichiometry four oxygen atoms, in the crystal con-

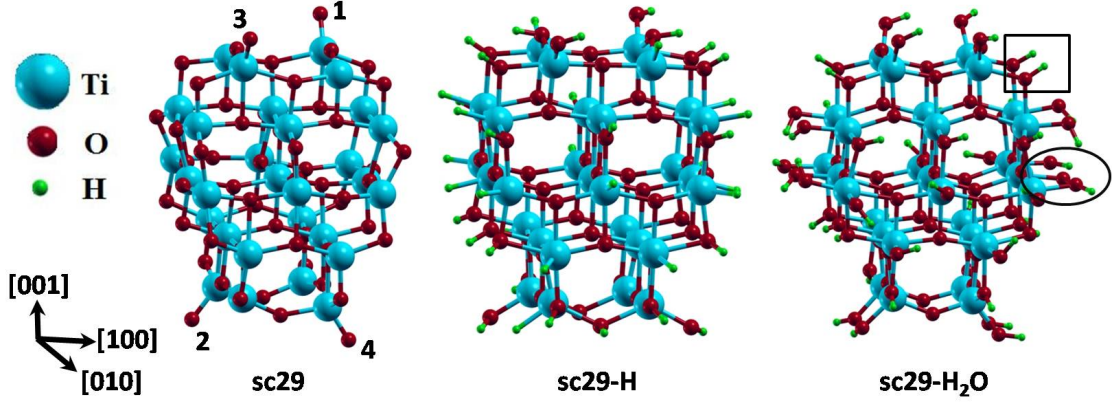


Figure 3.1: Optimized structures of the stoichiometric NCs [99]. The one-coordinated oxygens are labeled in the left NC in the same order as they are removed to form sub-stoichiometric bare NCs nc29-*MO* (see text). In the hydrated NC (on the right) the box shows some chemisorbed OH groups labelled as OH^{in} in the text, whereas the circle some examples of chemisorbed OH groups labelled as OH^{out} in the text.

figuration, were added on the [001] surfaces, labelled as one-coordinated oxygens (see Fig. 3.1). Several efforts to relax the system with these atoms placed on the square base of the structure did not converge, probably revealing the relevance of the TiO_2 anisotropy along the [001] direction [9]. The resultant morphology is not easy to explain since it can be viewed as an ellipsoid or a quasi-sphere anyhow nanofaceted, resembling the model obtained by S. Dzwigaj *et al.*[100] on a study of hydrated anatase surfaces. For the two different surface coverages that we propose each Ti atom is coordinated at least with four oxygens and each O atom is coordinated at least with two titanium atoms except the four one-coordinated oxygens.

The first surface coverage of sc29 is achieved by bonding each undercoordinated surface atom with one hydrogen (H) atom at distance of 1 Å and 1.75 Å from an oxygen and a titanium atom respectively [101]. The resulting NC (sc29-H), with chemical formula $(\text{TiO}_2)_{29}\text{H}_{48}$, can model the NC in extreme acidic environments but cannot attempt to restore an octahedral coordination of surface Ti atoms (see Fig. 3.1). The attempt to close the octahedron of 4-fold coordinated surface Ti atoms with two H atoms failed, as these H pairs tended to detach from the NC and go together during the relaxation process, thus we discarded this possibility. This type

of coverage can also model the exposure of dehydrated NCs to a H_2 atmosphere [30].

The second surface coverage is obtained from sc29-H by replacing hydrogens bonded to surface Ti atoms with OH groups, which we label as OH^{out} . On the other hand, we label as OH^{in} the bridging surface oxygens bonded to adsorbed H (see Fig. 3.1), since this difference will be useful in the following. One more OH group is added to each of the four Ti atoms in the square base vertices to close their octahedral coordination. We also neglected hydrogens bonded to the twofold-coordinated bridging oxygens of [001] surfaces as to ensure the stoichiometry of hydration sphere. The final NC (sc29- H_2O) has chemical formula $(TiO_2)_{29}(H_2O)_{24}$ (see Fig. 3.1). This coverage can model the NC in a moderate acidic environment, where OH groups account for the presence of functionalizing moieties which stabilize the NCs through their radicals, or be viewed as a complete dissociative adsorption of water in the first layer of the hydration sphere. Hence this covered NC is among the simplest (and also stablest) models of the first layer of the hydration sphere.

At last, we studied the desorption of single oxygen atoms from sc29. We eliminated one at a time the four one-coordinated oxygens bonded on the surface of the optimized sc29. The resulting structures will be referred to as nc29- MO , with $M=\{1,2,3,4\}$. These surface bonds are considered important reactive sites in the nanocrystalline TiO_2 activity [102].

For all the above described NCs we also computed the ionization potential (IP) and the electron affinity (EA) defined as $IP = [E(N - 1) - E(N)]$ and $EA = [E(N) - E(N + 1)]$ respectively. Here $E(N)$ represents the total energy of the neutral NC whereas $E(N + 1)$ ($E(N - 1)$) that of the negatively (positively) charged NC. A rigid shift has been applied to all the computed density of states (DOS), in such a way that $E_{HOMO} = -IP$ for each NC (E_{HOMO} being the HOMO energy).

3.2 Results and discussion: structure

In the next sections we will systematically draw a parallelism between our findings and experimental data, where available.

Table 3.1: Dimensions (Δx , Δy , Δz), volume ($V = \Delta x \Delta y \Delta z$) and volume variations ($\Delta V = (V - V_0)/V_0$, V_0 being the volume of the NC with the atoms in the ideal bulk positions) of the stoichiometric and passivated NCs. Δx , Δy , Δz are calculated as distances along the respective axes between two outermost Ti atoms.

System	Δx (Å)	Δy (Å)	Δz (Å)	V (Å ³)	ΔV (%)
bulk	7.618	7.618	9.604	557.36	-
sc29	7.253	7.261	9.361	492.99	-11.5
sc29-H	7.755	7.945	9.247	569.74	+2.2
sc29-H ₂ O	7.815	7.728	9.604	579.79	+4.0

3.2.1 NCs volume

The volume expansion or contraction of each NC has been evaluated by comparing the volume of the optimized NC with that of the NC with the atoms at the bulk positions. The volume of a given NC is computed as $V = \Delta x \Delta y \Delta z$ (Δi is the dimension along the $i = \{x, y, z\}$ axis, computed as the distance between the two outermost Ti atoms along that direction).

From Tab. 3.1 it can be seen that only sc29 has an appreciable volume contraction, -11.5% , whereas sc29-H and sc29-H₂O are slightly expanded, less than 5%. Since both trends are actually observed [13, 65], it was argued a dependence on the composition and preparation conditions [13] (for example, Li *et al.* [65] attributed the contraction to a positive pressure of hydration sphere). Our results show that the contraction is more likely a property of the bare NCs, since the two coverages induce the opposite effect (as for example observed by Swamy *et al.* [13]).

By analyzing the variations along the three crystallographic axes, we find the contraction of the bare sc29 in each direction, more pronounced in the basal plane (-4.8%) than along the z axis (-2.5%). This overall contraction is also experimentally reported by H. C. Choi *et al.* [103]. Passivated NCs show an expansion in the basal plane ($1.4 - 4.3\%$) whereas, along z , sc29-H contracts (-3.7%) and sc29-H₂O keeps unchanged, thus revealing another effect of the anisotropy of the [001] direction. This behaviour is also reported by Swamy *et al.* [13], who experimen-

Table 3.2: Experimental ranges of variation [14, 15, 16, 17, 18, 105] of Ti-O distances (Ti fixed, O up to the 5th coordination shell), Ti-Ti distances (3rd and 4th coordination shell) and coordination number (CN) in TiO₂ NCs. In parentheses the respective experimental values for the bulk are shown for comparison.

shell	atoms	distance (Å)	CN
1 st	Ti-O	1.95 – 1.72 (1.93)	5.8 – 2.8 (4)
2 nd	Ti-O	2.01 – 1.99 (1.98)	4.0 – 2.1 (2)
3 rd	Ti-Ti	3.13 – 3.02 (3.04)	3.3 – 1.5 (4)
4 th	Ti-Ti	3.88 – 3.78 (3.78)	3.0 – 0.7 (4)
5 th	Ti-O	3.88 – 3.77 (3.87)	5.0 – 4.0 (8)

tally observed an expansion of the lattice constant a and the decrease of c . Swamy attributed the small expansion to a Ti deficiency, our results show that particular surface configurations may contribute to determine this tendency. An expansion of anatase nanoparticles in water was also reported in a molecular dynamics study of S. Erdin *et al.* [104], showing that anatase NCs preferentially expand in the basal plane.

3.2.2 The bond lengths in the octahedron and distances of atomic pairs

To investigate the local order and the surface reconstruction of our optimized systems, bond length and distance distribution are analyzed. As a reference, we report in Tab. 3.2 the ranges of variation of distances and coordination numbers (CN), deduced from all experimental works to our knowledge [14, 15, 16, 17, 18, 105] (the samples in these works are prepared with sol-gel methods, with diameters ranging from 1.9 nm to 20 nm, and with nearly spherical shapes).

In Fig. 3.2 we report the Ti-O and Ti-Ti distance distribution. A dispersion around ideal bulk values (dotted vertical lines) is found as expected for strongly confined NCs, due to local disorder and reconstruction. However, while for sc29-H and mostly sc29-H₂O the peaks corresponding to the bulk distances are clearly

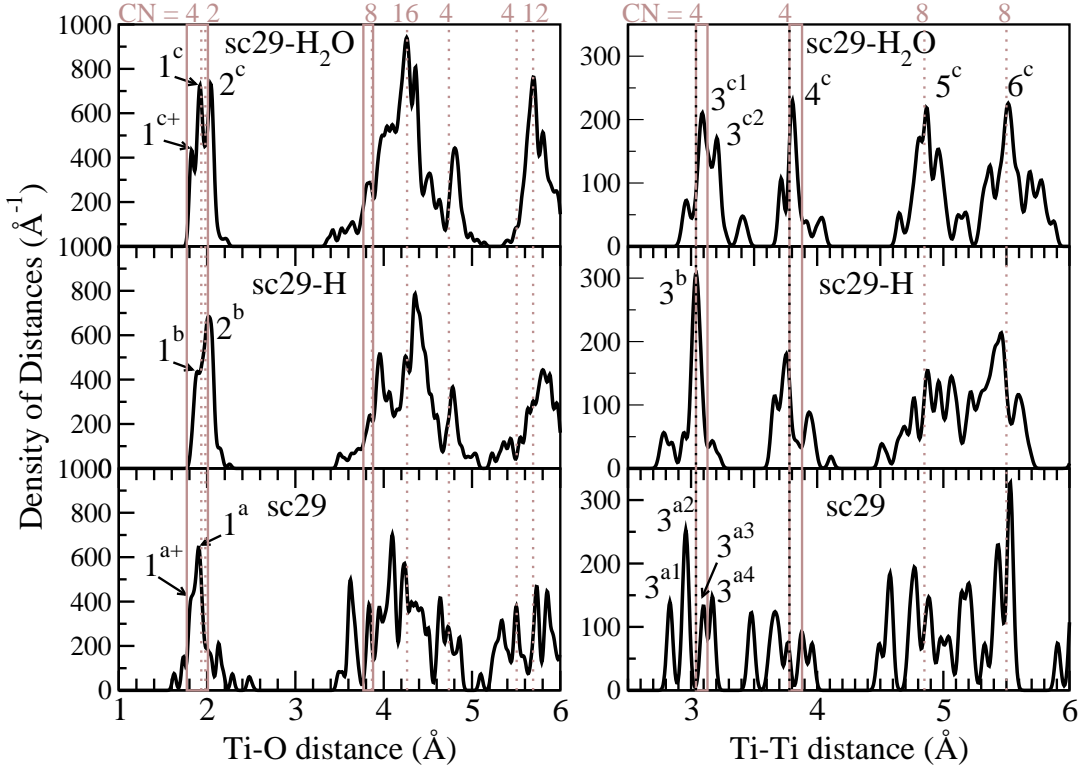


Figure 3.2: Calculated density distribution of Ti-O (left panel) and Ti-Ti (right panel) distances. Dotted vertical lines correspond to bulk distances (with the respective CN on the top). Experimental results lie within the vertical (grey) lines. The numbered peaks are described in the text. A fictitious Gaussian broadening ($\sigma = 0.03 \text{ \AA}$) is attributed to each distance to give an easier picture and each curve is normalized to the total number of distances.

distinguishable, for sc29 the distance distribution shows many more peaks. We conclude that the surface coverage stabilizes a better crystalline organization with respect to the bare NC. Experimentally, a decrease of the CN and a broadened distribution of their values are observed (see Tab. 3.2). The peaks 1^a , 1^b , 1^c of Fig. 3.2 reveal that the Ti-O first shell tends toward contraction in all of the NCs, in agreement with experimental findings [14, 15]. This is more evident for sc29, for which most of the distances are less than 1.93 \AA and the second shell does not show up as a sharp peak. In sc29-H the decrease of the Ti-O first shell bond length is less pronounced and it is contrasted by an increase of bonds in the range of the

second shell (peak 2^b). The decrease of the first shell length in sc29-H₂O is as well contained (peak 1^c) except for an amount of bonds shaping the peak 1^{c+} at the shortest distances.

Experimental samples show a reconstructed octahedron with three short and three long bonds [17, 18], whereas for the bulk anatase 4 short and 2 long bonds are found (4:2 ratio). To address this point we considered as Ti-O first shell all the bonds shorter than 1.95 Å (average of the first and the second shell length), hence the longer bonds as Ti-O second shell. We find that the bare sc29 is closest to the bulk ratio with 2.23, sc29-H is unbalanced to 0.56, whereas sc29-H₂O is the closest to experimental samples with 1.05.

Higher Ti-O shells are not experimentally analyzed since it is difficult to fit diffraction patterns for small NCs. However, sc29 shows a general trend of CN decreasing and distance contraction (larger disorder), whereas sc29-H and, to a larger extent, sc29-H₂O main peaks are close to the bulk values (thus ensuring a better structural organization, see Fig. 3.2).

In the Ti-Ti third shell variation, longer distances [14, 16] and a decreased CN with respect to the bulk distance are experimentally observed [17, 18, 103]. The bare sc29 shows a pronounced decrease of CN (see Fig. 3.2, peaks 3^{a1} - 3^{a4}). The hydrogenated sc29-H is the closest to the bulk-like behaviour, with a single well defined peak (3^b) at the bulk value. The hydrated sc29-H₂O has two main peaks (3^{c1} , 3^{c2}) at longer distances than the bulk value, which do not cause an excessive decrease of the CN, thus reproducing both experimental findings.

The observed Ti-Ti fourth shell slight expansion [16] is best reproduced by sc29-H₂O with its main peak (4^c). Higher Ti-Ti shells are broadened but hydration keeps distances at the bulk values better than the other surface configurations (see Fig. 3.2, peaks 5^c and 6^c).

In conclusion, the water coverage (representative of moderate acidic environment) is the best model for real NCs, since it is capable to intercept all experimental findings whereas full hydrogen coverage (representative of extreme acidic environment) shows an overestimation of experimental trends. The overall trend for the bare NC is toward contraction and to a more disordered reconstruction. Moreover the two simple surface coverages proposed in this chapter as models of two configurations of the hydration sphere are able to preserve a bulk structure of the NCs

better than their bare counterpart. This conclusion is in agreement with the results of a molecular dynamics study by V. N. Koparde *et al.* [106].

Finally, to explain the two main experimental findings, i.e. the decrease of the first shell Ti-O bond and the equality of the first and second shell CN, the contributions of different atomic pairs to the peaks of Fig. 3.2 can be separated out. From this analysis on sc29-H₂O, we find that: (i) bulk oxygens (3-fold coordinated) faithfully reproduce the 2:1 ratio of the distances in the bulk octahedron, thus other oxygens are the source of experimental variations; (ii) the increase of the second shell CN is entirely caused by surface (H-bonded) oxygens; (iii) oxygens coming from covering hydroxyl groups determine the first peak at 1.83 Å (peak 1^{c+}). We thus find that OH^{out} radicals, adsorbed on the surface of NCs, are the main source of the first shell contraction actually observed [14, 15]. On the other hand, the experimental evidence of the 1:1 ratio of the first two shells [17, 18] can be entirely ascribed to chemisorption of OHⁱⁿ groups (see Fig. 3.1). Thus we can clearly link the two main experimental variations to two different sources, that is the adsorption of two kinds of OH groups on the NC surface. At last, isolated and then highly reactive oxygens, possibly present on the NC surface, may produce the shortest bonds (< 1.79 Å [15]) as shown for sc29.

As a final remark, we point out that the adsorption of hydrogen gives rise to bonds with a very narrow distribution (with a 0.03 Å range). The sc29-H shows a mean Ti-H distance of 1.72 Å, slightly smaller than the initial value of 1.75 Å. The O-H bond mean value is 0.98 Å for all NCs (slightly reduced with respect to the initial value of 1.00 Å), in agreement with the result of Erdin *et al.* [104].

3.3 Results and discussion: electronic properties

3.3.1 From crystal to NC

In this section we discuss the electronic properties of the NCs by analyzing the DOS, the DOS projected on the atomic orbitals (PDOS) and charge density plots. First of all, we compare the electronic properties of the bare sc29 NC with those of the bulk. The electronic levels span four energy ranges, well separated by energy gaps (panels (a) to (d) in Fig. 3.3).

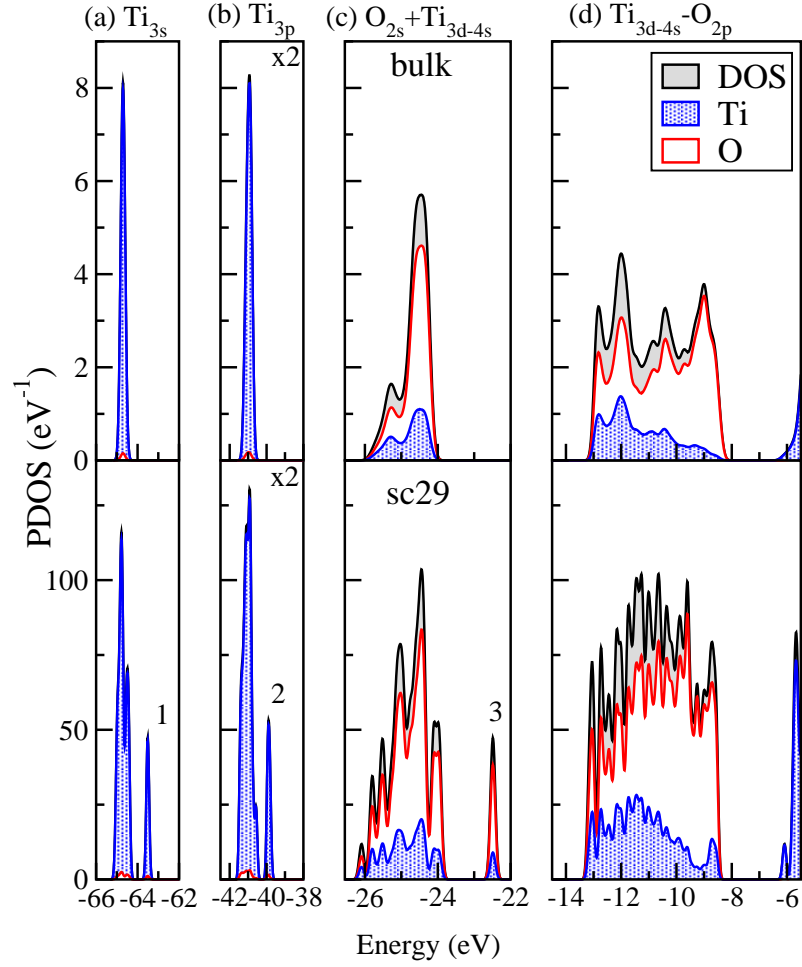


Figure 3.3: DOS and PDOS for bulk anatase TiO_2 (top panels) and the sc29 NC (bottom panels). The peaks labelled 1 to 3 are discussed in the text. The four occupied groups of levels and their respective atomic character are labelled on the top. The alignment has been performed by shifting the HOMO level of the cluster to the calculated value of the ionization potential. For graphical purposes the bulk DOS is shifted so as the top valence band matches the sc29 HOMO energy. DOS and PDOS curves are calculated by assigning a Gaussian broadening of 0.1 eV to each Kohn-Sham energy level.

The first (Fig. 3.3(a)) and second (Fig. 3.3(b)) group of levels have a very dominant Ti 3s and Ti 3p atomic character, respectively, thus they can be considered semicore states that do not take part significantly to the chemical bond with oxygen

atoms. For sc29 these two groups of levels span an energy range of 0.60 eV and 0.88 eV respectively, larger than the respective range in the crystal (higher panels in Fig. 3.3, 0.07 eV and 0.65 eV respectively). This apparently contradicts an expected narrowing due to the quantum confinement. Actually, this occurrence can still be attributed to the reduced size, enhancing the role of the surface. This can be inferred from the detached peaks at higher energy present in the first three groups of levels of the NC (see Fig. 3.3, bottom panels, peaks 1, 2, 3). The peaks 1 and 2 belong to the titania bonded to the four one-coordinated oxygens on the surface, while the peak 3 is due to those oxygens. The peak 2 can be connected to the results recently obtained by A. G. Thomas *et al.* [107] on resonant photoemission measurements of the Ti 3p electronic states of the anatase [101], [001] and rutile [110] surfaces. In that case, the Ti 3p related states have a tail at lower binding energy than the bulk peak. The tail is ascribed to the outermost Ti^{3+} atoms of oxygen deficient or defective surfaces. In our case they are related to the interaction of Ti atoms with one-coordinated surface oxygens, for which a double bond nature is suggested [15]. The desorption of these oxygens (nc29-MO NCs, see Fig. 3.1) leads to the progressive approaching of the peak to the bulk peak and an increasing number of occupied Ti 3d states, whose nature will be discussed later.

The third group of states has a dominant O 2s atomic character and shows hybridization with the Ti_{4s-3d} atomic orbitals. Its width is even in this case larger for the NC (2.14 eV) than for the crystal (1.47 eV).

The last occupied group has the hybrid $\text{Ti}_{4s}-\text{O}_{2p}$ and $\text{Ti}_{3d}-\text{O}_{2p}$ characters. In this case the group widths are similar, 4.50 eV for the crystal and 4.63 eV for sc29, and can be compared with the experimental value for bulk anatase of 4.70 eV [108].

The Q-size effect is better shown in the last two groups by the presence of narrower and sharper peaks in the DOS and most of all by the widening of the band gap. The anatase crystal is an indirect semiconductor with the first transition ($\text{M} \rightarrow \Gamma$) at 3.2 eV. Our calculation on the anatase crystal gives a gap of 2.13 eV which well compares with other theoretical works based on the DFT [109], but it is clearly an underestimation of the real band gap (this is an usual shortcoming of DFT). The HOMO-LUMO gap in the NC is 2.46 eV showing a blue shift of 0.33 eV. The first group of empty states has a dominant Ti 3d character at the onset with an increasing O 2p hybridization character for both systems. From this first analysis

we deduce that, in the range of 1 nm, two different effects, which can be competing, show up: the Q-size effect is present due to the reduced size but the spreading of the states all over the system makes them influenced by the surface structure. The overall behaviour of the electronic states is thus the result of the two effects.

3.3.2 Effects of the surface coverage

The main difference introduced by the surface coverages in the two semicore groups of levels is the absence of the detached peaks observed in sc29. They are ascribed to the Ti atoms bonded with the one-coordinated oxygens on the [001] surfaces (see Fig. 3.4, bottom panels, peaks 1, 2, 3). These oxygens are H-bonded for both coverages, thus becoming 2-fold coordinated.

The third group of levels (see Fig. 3.4(c), dominant atomic character O 2s) is strongly affected by the surface bonds. For both coverages, the levels mainly related to H-bonded oxygens (group of peaks A, C) are all located at higher binding energies than those related to unsaturated oxygens (group of peaks B, D). At variance, in sc29, the levels related to undercoordinated surface oxygens (the H-bonded ones in sc29-H) are all located at lower binding energies. Thus the surface coverage induces a level shift of these O 2s orbitals to higher binding energies than those related to bulk-like oxygens.

The most interesting changes concern the higher energy valence levels [see Fig. 3.4(d)], as explained in the following:

O-H bonds. Both sc29-H and sc29-H₂O do show, in this energy range, a subgroup of levels with higher binding energies than those related to the (bulk-like) Ti-O bonds. Such subgroups are labelled E and G in Fig. 3.5 and are ascribed to the O_{2p}-H_{1s} chemical bond. From a deeper analysis of the subgroup G in sc29-H₂O, it turns out that the higher binding energy levels are due to O-H bonds within chemisorbed OHⁱⁿ, whereas the lower binding energy levels are due to chemisorbed OH^{out} radicals. Thus, it is possible to distinguish the effect of the two types of chemisorbed OH radicals in stabilizing the electronic levels, as it happens for the structural reconstruction of the octahedron (see Sec. 3.2).

Ti-H bonds. Hydrogen coverage produces an occupied subgroup of states in the forbidden bulk gap (labelled F in Fig. 3.4(d)), just above the (bulk-like) Ti-O

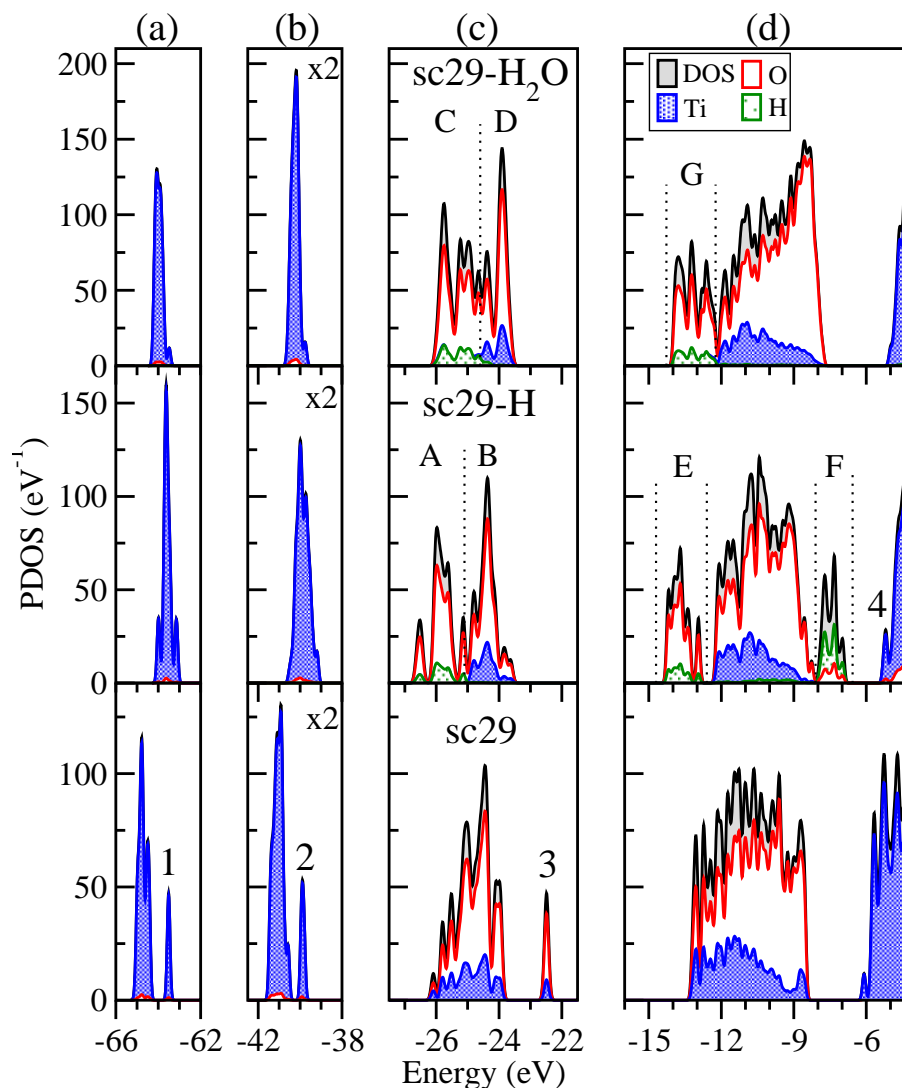


Figure 3.4: DOS and PDOS for sc29 (bottom panels), sc29-H (middle panels) and sc29-H₂O (top panels). The four groups of occupied levels are labelled on the top, panels (a) to (d). The numbered peaks (1,2,3,4) are discussed in text. Vertical dotted lines highlight the groups of levels (A to G) discussed in the text. A rigid shift has been applied to the DOS of all the NCs to bring the HOMO energy to the value of the computed ionization potential.

valence band (VB) states, whereas the hydrated sc29-H₂O results in a significant increase of the DOS below the (surface) O 2p HOMO energy. The subgroup F

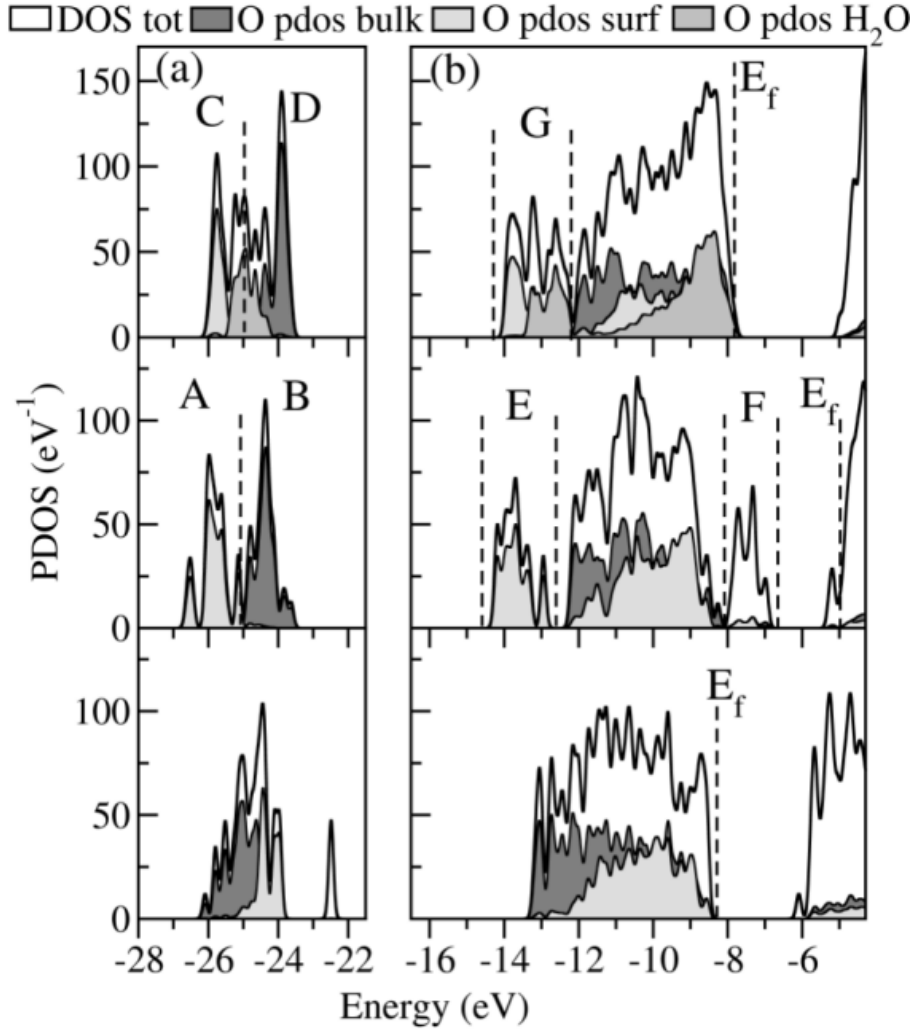


Figure 3.5: Total DOS and PDOS projected on oxygen atoms for sc29 (bottom panels), sc29-H (middle panels) and sc29-H₂O (top panels) [110]. The two groups of occupied levels are labelled on the top, panels (a) and (b). Vertical dotted lines highlight the groups of levels (A to G) discussed in the text. The legend on the top defines the oxygen position in the NCs, i.e. O from the bulk (dark grey), O from the surface (OHⁱⁿ, light grey), O from the water molecule (OH^{out}, grey).

is substantially related to the Ti_{3d-4s}-H_{1s} chemical bond, absent in the bare and hydrated NCs. Therefore, the reduction of Ti atoms promoted by the formation of Ti-H bonds leads to the opposite effect with respect to the Ti-OH bond: occupied

states show up at lower binding energy than the typical top valence states of TiO_2 (antibonding O 2p derived bands). This effect can be a source of a possible red shift of the band gap, eventually hiding the blue shift caused by the Q-size effect. The very presence of these subgap states shows that the hydrogen coverage does not provide an ideal hydrogen passivation of the system. Indeed, in bulk TiO_2 , Ti is in the formal oxidation state 4+ and sixfold coordinate, resulting in a donation of 2/3 electrons per bond. In this way the hydrogen coverage is not a truly passivation, as it results in the reduction of Ti instead of an ideally expected oxidation. The gap between the top (bare-like) occupied level and the onset of the subgroup F is 0.35 eV. Similar intra-gap states have been actually observed and ascribed to the hydration sphere, whose Ti-OH and Ti-H₂O bonds have induced occupied states above the VB of about 0.6 eV and 0.54 eV respectively [58]. On the contrary, our results show that Ti-OH bonds do not induce states in the gap but they stabilize states to higher binding energies than the VB. The intra-gap states do depend from possible Ti-H bonds which can be formed on the surface of the NCs, for example due to the steric hindrance of the same hydration sphere.

3.3.3 Band gap

The blue shift obtained for the bare NC (0.25 eV) is enhanced in sc29-H₂O, showing a forbidden gap of 2.83 eV (i.e., a blue shift of 0.70 eV). We expect that the Q-size effect can be detectable in stoichiometric TiO_2 NCs and, mostly, it can be preserved by some configurations of the hydration sphere. In fact, the experimentally observed blue shift is sometimes ascribed to direct allowed transitions [22, 24] in an otherwise indirect semiconductor, but our results show that even the direct transition is blue shifted. Of course the small exciton radius of TiO_2 ($R_{ex} \sim 1$ nm) [22] makes difficult the detection of Q-size effects, since it requires the synthesis of very small NCs. Furthermore, such NCs may show properties strongly dependent on the structural relaxation, the crystal purity and the surface properties. Our results are in agreement with the very recent experimental work of Satoh *et al.* [67], who have observed band gap blue shifts in the range 0.22 – 0.69 eV for anatase NCs with diameters in the range 1.64 – 1.02 nm. These authors have also pointed out the importance of crystallinity on the Q-size effects, as they have detected different blue

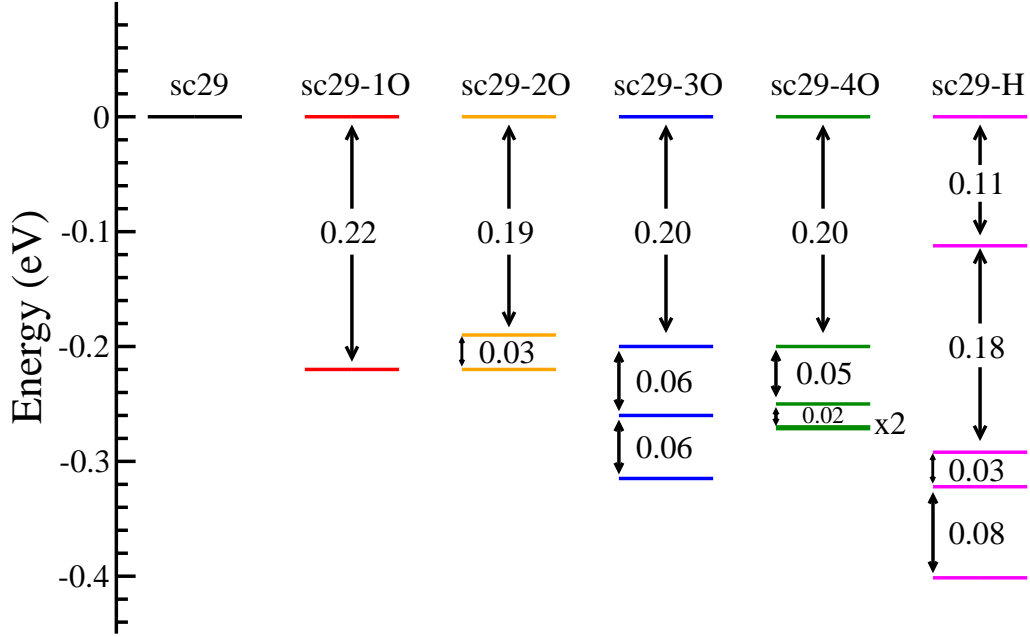


Figure 3.6: Scheme of the intra-gap energy levels of the hydrogenated and O deficient NCs. All LUMO energies are placed to 0 eV for graphical purposes. The HOMO-3 level of sc29-4O is double degenerate, as indicated by the label.

shifts ascribable to rutile and anatase NCs of comparable dimension. In our case, this dependence on the structural organization is linked to the surface coverage, as it is capable to preserve a better crystallinity (see 3.2). In fact the blue shift of the hydrated NC (0.70 eV) is closer to the experimental value (0.69 eV) with respect to the bare sc29 (0.33 eV).

In Fig. 3.6 we sketch some examples of the different phenomena which do occur with other surface configurations. The hydrogen coverage of the bare NC leads to the presence of four occupied energetic levels near the conduction band (CB) (see Fig. 3.4(d), peak 5), which considerably reduce the gap to 0.11 eV. In the same way the progressive desorption of the one-coordinated oxygens from the [001] surface leads to NCs (nc29-MO, $M=\{1,2,3,4\}$) with an energy gap of about 0.2 eV and an increasing content of occupied states near the CB, whose occupation number is always twice the number of desorbed oxygens.

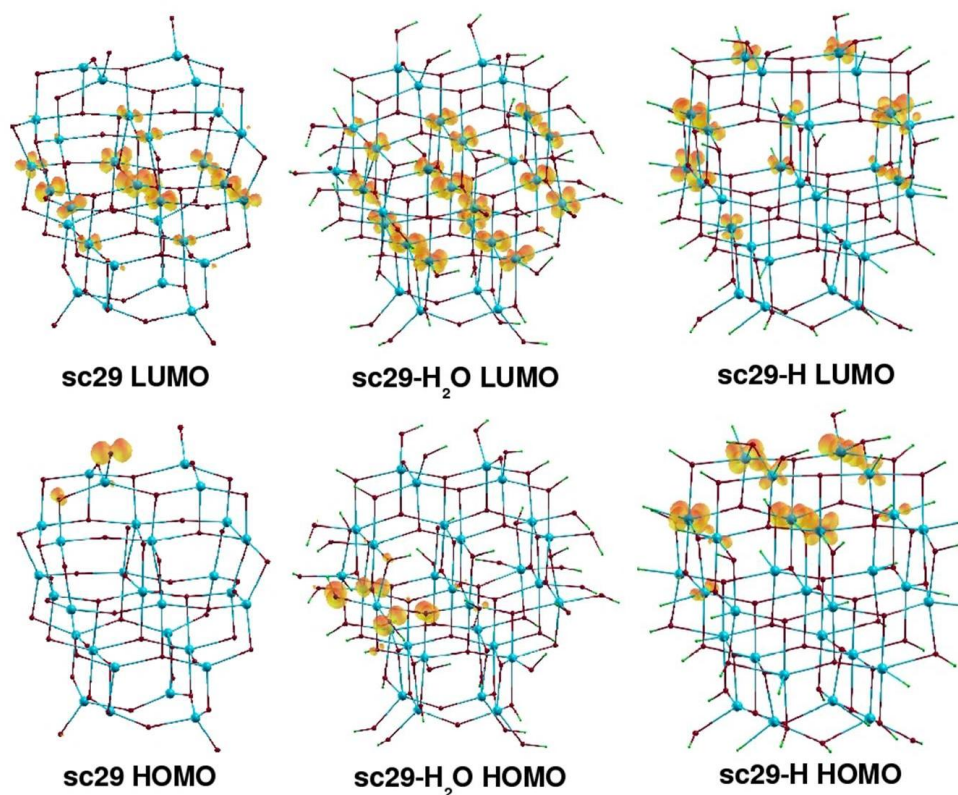


Figure 3.7: Charge density contour plots of the HOMOs and LUMOs states of stoichiometric NCs. The contours correspond to 10% of the maximum value.

3.3.4 HOMO-LUMO states

In this section we comment on the spatial distribution of the HOMO, LUMO and the intra-gap states of the hydrogen covered sc29-H and substoichiometric nc29-MO NCs respectively. The knowledge of these key features can help in understanding the photoactivity of TiO_2 NCs since the location of reactive sites and the pathways of charge transfer are originated by the overlap of the wave functions and by the energetic proximity among excitable and available single states.

HOMO and LUMO charge density contour plots are depicted in Fig. 3.7. The sc29 HOMO originates from an O 2p orbital, which is also typical of the valence band maxima of TiO_2 crystals [108]. It is a localized surface state and no hybridization with Ti orbitals occurs (see Fig. 3.7). Similarly, the sc29-H₂O HOMO is O 2p

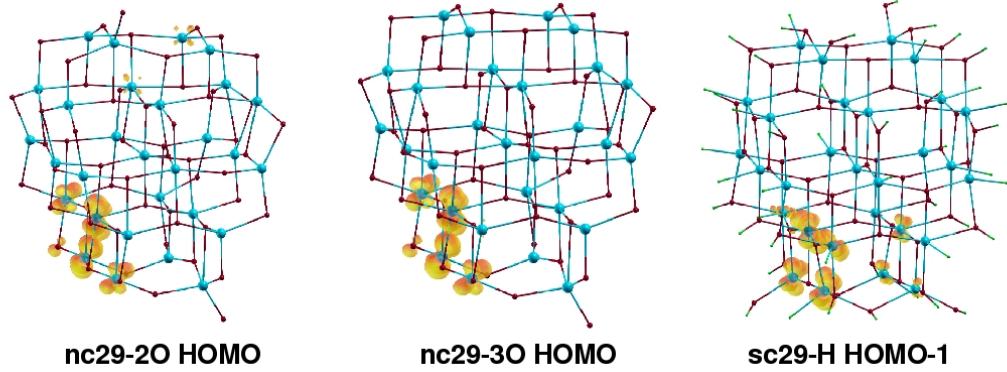


Figure 3.8: Charge density contours plots of some occupied states of O-deficient or hydrogenated NCs. The contours correspond to 10% of the maximum value.

in character but its spatial distribution is affected by the degeneracy of the highest occupied energetic levels, as previously shown in Fig. 3.4. On the contrary, the sc29-H HOMO shows an exclusive Ti 3d character and its spatial distribution involves Ti atoms localized in a restricted region of the NC. In general, the Ti 3d orbital character of electronic states is due to free CB electrons [108], to defect sites caused by oxygens deficient structures [107] or to photogenerated traps [111, 112]. The oxygens vacancies can determine intra-gap occupied states immediately above the VB [108] or below the CB edge [82]. In our case, the sc29-H HOMO is a defect state just below the conduction levels (HOMO-LUMO gap is 0.11 eV, see Fig. 3.6). It is worthwhile to note that this result can be linked to the very recently observed formation of Ti 3d occupied states, in the dark and at low temperatures, due to the hydrogen coverage of NCs [29, 30]. The other three occupied states below this HOMO also have Ti 3d character and are localized in the region of one the two [001] surfaces (see as example the HOMO-1 level in Fig. 3.8). It is interesting to note that the Ti atoms involved in these states are indifferently bonded to hydrogen or oxygen.

All the LUMOs have Ti 3d character, as expected for the TiO₂ conduction levels [108] but the spatial distribution of the sc29-H LUMO differs from the others, since it involves only the outermost titania (see Fig. 3.7 top right). The sc29 and sc29-H₂O LUMOs are delocalized in the bulk, showing Ti 3d levels spread either all

over the structure (sc29-H₂O) or on a 'bulk' plane of Ti atoms (sc29). On the contrary, sc29-LUMO is surface delocalized as for two-dimensionally delocalized shallow traps [82, 113, 114]. This information can be particularly useful for the synthesis of TiO₂ nanofilms built up of NCs, whose conductive properties are liked to be tuned.

Another result concerns the four defect states of sc29-H, namely HOMO-3 to HOMO. We can infer that the reduction of the bare NC with hydrogens does not produce any charge transfer from the Ti 3d defect sites to the nearest hydroxylic groups if we consider these aspects: (i) the difference between sc29-H and sc29-H₂O is the substitution of the Ti-H bonds with Ti-OH ones; (ii) the defect sites are absent in the hydrated sc29-H₂O, thus unveiling the electron donor behaviour of hydrogens in sc29-H; (iii) the defect sites involve titania of Ti-H as well as of Ti-OH bonds; (iv) there is no hybridization of the defect sites in sc29-H with H 1s orbitals, on the contrary they show a pure Ti 3d character. This occurrence was reported by M.A. Henderson *et al.* [115] on measurements regarding the TiO₂ [110] surface, where the charge transfers from the defective Ti 3d to the bonded hydroxylic group only. This result also confirm that surface Ti-OH species are unlikely to be electron donors as it has been recently reported [29]. This information can be useful to understand the electronic pathways in the photocatalytic activity of TiO₂ NCs.

The desorption of the four one-coordinated oxygens from the bare sc29 produces defect sites below the conduction levels. The number of such sites equals the number of desorbed oxygens (see Fig. 3.6). They are all Ti 3d in atomic character and are localized on the surface region surrounding the desorbed oxygens (see Fig. 3.8). The electron scavenging action of adsorbed oxygens involve, at first, deep defect sites and then shallow energy sites, thus narrowing and quenching the distribution of defect states below the CB. An analogous result is reported by L. de la Garza *et al.* [116], who observed a progressive removal of surface sites of TiO₂ nanoparticles by increasing the concentration of dopamine, which restores the octahedral coordination of surface Ti atoms with its OH bidentate ligands.

Table 3.3: Formation energy (E_f), passivation energy (E_p), formation energy per TiO_2 unit (E_f/N) and adsorption energy per passivating molecule (E_p/M). The values are obtained from Eq. 3.1 and Eq. 3.2 and are all expressed in eV.

System	E_f	E_f/N	E_p	E_p/M
sc29	-140.37	-4.84	-	-
sc29-H	-130.02	-4.48	10.35	0.43
sc29-H ₂ O	-164.03	-5.66	-23.66	-0.99

3.4 Formation energies

The formation energy of a given NC is defined by

$$E_f = E_{tot} - M_x \cdot \mu_x - N \cdot \mu_{\text{TiO}_2} \quad (3.1)$$

where E_{tot} is the total energy of the system, M_x is the number of covering molecules having chemical potential μ_x ($x=\text{H}_2$; H_2O), N is the number of TiO_2 units (with chemical potential μ_{TiO_2}). The chemical potentials are chosen as the total energy of the correspondent isolated molecules.

The energy required to cover the surface with adsorbates, referred to as passivation energy with respect to the bare NC sc29, is defined by

$$E_p = E_{tot} - M_x \cdot \mu_x - E_{tot}^{\text{sc29}} \quad (3.2)$$

where E_{tot} is the total energy of the covered system, E_{tot}^{sc29} is the total energy of the bare sc29 and M is the total number of covering molecules. All data are shown in Tab. 3.3.

All NCs have negative formation energies (column E_f). The highest E_f per TiO_2 molecule is -4.48 eV of sc29-H, while the lowest is -5.66 eV of sc29-H₂O (column E_f/N). The passivation energy with molecular hydrogens costs 0.43 eV per H_2 molecule, while dissociative adsorption of molecular water is -0.99 eV per H_2O molecule (column E_p/M).

The hydrated NC is the most stable and this is consistent with our initial assumption that truncated bipyramidal morphologies are characteristic of moderate

Table 3.4: Calculated electron affinity (EA) and ionization potential (IP) of all the TiO₂ NCs.

System	EA (eV)	IP (eV)
sc29	3.72	8.55
nc29-1O	3.52	6.39
nc29-2O	3.35	5.95
nc29-3O	3.17	5.78
nc29-4O	3.06	5.63
sc29-H	2.71	4.98
sc29-H ₂ O	2.83	7.82

acidic aqueous solutions. The stabilizing role of dissociative adsorption of water on the overall energetics of nanophase samples has been observed [74] and it has been also suggested by theoretical works [104].

The desorption energy ΔE_O of an oxygen atom, one-coordinated on the surface of sc29, is calculated from

$$\Delta E_O = \left(E_M^{tot} + \frac{M}{2} \cdot \mu_{O_2} - E_{sc29}^{tot} \right) / M \quad (3.3)$$

where $M=\{1,2,3,4\}$, E_M^{tot} is the total energy of nc29- MO , μ_{O_2} is the chemical potential of a spin polarized isolated oxygen molecule and E_{sc29}^{tot} is the total energy of sc29. The result is 3.47 eV for each oxygen, which shows that the stoichiometric NC is the most stable, that these oxygens sites are independent and lastly that oxygen desorption from these NCs is unfavourable. It should be pointed out that the four oxygens are one-coordinated to the surface Ti atoms which became 4-fold coordinated in this way, thus ensuring a better stabilization of undercoordinated titanium atoms with strong bonds.

Using the Makov-Payne correction for charged systems [117] we calculated the electron affinity (EA) and the ionization potential (IP) of our NCs, with results shown in Tab. 3.4. The sc29 ionization potential of 8.55 eV is in the range of values of 8.37 – 9.98 eV calculated by Z. Qu and G-J Kroes [118] for TiO₂ NCs composed

by up to 15 molecular units, whereas its electron affinity of 3.72 eV is between the adiabatic and vertical detachment energy, 3.6 – 4.80 eV, measured by H-J Zhai and L-S Wang [119] on an anionic $(\text{TiO}_2)_{10}$ NC. Progressive oxygen desorption from sc29 lowers more and more both the electron affinity and the ionization potential and can be rationalized as the effect of the presence of defective electronic states, near in energy to empty conductive states. This trend is confirmed by hydrogen covered sc29-H, which as well presents defective states. Hydrated sc29- H_2O shows a high ionization potential of 7.82 eV, which can be connected to that of sc29, but a low electron affinity of 2.83 eV, which is close to that of sc29-H.

3.5 Conclusions

We performed DFT calculations on TiO_2 NCs with different surface coverages, modelling different synthesis conditions. From a thorough analysis of the experimental findings we identified the relevant ranges of variation of the main structural and electronic properties. The comparison with our calculations allowed us to interpret some controversial properties of TiO_2 NCs. The main properties that we highlighted are summarized in the following.

1. The bare stoichiometric NC undergoes a global structural contraction whereas surface coverage induces volumetric expansion. The contraction of sc29 occurs in each direction, thus the same trend is expected for TiO_2 NCs not subjected to an external pressure. On the contrary, the interaction with adsorbates produces an expansion which is more evident along the basal direction than on the $[001]$ surfaces. This explains the observed expansion of the cell parameter a and the slight contraction of c .
2. All the NCs show the contraction of the first shell Ti-O bond length, but only hydration leads to a 1:1 ratio of the first and second shell coordination numbers, i.e. the observed rearrangement of the Ti-O bond lengths in the octahedron. Thus, from the hydrated NC, we link these two results to two surface bonds of different nature: (i) Ti-OH bonds, with the hydroxylic radical adsorbed *on* the undercoordinated Ti of the surface, lead to short Ti-O bonds;

- (ii) OH, adsorbed *in* the surface of NCs as bridging groups between Ti atoms, induce long Ti-O bonds.
3. The surface coverage prevents a pronounced reconstruction of the surface, thus leading to a more bulk-like organization of the whole structure. In particular, the hydrated NC more closely reproduces the observed variations with respect to the bulk structural properties.
 4. The small exciton radius of TiO_2 ($R_{ex} \sim 1$ nm) [22] makes difficult the observation of Q-size effects. Our NCs are thus well suited ($2R_{NC} \sim R_{ex}$) to detect such possible effects. In fact, the quantum confinement of the electronic states can be deduced from the tendency to discretization of the electronic levels and from the blue shift of the band gap. This shift and the shape of the DOS depend on the NC crystallinity, since we showed that each surface coverage induces a different local and hence global spatial reconstruction. Such result agrees with recent experimental observations [67]. However the decrease of the NC dimension down to the nanoscale enhances the surface role, as well. Hence, Q-size effects can be hidden in presence of particular surface morphologies. For example, hydration stabilizes all the dangling bonds to higher binding energies than the valence states of the NC, whereas the chemical reduction of the same NC with hydrogen coverage induces intra-gap states. Furthermore, the surface configuration affects the energy distribution of the electronic states down to the semicore states.
 5. Occupied electronic states in the range 0.11 – 0.40 eV below the conduction levels are induced by oxygen desorption and reduction with hydrogen of titanium atoms. These states are Ti 3d in atomic character and are spatially localized in restricted regions of the NCs. Adsorption of oxygen decreases the number of these states from the deepest energetic levels on, similarly to the effect induced by dopamine bidentate ligands on defect sites [116]. No complete charge transfer occurs from these defect sites to the hydroxylic groups, as experimentally observed for surfaces [115].
 6. At last, the hydration leads to the most stable NC. This is consistent with the experimental evidence that truncated bipyramidal NCs are characteristic

of moderate acidic environments and that the first layer of water coverage on TiO_2 nanosamples is preferentially constituted of dissociated water. Oxygen adsorption is as well favoured, since it restores the octahedral coordination of surface titanium atoms.

Chapter 4

TiO₂ 1D nanowires

A main focus of the modern material research relies on the efficient tuning of the peculiar properties emerging at nanoscale to ultimately enhance specific processes of interest. A striking example in this field is represented by the huge efforts in controlling and tailoring the performance of TiO₂ functional nanodevices, boosted by the relevant social and commercial rebounds of their applications. Actually, zero-dimensional (0D) TiO₂ nanoparticles (NCs) and one-dimensional (1D) nanowires (NWs) share the same benefits from having larger surface area, more active sites, and quantum confinement related properties which eventually lift the rates of their activity [8, 31, 32, 120, 121, 33, 122, 123]. 1D nanotubes, nanorods, and NWs are sometimes polycrystalline assemblies of NCs [34, 124, 125, 126, 127], hence the elementary physical properties can overlap. The main feature that can distinguish 1D TiO₂ nanostructures from their 0D counterpart is a better ability to transport (photo)generated charges away from possible (recombination) reaction sites, thus revealing the heavy attention they are receiving for applications in photovoltaic cells, sensors, electrodes, and optoelectronics [128, 129, 130, 35, 131, 132].

Theoretical investigations may fill the gap through the atomistic modeling of TiO₂ nanostructures, by proposing the fundamental understanding of the physical properties behind the observed mechanisms at the nanoscale. Despite the example of the well characterized 1D nanomaterials like silicon and carbon, a very scarce literature is directly focused on the study of TiO₂ 1D nanostructures up to now. Enyashin *et al.* [36] proposed a model describing the stability of (anatase and de-

hydrogenized lepidocrocite-based) nanotubes, nanorolls, and nanostrips of TiO_2 as a function of the radius, by using a density-functional-based tight-binding method. They also reported the convergence of the band gap to the bulk value for radii of about 25 Å, but without considering the effect of the surface interactions with environment species. Allen [133] speculated on the geometric construction of 1D formula units which can take advantage of the translational and rotational symmetries to design dipole-free, charge-neutral, and minimal surface polarized rutile and anatase NWs. Alvarez-Ramirez *et al.* [37] performed ab initio molecular dynamics calculations to determine the transformation mechanism of anatase wires in titanate-type structures, highlighting the important factor played by the adatoms which mimic the environment interactions. Zhang *et al.* [38] tested the stability of the two thinnest TiO_2 NWs assembled from dimeric Ti_2O_4 molecules as basic building blocks, within the density functional theory (DFT) approach. At last, Meng *et al.* [39] have recently shown the ultrafast electron injection from a dye molecule to anatase NWs by means of time-dependent DFT.

The aim of this chapter is to investigate the dependence of the structural, electronic, and stability properties of anatase TiO_2 NWs as functions of the surface coverage, of the diameter size, and of the morphology, within the framework of first-principles DFT calculations. It is experimentally possible to synthesize TiO_2 NWs starting from NC as building blocks, one possible elongation of the chain being the [001] direction [57, 21, 134]. We took advantage of our previous study on TiO_2 NCs to construct the bare NW presented in this chapter, which is cut by the (100) and (010) planes and periodic along the [001] axis. We then defined an analogous NW with a larger diameter to verify the trends in size of the calculated properties. Both NWs were then covered with simple water-derived species to simulate two different environments in which they could be synthesized or catalyze reactions. A second type of NW periodic in the [010] direction and with lateral surfaces derived from cutting by the (001) and (101) planes, was compared to the previous ones to find peculiarities related to the geometric arrangements. The following points summarize the main findings which are going to be unraveled:

- Terminal atoms of the surface are directly involved in the photocatalytic processes, since both charge transfers and bonds occur at the interface. The structural organization of these atoms is different with respect to the ideal bulk configuration

because of the truncation of the crystal field. This difference sums to the specific properties of each surface thus determining the final behaviour in terms of chemical stability and catalytic efficiency. The presence of edges, corners, and different local arrangements in nanomaterials can affect the overall features more significantly than in the macroscopic samples. Nevertheless, to the best of our knowledge, there are no available data on the atomic displacements and reconstructions at the TiO_2 NWs surface. It should also be considered that the smallest diameters (1-6 nm) [58, 135, 31, 63, 79, 136, 137, 138] of 1D nanostructures are in the same range of the 0D NCs for which surface distortions are reported [139, 16, 17, 18]. Through total energy optimizations we show the effects of the surface reconstruction on the whole crystallinity of the NWs in Sec. 4.2.

- Scaling the dimension down to the nanometer range should lead to quantum size effects, as the band gap blue shift. It could contribute to improve the charge transfer between the NW and the reactive species if a proper line-up of the valence band maximum (VBM) for holes or conduction band minimum (CBM) for electrons, with respect to the redox couple potentials, is satisfied. The anatase TiO_2 crystal is an indirect semiconductor and the onset radius of 0D NCs at which the blue shift is detectable, as well as the nature of the transition, has been a matter of debate [22, 23]. The exciton radius is reported in the range 0.35 – 1.9 nm [22, 75] while the effective mass for hole and electron is not unambiguously determined [22], such that even the effective mass approximation has been considered arguable for small TiO_2 NCs [23]. It follows that some NCs are blueshifted in the range 1 – 10 nm [76, 77, 78, 67], while others show the bulk band gap down to 1.5 nm [22, 23]. The same controversy stands for 1D NWs, whose diameter acts as the confinement direction. However, a better crystallinity should preserve a more ideal behaviour against the effects of the preparation methods and surface environment, hence blue shifts of 0.1 – 0.5 eV are reported for TiO_2 1D nanostructures in the diameter range of 2–9 nm [33, 79, 80, 81]. We discuss in Sec. 4.3 the electronic properties of the NWs through calculations of the density of states (DOS) and of the charge density distribution of the states. A line-up of the bands energies of the NWs will elucidate the effect of the size, of the surface configuration, and of the morphology on the NW ability to photocatalyze reactions.

- Nanostructured TiO_2 is widely investigated for large scale hydrogen production

from water splitting and as hydrogen sensor [122, 140, 95, 40, 42, 141]. These relevant outcomes need a systematic understanding of the interaction of the water constituents with the surface of TiO_2 NWs. Among different synthesis techniques, solvothermal and hydrothermal methods can lead to NWs with water-capped surface, mainly because of the presence of hydroxylated terminations [81, 142]. Several photocatalytic reactions of TiO_2 nanostructures are performed in aqueous media, hence a considerable number of hydroxyl groups adsorbed on the surface can play an important role in the activity of the nanostructures [79]. The presence of a hydration sphere is usually observed to surround TiO_2 NCs, with a dissociative adsorption of the first water layer to prevail due to the ability to fill surface vacancies in the synthesis process [28, 74]. We thus considered the coverage of the bare NWs with simple water derived adsorbates, modeling the surface configuration in the presence of hydrogen and hydration. We discuss in Sec. 4.4 the deep influence that the surface functionalization plays in determining the overall structural, electronic and stability properties of these 1D NWs.

4.1 Methodology

4.1.1 Computational details

All *ab initio* calculations are performed within the DFT framework implemented in the Quantum-ESPRESSO package [51] based on plane waves and pseudopotentials. We used the generalized gradient approximation (GGA) parametrized with the Perdew-Wang (PW91) exchange-correlation functional [96] and Vanderbilt ultrasoft pseudopotentials [52]. The plane-wave basis set was chosen with a kinetic energy cutoff of 30 Ry for the wave functions and 180 Ry for the total charge. The Brillouin zone for the band structure calculation was sampled by a $8 \times 1 \times 1$ Monkhorst-Pack k -point grid [143], if considering the x axis as the direction of periodicity for the NWs. The NWs geometry is optimized with the direct energy minimization technique of Broyden-Fletcher-Goldfarb-Shanno [97], based on the calculation of the Hellman-Feynman forces. The optimization is stopped when each Cartesian component of the force acting on each atom is less than 0.026 eV/\AA . All the presented properties are referred to the optimized systems. A vacuum gap of at

least 10 Å separates each NW from its periodic replica in neighbour supercells to avoid spurious interactions. A satisfactory convergence of the calculated properties with respect to the above parameters has been carefully checked. The structural optimization of the tetragonal three-dimensional anatase crystal gave lattice constants $a=3.809$ Å and $c=9.604$ Å, whereas the internal dimensionless parameter is $u=0.208$. All three numbers compare well to the experimental values (at 15 K) 3.782 Å, 9.502 Å and 0.208 respectively [98]. The starting geometry of the TiO₂ NWs is defined with atoms at the ideal crystal positions. The atomic positions were then randomized by 1% to break symmetries and thus ensuring an unconstrained and more physical relaxation. The bands energy alignment of all the NWs is achieved by calculation of a mean electrostatic potential as function of the distance from the NW axis. At a fixed distance, this mean electrostatic potential is the average on the surface of a cylinder coaxial to the NW. The flat value of the averaged electrostatic potential in the vacuum region is defined as the vacuum level and shifted to 0 eV (reference energy). All the single state eigenvalues are accordingly shifted such that the energy of the VBM matches the ionization potential. In Fig. 4.1 we report the application of this procedure to a set of NWs that we have studied in this chapter, where it is possible to see the trend of the averaged potential to a flat value as the distance from the NW axis increases. In Sec. 4.3.2 we will show that this procedure gives reliable results which can be directly connected to the experiments.

4.1.2 NWs definition

In Fig. 1.5 we show that the smallest bare and stoichiometric NW (labeled sw9) studied in this chapter is made up of 27 atoms in the unit cell, with chemical formula (TiO₂)₉. This NW directly follows from the model proposed by C. Liu and S. Yang in an experimental effort to synthesize angstrom-scale titania NWs, which are the thinnest anatase TiO₂ NWs assembled to our knowledge [58]. The sw9 NW elongates in the [001] direction, which is a common growth direction of anatase 1D nanostructures due to the anisotropy of the TiO₂ crystal and to the different reactivity of the (001) surface with functionalizing species in the synthesis process [9, 57]. A first kind of surface coverage is achieved by bonds with single hydrogen atoms (H) of the undercoordinated atoms of the surface. This NW (sw9-H) has chemical

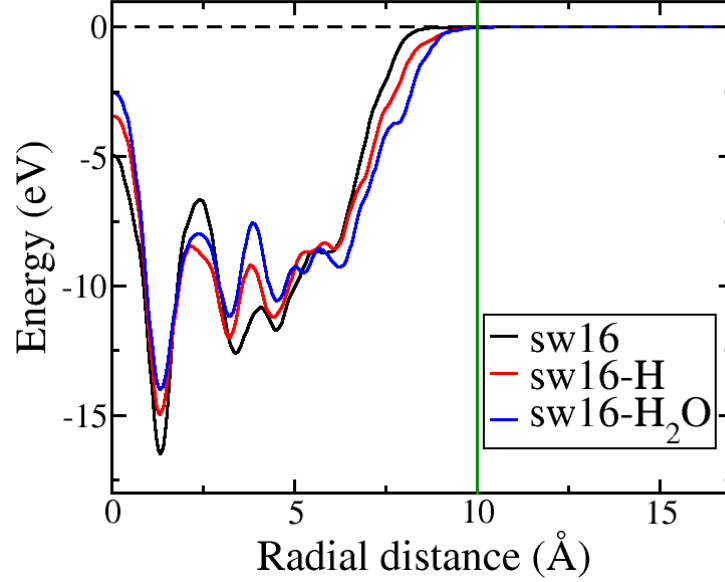


Figure 4.1: Plot of the averaged electrostatic potential on cylinders coaxial with the NW. The green vertical line highlights the distance from the axis where the averaged potential approaches the flat value. The three curves refer to a bare NW (black curve) and its hydrogenated (red) and hydrated (blue) surface counterparts [144].

formula in the unit cell $(\text{TiO}_2)_9\text{H}_{20}$. The hydrogenation coverage is meant to model the NWs in extreme acidic environments or the exposure of naked NWs to a H_2 atmosphere [42, 149]. The second surface coverage is obtained bonding with H atoms the undercoordinated oxygens of sw9 and with OH groups the undercoordinated Ti, thus closing their octahedral coordination. The resulting NW (sw9- H_2O) has chemical formula $(\text{TiO}_2)_9(\text{H}_2\text{O})_{12}$ in the unit cell. This hydration coverage is meant to model a moderate pH environment in which a complete dissociative adsorption of water takes place. The OH groups can also model the same stabilizing role of the functionalizing species employed in the NW production [57].

The second bare and stoichiometric NW (sw25) studied in this chapter is made up of 75 atoms in the unit cell, with chemical formula $(\text{TiO}_2)_{25}$. Its morphology derives by the connection of single NCs, that we studied in the previous chapter, to form a chain in the $[001]$ direction. The lateral surfaces expose the (100) and (010) planes, which occasionally occur in nanostructured TiO_2 [134, 79, 145, 146, 147, 148]. Ti

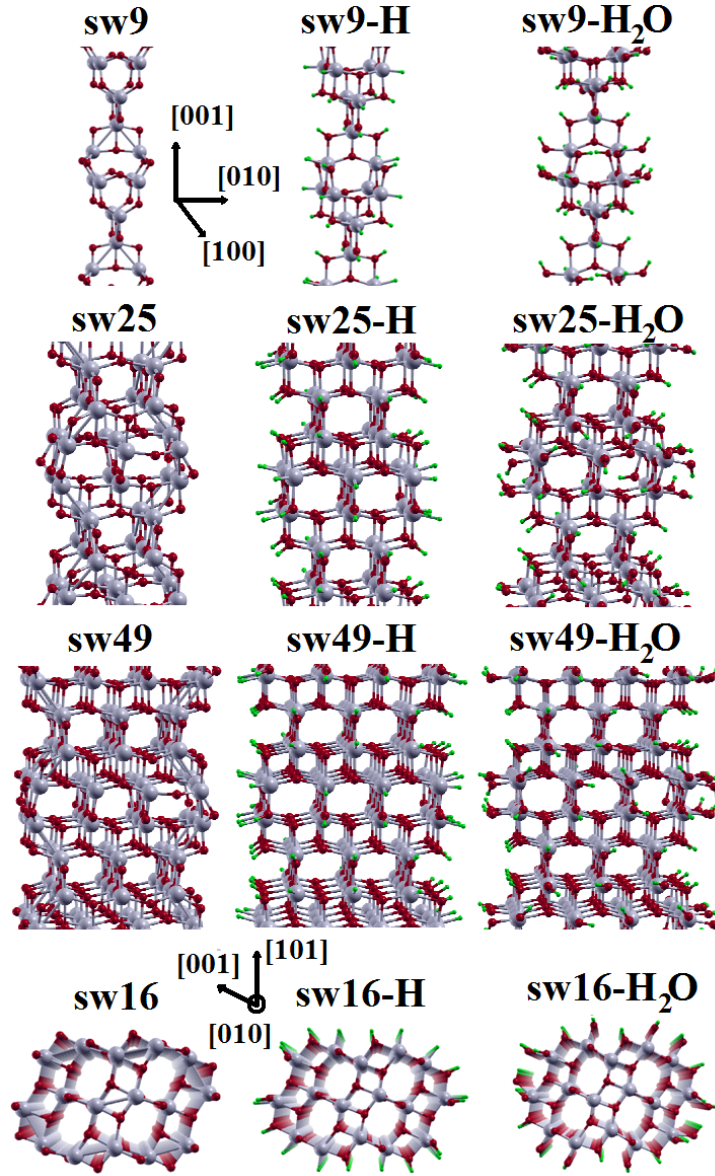


Figure 4.2: Optimized structures of the stoichiometric NWs. Ti atoms are in grey, O atoms in red and H atoms in green. The first type NWs are elongated in the $[001]$ direction whereas the second type NWs (bottom row) are elongated in the $[010]$ direction. Bare NWs are in the left column, hydrogenated NWs in the central column, and hydrated NWs in the right column with their respective label reported on top.

atoms are at least 4-fold coordinated while O atoms are at least 2-fold coordinated. As for sw9, we considered both hydrogenation and hydration. The hydrogenated NW (sw25-H) has chemical formula in the unit cell $(\text{TiO}_2)_{25}\text{H}_{36}$. The hydrated NW (sw25-H₂O) has chemical formula $(\text{TiO}_2)_{25}(\text{H}_2\text{O})_{20}$ in the unit cell.

The third bare and stoichiometric NW (sw49) of this morphological set is made up of 147 atoms in the unit cell, with chemical formula $(\text{TiO}_2)_{49}$. It retains the same axial direction and exposed surfaces as sw25 but with a longer diameter. In this way we can span the range of 1 nm size to give a trend in dimension of the calculated properties. This bare NW is also considered in its covered configurations, the hydrogenated sw49-H and the hydrated sw49-H₂O, with chemical formula $(\text{TiO}_2)_{25}\text{H}_{52}$ and $(\text{TiO}_2)_{25}(\text{H}_2\text{O})_{28}$ respectively. At last, we calculated a naked NW (sw81) with same morphology and a diameter of 1.524 nm (figure not shown).

The fourth bare and stoichiometric NW (sw16) contains 48 atoms in the unit cell, with chemical formula $(\text{TiO}_2)_{16}$. It is periodic in the [010] direction and the lateral surfaces are derived by cutting with (101) and (001) planes. In this case Ti atoms are at least 5-fold coordinated. This second type of NW is used to identify properties related to morphological aspects as the growth direction and the exposed surfaces. The hydrogenated form (sw16-H) has chemical formula $(\text{TiO}_2)_{16}\text{H}_{20}$ while for the hydrated NW (sw16-H₂O) it is $(\text{TiO}_2)_{16}(\text{H}_2\text{O})_{10}$ in the unit cell.

4.2 Results and discussion: structure

The microscopic knowledge of the local structural features of TiO₂ nanostructures is a critical issue for the understanding of the properties that emerge at the nanoscale. The fundamental question to be addressed is the relevance of the profusion of specific geometric and local arrangements on the overall performance and activity of the nanosamples. The theoretical modeling is thus a necessary tool to push the microscopic investigation of TiO₂ NWs on a purely atomistic scale, where the current available experimental techniques may encounter challenging tasks to overcome. In this section we show that the structural properties of the NWs depend on the diameter size, on the morphology, and on the surface termination. These are factors that can deeply influence the behaviour of the nanosamples in real applications and

must be taken into account when designing new TiO₂ nanomaterials.

4.2.1 Section area variations

We have estimated the transversal variations of the area of a NW section by comparing the section area of an optimized NW with that of the NW with the atoms at the bulk positions. The section area of a given NW is computed as $A = \Delta d_x \cdot \Delta d_y$, where Δd_i is the diameter along the i axis. Keeping the crystallographic notation the axes are $\{x = [010], y = [100]\}$ for the first type NWs periodic along the $[001]$ direction and $\{x = [100], y = [001]\}$ for the second type NWs periodic along the $[010]$ direction, while Δd_i is computed as the distance between the outermost Ti atoms along the i direction.

From Tab. 4.1 it can be seen that the section of all the bare NWs is contracted with respect to the ideal bulk value, whereas the surface coverage always leads to the expansion of the section. Thus the presence of adsorbates at the surface can compensate and eventually invert the own trend of TiO₂ NWs to contract inward. This first result must be considered when measuring the lattice parameters variations in real NWs as they always undergo surface interactions either in the synthesis process, either due to functionalizations for specific applications, or in the final working environment. It can also explain the contrasting experimental results on the lattice variations with the size observed for TiO₂ NCs synthesized with different techniques [13].

The bare NWs section is more and more contracted with respect to the ideal (un-relaxed) size as the diameter decreases, which is actually found for TiO₂ nanoparticles larger than 10 nm (Ref. [12]). Hence naked TiO₂ NWs are expected to contract with the size reduction. At variance with this trend, water covered NWs undergo an increasing expansion with decreasing size. This second result is in agreement with the volume trend of the TiO₂ nanoparticles below the 10 nm size desumed from experiments [12]. Thus we can explain the overall trend upon size reduction in terms of competing phenomena: on one hand anatase TiO₂ NWs have an own tendency to contract but, on the other hand, the presence of surface adsorbates induce the opposite effect. Thus, when the size is shorter than 10 nm the surface dislocations prevail and a clear contraction is detected. At the end, the second type

Table 4.1: Diameters ($\Delta d_x, \Delta d_y$), section area ($A = \Delta d_x \cdot \Delta d_y$) and section area variations ($\Delta A = (A - A_0)/A_0$, A_0 being the section area of the NW with the atoms in the ideal bulk positions) of the NWs. Δd_x and Δd_y are calculated as the distance along the respective axes (x, y) between the two outermost Ti atoms (keeping the crystallographic notation $x = [100], y = [010]$ for the first type NWs and $x = [100], y = [001]$ for the second type NWs).

System	Δd_x (Å)	Δd_y (Å)	A (Å ²)	ΔA (%)
ideal	3.809	3.809	14.51	-
sw9	3.167	3.566	11.29	-22.2
sw9-H	3.859	3.752	14.48	-0.3
sw9-H ₂ O	4.016	4.170	16.75	+15.4
ideal	7.618	7.618	58.03	-
sw25	7.180	7.181	51.56	-11.1
sw25-H	7.788	7.819	60.89	+4.9
sw25-H ₂ O	7.884	7.712	60.85	+4.8
ideal	9.522	12.005	114.31	-
sw16	9.266	11.717	108.57	-5.0
sw16-H	9.711	12.340	119.83	+4.8
sw16-H ₂ O	9.789	12.084	118.29	+3.5
ideal	11.427	11.427	130.58	-
sw49	11.053	11.012	121.71	-6.8
sw49-H	11.618	11.620	135.00	+3.4
sw49-H ₂ O	11.685	11.681	136.49	+4.5
ideal	15.236	15.236	232.14	-
sw81	14.923	14.901	222.37	-4.2

NWs grown along the $[010]$ direction (sw16 series in Tab. 4.1) show variations in the trend of the section area with respect to the first type NW of comparable size. Both the bare sw16 and the hydrated sw16-H₂O have smaller variations than the first type NWs. Hence by changing the exposed surfaces and the growth direction it is possible to tune the NW crystallinity against variations of the size and of the

surface configuration.

4.2.2 Variations of the atomic distances

We analyzed the bond lengths and the distances between atoms in the NWs to have a picture of the deviation from an ideal perfect crystallinity, which is unavoidable in the real nanosamples. We show here the result of this study through plots of the distribution of the distance between atomic pairs.

All the NWs show distortions (with respect to the ideal, bulk positions) in the geometry of the bonds as well as of the long range distances between the atoms. Hence a change of the coordination numbers of the bulk atomic shells is revealed by the distribution of distances around the bulk ideal values, as shown in Fig. 4.3 (a) for the case of the Ti-O distances in the sw49 NW series. The surface coverage is always found to preserve a better structural order with respect to the bare NWs. This result can be seen by the smaller dispersion of the distances around the bulk values which results in the long range order of the covered NWs. Thus the first result clearly points out that the surface termination with proper adsorbates is determinant for synthesizing well ordered and crystalline NWs with diameters in the nanometer range. The largest atomic displacements are found for the NWs terminal atoms (figure not shown), upon covering the surface. In fact, the adsorbates induce an outward shift of the NW atoms which are instead contracted in the bare NWs. Furthermore, the inner atoms of the covered NWs faithfully reproduce the bulk-like geometry. Hence, we agree with the very recent suggestion that for anatase nanocrystals a core-shell picture of the structural organization can be inferred [12]: internal atoms preserve the (ideal) anatase crystal arrangement whereas a surface shell of atoms is more or less distorted according to the local surface environment and to the availability of adsorbates.

The overall crystallinity of the NWs also depends on the diameter size. On increasing the size in the first type NWs the octahedral coordination of the titanium atoms, the geometry of the bonds, and the atomic distances are closer and closer to the corresponding bulk values. In Fig. 4.3 (b) we summarize this trend focusing on the short range order of the Ti-O bonds of the bare NWs. As shown by the green arrows, the main peaks of the distance distribution shift to the bulk bond lengths as

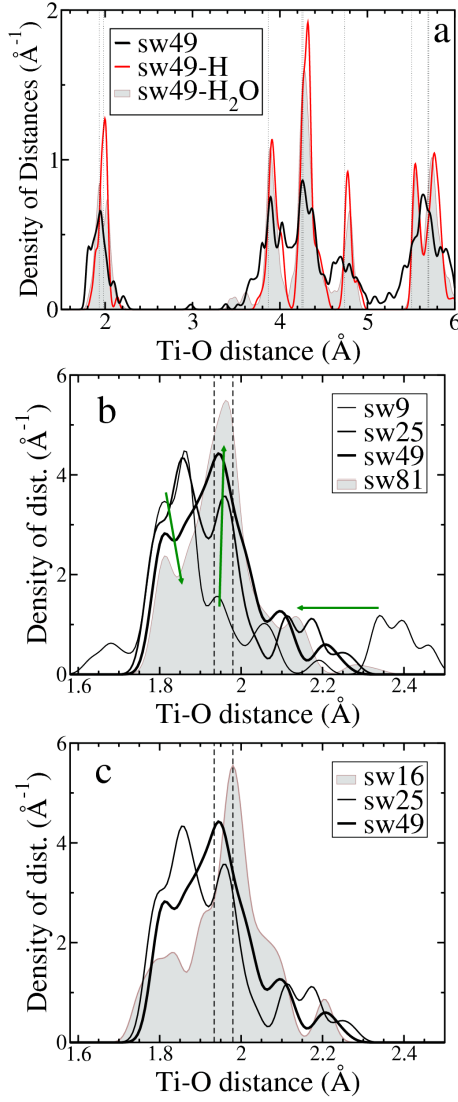


Figure 4.3: Distribution of the atomic distances density for (a) the sw49 series of NWs, (b) the first type bare NWs, and (c) the bare second type NW sw16 and the bare first type NWs (sw25 and sw49) of comparable size. Vertical dashed lines correspond to the bulk distances, while the green arrows in (b) highlight the effect of the size increase on the relevant peaks. A fictitious Gaussian broadening ($\sigma = 0.03 \text{ \AA}$) is attributed to each distance to give a clearer picture.

the size of the NW increases. In fact, the peaks outside the range of the bulk values (vertical dashed lines) lose their intensity or shift to the bulk values whereas the peak at the bulk values increases its intensity. Hence the long range effects of the local surface disorder can be diminished by increasing the size, yet they cannot be eliminated.

As a last result, we mention that the morphology of the NWs also contributes to change the effects of the size on the structural distortions. In fact, we found that the second type NWs grown along the [010] direction have a better crystalline order than the first type NW grown along the [001] direction of comparable size, namely the sw25 and sw49 series. The result also holds for the surface covered NWs but to give an easy picture of this dependence we show in Fig. 4.3 (c) the Ti-O distribution of distances in the bond lengths range of the bare NWs. The second type NW sw16 shows a structural order that is close to the largest studied NW sw81, with a diameter of 15 Å. We conclude that the choice of the exposed crystallographic surfaces and of the growing direction can be factors to be taken under consideration when the crystallinity of the nanosamples is a crucial parameter for the applications of these TiO₂ NWs.

4.3 Results and discussion: electronic properties

4.3.1 Effects of the size reduction

Many aspects concerning the size reduction in TiO₂ nanostructures are still object of debate. Unraveling such aspects is crucial, to employ such materials in the future generation of optical and electronic devices. First of all, we mention the increase of the band gap in the quantum confinement regime due to the shrinking of the material below the exciton radius (r_{ex}). Experiments on TiO₂ nanostructures do not always agree in detecting the band gap blue shift upon size reduction [22]. This also applies to the 1D NWs, as they can be grown as agglomerates of NCs.

To detect the blue shift of the band gap it is sufficient that the material size in one direction is of the order of r_{ex} . The size of the TiO₂ r_{ex} is not unambiguously determined and it is reported in the range 0.35 – 1.9 nm [22, 75]. Our model systems fit in this range as their size goes from 3.81 Å for the thinnest sw9 NW to 15.24 Å

Table 4.2: Valence band maximum energies (VBM) scaled with respect to the vacuum and to the SHE reference. ΔE_g is the band gap difference with respect to the bulk value.

System	VBM (eV) ¹		ΔE_g (eV)
	vs vacuum	vs SHE	
bulk ²	-7.13	+2.69	-
thin film ³	-6.94	+2.50	-
sw9	-7.25	+2.81	0.67
sw25	-7.21	+2.77	0.59
sw49	-7.26	+2.82	0.34
sw81	-7.18	+2.74	0.18
sw16	-7.01	+2.57	0.06
sw9-H ₂ O	-6.77	+2.33	1.22
sw25-H ₂ O	-6.94	+2.50	0.65
sw49-H ₂ O	-6.72	+2.28	0.45
sw16-H ₂ O	-6.54	+2.10	0.53
sw9-H	-7.56	+3.12	metal
sw25-H	-7.55	+3.11	metal
sw49-H	-7.37	+2.93	metal
sw16-H	-7.49	+3.05	-0.61

for the largest sw81 NW. The anatase crystal is an indirect-gap semiconductor with the first transition ($\sim X \rightarrow \Gamma$) at 3.2 eV. Our calculation on the bulk crystal gives a band gap of 2.08 eV which well compares with other theoretical calculations based on the DFT [150, 151, 152], but it is clearly an underestimation of the real band gap (this is an usual shortcoming of the DFT). We expect that this underestimation does not affect our results since it should be independent of the dimensionality of the system. As reported in Tab. 4.2, the bare NWs of the first type, elongated in the [001] direction, show a band gap blue shift with respect to the bulk value which goes from 0.18 eV for the largest sw81 to 0.67 eV for the thinnest sw9.

This is a clear indication that the size reduction affects the band gap blue shift. As expected on a general ground, the amount of blue shift increases with the size reduction and the fact that the largest sw81 presents a 0.18 eV blue shift leads us to conclude that the TiO_2 r_{ex} is at least of 1.5 nm. Interestingly, the second type NW sw16 shows a small band gap variation with respect to the bulk crystal ($\Delta E_g = 0.06$ eV) even if its diameter is comprised between the sw25 and the sw49 ones. The degree of structural distortion is not so different between the two types of bare NWs to account for such a deviation, thus we ascribe the substantially unchanged band gap of sw16 to a morphological origin. The second type NWs expose the (101) and (001) surfaces which are typically more stable in the most common conditions. TiO_2 nanostructures with these surfaces as the major fraction of the surface facets can retain bulk-like properties hence hindering the effect of the size reduction by making difficult the detection of the band gap blue shift down to the smallest samples. This result unravels a possible explanation of the disagreement of the blue shift measurements, in that a dependence of the quantum confinement effect on the morphology of the nanostructure comes out.

The effect of the structural distortion on the band gap becomes visible by considering the more ordered hydrated NWs. As reported in Tab. 4.2, all hydrated NWs show a higher blue shift with respect to their bare configuration. Moreover, the band-gap shift of the (second type) sw16 NW falls between the sw25 and sw49 ones, as it should be for an ideal trend of the blue shift with the size. As discussed in Sec. 4.2, hydrated NWs have the highest crystallinity which means that as the size of TiO_2 nanostructures decreases the effects of the local bonds geometry, surface reconstruction, and structural order become more and more relevant in determining the final electronic properties. This suggests that particular attention must be paid in synthesizing well ordered TiO_2 NWs to detect quantum confinement phenomena.

The electronic properties of hydrogenated NWs deviate from the other surface configurations because in-gap states appear. Both types of NWs show occupied bands above the VBM energy which correspond to surface defect levels localized on the Ti-H bonds. The second type NW sw16-H, elongated in the [010] direction, preserves its semiconductive band gap but the first type hydrogenated NWs have occupied bands at the bottom of the CBM energy, with the band gap closing to less than 60 meV. Hence a metallic behaviour is expected for this morphology of

TiO₂ NW which once again stresses the importance of the geometric design of this nanostructured material. Interestingly, experiments on TiO₂ NCs reveal the possibility of H lattice diffusion to produce free conduction band electrons from infrared excitation [29]. Moreover, conductance enhancement of several order of magnitudes has been detected in TiO₂ nanotubes upon exposure to hydrogen gas [40]. We will debate in detail this topic in Sec. 4.3.4.

The second issue discussed in this section is related with the efficiency of TiO₂ NWs to support photocatalytic reactions and the charge transport to external circuits (for photosensing and solar cells). Both mechanisms are linked to the nature of the charge density distribution of the states involved in the transfer of charges. In fact the probability of the charge transfer increases with the overlap between the donor/acceptor wave functions of the NW and the reactant. To support the transport of photoelectrons throughout the external circuit it is also necessary that conduction band channels flow inside the NW to lengthen the lifetime of charges by avoiding recombination centers, i.e. structural distortions, defects, and charge traps which are mainly located at the surface.

From the analysis of the projection of the density of states on the atomic orbitals we found that both highest valence bands and lowest conduction bands involve atoms located at the surface, particularly for the bare NWs (see Fig. 4.4). This means that the size reduction effectively turns in favour of higher photocatalytic performances. Interestingly hydration of the surface is found to produce states with a spatial distribution of the density which is higher inside the NWs structure than that belonging to the states in same energy region of the bare NWs, see as example the effect of H₂O on the LUMO state of the sw25 NW in Fig. 4.4.

This effect sums to a better crystallinity of the hydrated NWs thus entailing the possibility to design surface configurations that optimize the availability of internal channels for the transport of electrons. To this purpose it is noteworthy that the water induced inward shift of the charge density is not appreciable only for the conduction bands of the second type NW sw16, hence it is important to select appropriate adsorbates according to the morphology of the NWs. The highest valence bands states, with O 2p orbital character, are delocalized on the surface thus being readily available for the charge transfer with adsorbates. On the other hand, the lowest conduction bands states, with Ti 3d orbital character, are delocalized inside

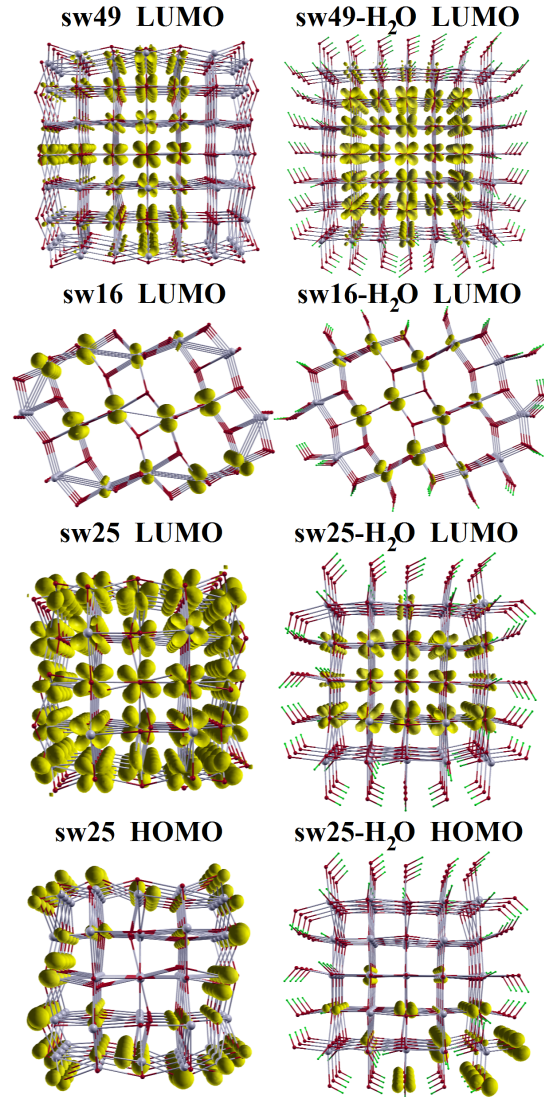


Figure 4.4: Charge density contour plots (10% of the maximum value) for some relevant electronic states lying in the gap region. The charge densities are localized on the surface for the bare NWs. On the other hand, the states in the gap region of surface covered NWs show charge densities with higher intensities inside the NWs than isoenergetic states of the bare NWs. This effect is not appreciable only for the lowest energy conduction bands of the second type NW sw16.

the NWs with tails on the surface atoms. This ensures both the possibilities for photoelectrons to be exchanged with the adsorbates and move along the NW axis. In conclusion the NWs are found to profit from the size confinement since the charge density of their states in the band gap region involves atoms at the surface, where the most of photocatalytic reactions takes place. Furthermore the interaction with water induces variations in the wire field that end up with the modulation of the spatial distribution of the NWs wave functions, thus proving the possibility to tune the electronic properties by specific surface configuration. The adsorbates can be functional to preserve a better crystallinity of the thinnest NWs on one hand and to confer peculiar properties to the electronic channels on the other.

4.3.2 Bands line-up

In this section we discuss the distribution of electronic levels in the ‘bulk’ band-gap region since they are important in determining the relationship between the redox potentials of the nanostructured TiO_2 and the reactive couple adsorbed at the surface. This relationship establishes the direction of a reaction when the two reactants are placed together. A striking example is the evolution of H_2 and O_2 in the water splitting process for which nanostructured TiO_2 is willing to be used. By illuminating TiO_2 nanostructures the photogenerated holes (h^+) can oxidize water molecules to produce hydroxyl radicals and protons, while photogenerated electrons (e^-) flow to the photocathod and produce molecular hydrogen by reducing the protons. The former oxidation process takes place if the TiO_2 VBM energy is more positive than the water redox potential on an electrochemical scale (i.e., vs SHE, the standard hydrogen electrode). The latter reduction process is allowed if the TiO_2 CBM energy is more negative than the hydrogen redox potential. We calculated the line-up of the bands energies of our model systems with respect to the vacuum energy and hence to an electrochemical scale by means of cylindrical averages of the electrostatic potential, as defined in Sec. 4.1.1. Moreover a rigid shift of the conduction bands has been applied to correct the DFT underestimation of the band gap of the semiconductive NWs, as detailed later. Thus we analyzed for the case of TiO_2 NWs the effect of size reduction, the determination of the h^+ acceptor site, and the capability of hydrogen sensing.

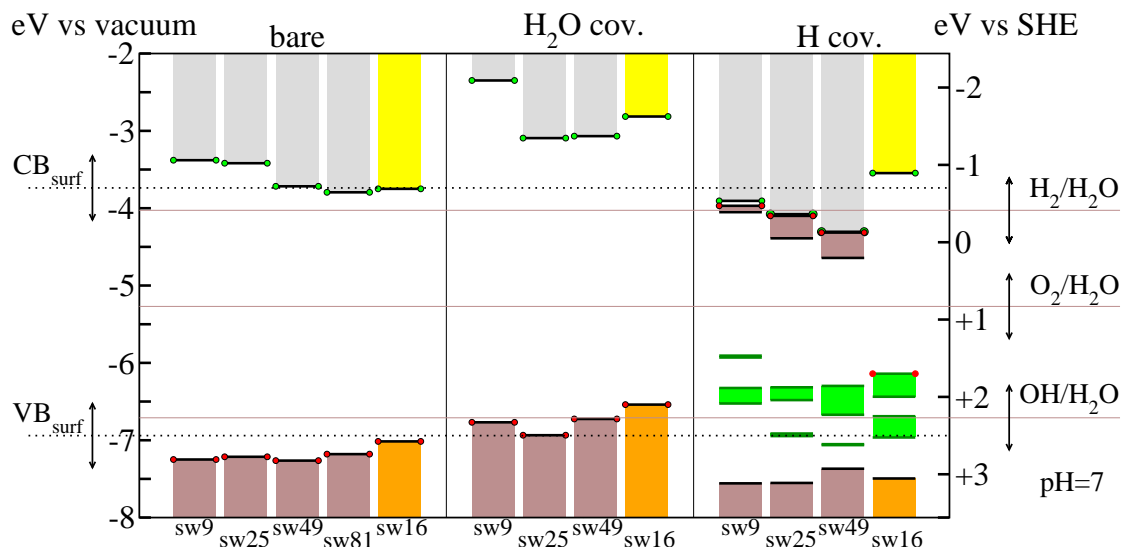


Figure 4.5: Band line-up of the NWs in the gap region. Brown bars refer to occupied states (orange for the second type NW elongated in the [010] direction), gray bars to empty states (yellow bars for the second type NW). Green bars refer to hydrogen induced in-gap states. Red circles refer to the HOMO energy level whereas green circles to the LUMO energy level. The dotted horizontal line is the experimental HOMO energy level from Ref. [153]. Continuous horizontal lines refer to the energy value of relevant redox potential couples at pH=7 taken from Ref. [27]. Their respective vertical lines span the energy range of variation with the pH. On the right the energy scale is relative to the standard hydrogen electrode (SHE). All the CBM energies of semiconductive NWs are shifted of +1.12 eV to account for the DFT underestimation of the band gap of semiconductive materials.

Fig. 4.5 reports the VBMs, the CBMs, and in-gap states energies of the NWs. To give a direct comparison of these energies with experimental data we scaled the graph with respect to the vacuum reference (on the left) and to the standard hydrogen electrode (SHE, on the right), and we also reported the highest occupied molecular orbital (HOMO) energy obtained with a UPS measurement on a nanocrystalline TiO_2 thin film[153] (labeled as VB_{surf}). Horizontal lines refer to the redox potentials at pH 7 of the species involved in the water splitting process[27]. The respective vertical arrows set the energy range in which these energies change by changing the pH of the solution (towards more positive values with decreasing pH and vice versa

for increasing pH).

We found the VBM of all the bare NWs to fall in the range $-7.26 \div -7.01$ eV (see Tab. 4.2). By considering that our bare systems are isolated NWs, we can compare this energy range with the UPS measure of -6.94 eV obtained in vacuum by Snook *et. al.* on nanocrystalline TiO_2 thin films [153]. UV-vis absorption spectrum gives a VBM value of -7.4 eV for TiO_2 nanorods surface capped with conjugate polymers [154], which however shift the VBM due to charge transfer at the interface. Comparison is also possible with cyclic voltammetric measurements which gave a VBM value of -6.9 eV for surface capped TiO_2 nanocrystals [155], whereas the anatase single crystal value lies around -7.13 eV at pH 7 [156]. In this case the VBM is extrapolated by measuring the flat band potential, which matches the apparent Fermi energy of the sample.

All these values unveil that the NWs do not undergo a sensible variation of the VBM energy, also for the case of the thinnest sw9 NW. Thus an increase of the oxidant capability of TiO_2 h^+ cannot be achieved merely by size reduction of NWs. In fact, the VBM energy difference between the thinnest sw9 and the largest sw81 NW is 0.07 eV. Room for tuning the VBM energy can instead be connected to the morphology of the NWs, since first type NWs, elongated in the [001] direction, have a VBM energy at least 0.17 eV lower than the second type NW, grown along the [010] direction. Anyway all the VBM energies are more positive (at least $+2.57$ eV) than the redox potential of the $\text{O}_2/\text{H}_2\text{O}$ couple ($+0.83$ eV, pH=7), which means that all NWs are able to support oxidation of H_2O by h^+ donation.

To produce the reaction of the water splitting it is also necessary that the H_2 reduction potential is less negative than the CBM energy of the NWs. Bulk rutile has a VBM energy essentially coincident with the reversible hydrogen potential, whereas for bulk anatase is more negative by 0.20 eV [83]. Therefore anatase is the only TiO_2 crystal phase thermodynamically able to induce the water photoelectrolysis [156]. As discussed in the previous section, DFT typically underestimates the band gap of semiconductors so that a direct comparison of the CBM energies in Fig. 4.5 with experiments is not possible without applying a rigid shift (1.12 eV) to the empty bands energies. This procedure would match the calculated bulk band gap (2.08 eV) and the experimental one (3.2 eV) and it has been already applied to the TiO_2 semiconductor [151, 157, 158]. The shift unveils that all NWs CBM energies lie

above -0.65 eV vs SHE, which is 0.24 eV more negative than the H^+/H_2 reduction potential (-0.413 eV [27]). All the bare NWs are thus found to be able to produce a complete water splitting reaction by oxidation of water at the surface and reduction of protons at the cell cathode.

The morphology of the NWs, also in this case, can play a role in determining the ability of the nanostructure to efficiently produce the reaction, since the second type NW (sw16) has a CBM energy close to the larger first type NWs (sw49 and sw81) and to the experimental CBM of nanocrystalline thin films [153], but as stated before the sw16 VBM energy is about 0.2 eV higher than those of all the first type NWs. Therefore we expect an overall lower yield of the second type NW with respect to the first type, for NWs of the same size.

The last result deals with the effect of the size on the first type NWs, elongated in the $[001]$ direction. The respective CBM energy is shifted to higher negative redox potential values as the size reduces, such that the thinnest sw9 has a CBM energy 0.41 eV more negative than that of sw81. This directly leads to infer that as the diameter of the $[001]$ NWs decreases the ability to reduce protons to produce molecular hydrogen increases. Hence the anatase $[001]$ NWs show an increasing efficiency in the water splitting as a consequence of the size confinement.

4.3.3 Pathways of reactions at the surface of the NWs

In this section we discuss an unsolved problem in the photocatalytic activity of TiO_2 , i.e. the nature of the h^+ trap responsible for the oxidation of reactants [83]. There is consensus on the fact that recombination of photocharges is delayed by trapping in localized states, from which photocharges are transferred to dissolved reactants [83, 84]. However the hole trap site is not yet unambiguously determined, since it has been assigned to terminal hydroxyl radicals [84, 85], lattice oxygens [82], subsurface oxygens [86], surface oxygen radicals [87, 88]. Here we consider our water coverage of the NWs as a model configuration for the hydroxyl termination, where the hydrogen covered oxygen of the bare NW (Ti-OH-Ti) represents an acidic site while the hydroxyl group which covers undercoordinated Ti represents a basic site (Ti-O-Ti-OH) [87]. This surface configuration is based on the assumption that TiO_2 nanostructures are more hydroxylated than macroscopic surfaces, given the

stabilizing role of the hydroxyl group [28, 74]. Therefore it simulates a generic configuration of a stable surface covered NW.

As shown in Fig. 4.5, the VBM and CBM energies of the H₂O covered NWs are upward shifted in comparison to the bare case. It is a consequence of the Nernstian dependence of the band edge energies from the pH, which is valid for most oxide semiconductor/aqueous solution interfaces [159] and found to persist over a wide range of pH for nanocrystalline TiO₂ [160]. It is essentially ascribed to a surface acid-base equilibrium where charge is transferred creating an accumulation layer in the solid, the bands undergo an upward bending if excess electrons are accommodated on the surface whereas downward bending is consequence of positive excess charge [83, 159]. Our model NWs are subject to the same shift, which is predominantly due to the basic behaviour of the terminal hydroxyl groups (Ti-OH), where excess electronic charge is transferred from bound Ti atoms. This leads to consider our surface configuration as a reliable model for NWs in basic solution and shows that the general model employed for the TiO₂ semiconductor holds through the nanometer scale. Thus a first result is the effective ability of the hydroxyl groups adsorbed on the surface of NWs to attract excess electronic charge. Hence it is possible that conduction band electrons are scavenged by the presence of such terminal groups as experimentally reported for TiO₂ nanocrystals [29].

The VBM energies of the hydrated NWs lie around the water oxidation potential to hydroxyls (2.27 eV vs SHE, pH=7) [27] as reported in Tab. 4.2. This means that the overall effect of terminal Ti-OH groups is to lower the oxidizing potential of the NWs, if they constitute stable radicals in acidic environments. On the other hand, the upward bending of the CBM energies increases the reducing potential of photoelectrons, which are able to form superoxide O₂⁻ and hydrogen peroxide H₂O₂. Two questions which are debated in literature on the activity of TiO₂ surfaces and nanocrystalline assemblies can now be discussed in the case of TiO₂ NWs[88]: (i) can the photogenerated TiO₂ VB hole oxidize the terminal OH radical? (ii) which condition allows the production of free OH species participating in the primary oxidation of organic compounds? The first question can be addressed by studying the nature of the top VB states. The analysis of the DOS and of the charge distribution of states reveals that the highest occupied states are indeed O 2p as expected for TiO₂, but their spatial distribution involves both oxygens from the hydroxyl groups

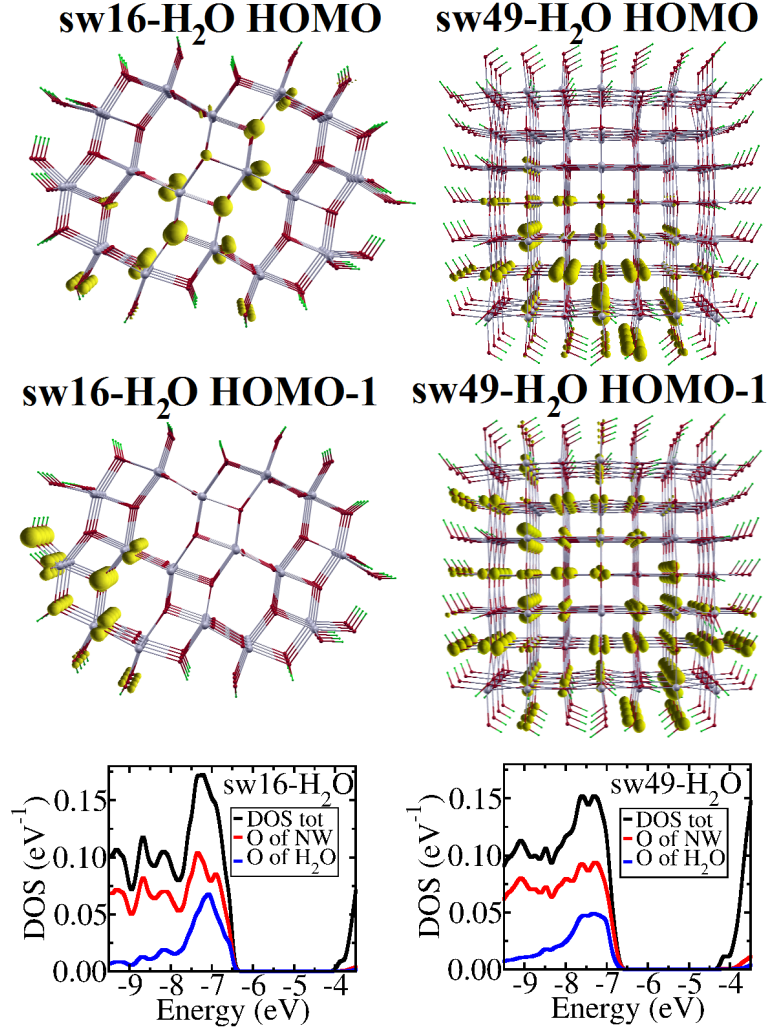


Figure 4.6: Charge density contour plots (10% of the maximum value) of the HOMO and HOMO-1 states of the hydrated sw16 NW on the left and the hydrated sw49 NW on the right. In the bottom panels the respective total DOS (black line) is projected on the oxygen orbitals belonging to the NW (red line) and to the water molecules (blue line).

and oxygens of the NWs (see Fig. 4.6). This is due to the fact that the energy range of the OH 2p states overlaps with that of the O 2p states of the NWs. Hence a clear distinction of the final hole trap between hydroxyl termination and sub-surface oxygen is not possible for the thinnest imaginable anatase NWs. Some remarks in

favour of the sub-surface oxygens as final hole traps can however be asserted: (i) the DOS maximum peak of the OH 2p states is at least 0.30 eV under the VBM for all the NWs, which means that these states cannot be considered as deep hole traps; (ii) the ratio between TiO₂ O 2p states and OH O 2p states is a function of the degree of surface hydroxylation and of the semiconductor size. Therefore as the size decreases the ratio between surface hydroxyls and sub-surface oxygens can increase leading to a higher number of available OH traps isoenergetic with TiO₂ oxygen traps. Our hydrated NWs are completely hydroxylated and thus model an extreme configuration where hydroxyls have the highest weight. These observations can explain the reason why holes are found to be trapped at surface or subsurface oxygens in TiO₂ colloids and films [86, 88] whereas they are found to be trapped at surface oxygen radicals or terminal hydroxyls in TiO₂ nanoparticles [87, 84, 85]. The second question dealing with the availability of free OH species can be addressed following the picture given by P. Salvador [88]. If the surface of TiO₂ NWs is highly hydroxylated in a wide range of pH the ability to oxidize water can decrease but the upward shift of the CBM energies increases the reduction of dissolved oxygen to superoxide and hydrogen peroxide which ultimately react to produce free OH species. We consider this dynamics to be more feasible for hydroxylated NWs exposed to gaseous environment, due to the limitations that our model systems have to simulate a liquid environment.

4.3.4 Hydrogen sensing ability of the NWs

This last section deals with the possibility to employ TiO₂ NWs as hydrogen sensors. Experiments reveal that TiO₂ nanotubes [40, 41] and mesowires [42] show an increase of the conductance upon exposure to hydrogen gas, which can be of some orders of magnitude [43] and can lead to the highest variation of the electrical properties of a material, to any gas, ever shown [44]. The main mechanism is ascribed to the chemisorption of the dissociated hydrogen molecules at the surface due to the high electrical variation, velocity, and reversibility of the sensing process [45]. Measurements in acid medium show that the resistivity is so low that cannot be reliably measured and a negative bias potential is not needed [41]. Our hydrogenated model systems can fit an analogous surface configuration as the one proposed, with

dissociated hydrogen molecules covering the surface atoms of the NWs.

As shown in Fig. 4.5, all the H covered NWs present in-gap states (green bars) above the VBM energy of the TiO_2 O 2p states. The space charge distribution of these states is surface localized on the titanium bonded hydrogen atoms. The VBM energies are downward shifted with respect to the bare case (in the range $-7.56 \div -7.37$ eV vs vacuum), as expected in acidic conditions where an excess partial positive charge accommodates at the surface (see Tab. 4.2). The most interesting result concerns the bottom of the conduction bands. The first type NWs elongated in the [001] direction have occupied states close in energy to the empty states, showing a gap in the range $10 - 60$ meV. The spatial charge distribution of these states is not localized to single atoms but is conductive like with an exclusive Ti 3d atomic character which is typical of the TiO_2 conduction bands (see Fig. 4.7). Thus it is possible to conclude that TiO_2 NWs can show an increase of the conductance due to the injection of electrons in the conduction bands following hydrogen adsorption at the surface. From the nature of these occupied states below the CBM, i.e. the Ti 3d atomic character, the delocalization of the charge density, and the dispersion of the bands, it is possible to infer that these occupied bands are indistinguishable from the conduction bands of the TiO_2 bare NWs. At the end, the adsorption of hydrogen leads to the formation of a space charge layer which induces the band bending of the energy levels of the NW. The depth of this bending is typically of the order of few nanometers but longer than the diameter of our NWs. Hence the potential shift induced by the space charge layer extends throughout the NW in such a way to equilibrate the NW Fermi energy with the H^+ surface state energy. From an electrochemical viewpoint the $\text{H}^+(\text{aq})/\text{H}_2(\text{g})$ energy is in the range $-0.413 \div 0$ eV vs SHE according to the degree of acidity of the pH, and in fact the occupied states energies lie in the range $-0.47 \div 0.20$ eV vs SHE.

The second interesting result is related to the dependence of the presence of occupied states in the CBM energy region from the surface morphology. The second type NW elongated in the [010] direction does not show such states, but only the decrease of the band gap due to the in-gap states above the VBM. Hence we do not expect the same degree of sensitivity to hydrogen gas for this type of NW, although it has barely the same size of the larger first type NWs. This result highlights the importance of the structural features of low dimensional materials in determining

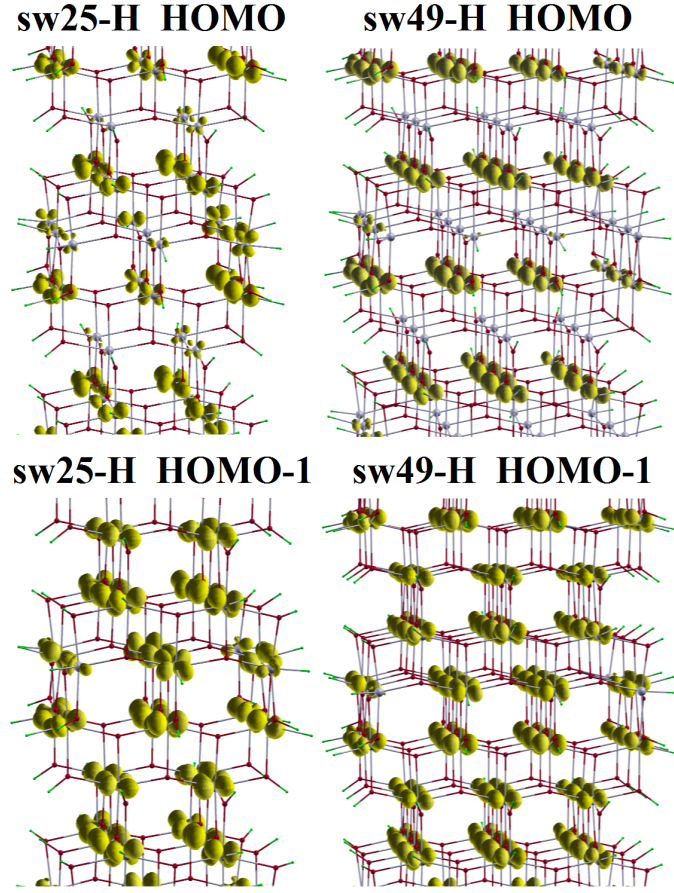


Figure 4.7: Charge density contour plots (10% of the maximum value) of the HOMO and HOMO-1 states of the hydrogenated sw25 NW on the left and the hydrogenated sw49 NW on the right. The charge densities are not spatially localized but spread throughout the NWs.

their overall properties and applicability. At the nanoscale the presence of specific sites plays a fundamental role since the relative amount of each type of active site can be increased by tuning the morphology of the nanostructure.

4.4 Relative stability analysis

The knowledge of the expected stable configurations can be of particular relevance for the choice of the NWs to design and to synthesize. In this last section we discuss

the relative energetic stability of the studied NWs. We calculated the formation energy of a NW as defined by the equation $E_f = E_{tot} - M_x \cdot \mu_x - N \cdot \mu_{\text{TiO}_2}$, where E_{tot} is the total energy of the NW, M_x is the number of covering molecules having chemical potential μ_x ($x=\text{H}_2$; H_2O), N is the number of TiO_2 units (with chemical potential μ_{TiO_2}). The chemical potentials are chosen as the total energy of the correspondent isolated molecules. The energy required to cover the surface with a given adsorbate is given by the equation $E_c = E_{tot} - M_x \cdot \mu_x - E_{tot}^{bare}$, where E_{tot} is the total energy of the covered NW, E_{tot}^{bare} is the total energy of the correspondent bare NW and M is the total number of covering molecules.

As depicted in Fig. 4.8 (a) the formation energy per TiO_2 unit (E_f/N_{TiO_2}) of all the NWs is negative which means that their molecular constituents gain stability upon NW formation. Furthermore, the stability of the NWs increases on increasing the size. This trend is more appreciable for the bare and hydrogenated NWs whose formation energy is thus found to be favoured by the size growth. The hydrated NWs are the most stable systems with formation energies which are close to the bulk value (the maximum energy difference is less than 0.14 eV). Hence the surface configuration reveals its importance in determining the feasibility of a NW also in terms of energetic stability. In fact, given a bare NW, the hydration coverage leads always to the most stable system whereas hydrogenation leads to the least stable system. Fig. 4.8 (b), reporting the coverage energy defined above per adsorbing molecule (E_{cov}/M), shows that the dissociative adsorption of hydrogen molecules is unfavoured for all the NWs. This configuration is thus highly reactive and can fit for applications in hydrogen rich gaseous environments. On the other hand, the dissociation of the water molecule at the surface of TiO_2 NWs is a stabilizing process (negative coverage energies in Fig. 4.8 (b)) since it is able to fill oxygen vacancies, to close the octahedral coordination of terminal titanium atoms, and to preserve a high cristallinity through the smallest TiO_2 NWs that can be synthesized. The stabilization of the bare NWs upon dissociative adsorption of water is more pronounced for the thinnest NWs.

Our result confirms the possibility to find a consistent amount of terminal hydroxyl groups on the surface of TiO_2 NWs as experimentally reported [79, 142]. We can predict that the stabilizing role of the water coverage experimentally found for TiO_2 NCs [74] also stands in the case of 1D NWs. At the end we found that the

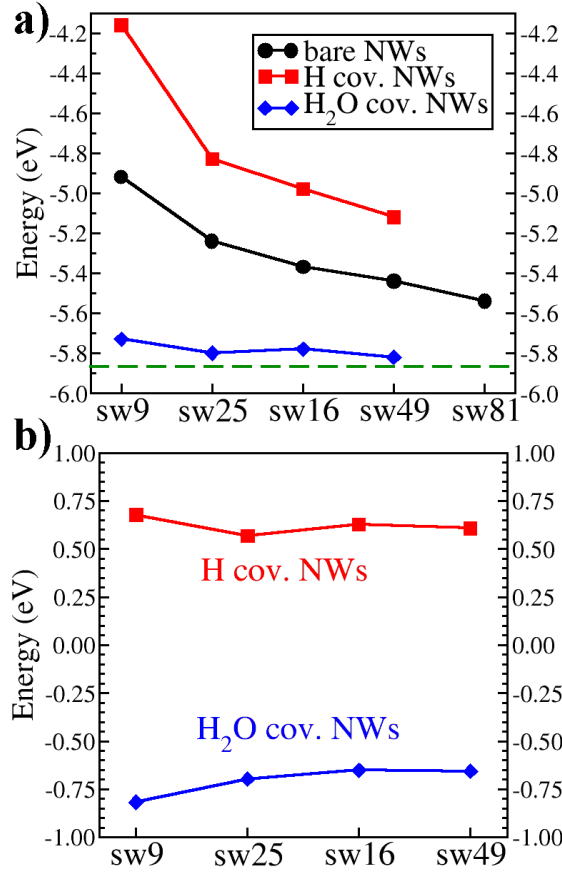


Figure 4.8: a) Plot of the formation energy per molecule of the NWs as function of the diameter size. The black curve refers to bare NWs, the red curve to hydrogenated NWs and the blue one to hydrated NWs. The green dotted line is the formation energy x TiO₂ unit of the bulk anatase. b) Plot of the adsorption energy per adsorbate molecule as function of the diameter size. The red curve refers to the H₂ adsorption energy and the blue curve to the water adsorption energy.

dissociative adsorption of water forms strong bonds at the surface thus extending the experimental results obtained for TiO₂ NCs [28, 74] to the one-dimensional case.

4.5 Conclusions

In this chapter we presented a detailed investigation of the structural and electronic properties of 1D anatase NWs through first-principles calculations. We showed that these properties depend on the diameter size, on the surface coverage, and on the morphology (namely, growing direction and lateral surfaces) of the NWs. These informations can be useful to outline a theoretical background of knowledge, readily available for the experimental research on new TiO_2 nanomaterials and devices. We also proposed an interpretation of some currently debated experimental findings on TiO_2 nanostructures. The main results of this study are summarized in the following.

1. The bare NWs have an inward contraction which decreases their size whereas the surface coverage induces an outward expansion. Hence the final configuration is the result of two competing phenomena. On one hand, the own trend of TiO_2 anatase to exhibit volume reduction on decreasing the diameter size. On the other hand the presence of specific adsorbates can compensate or even reverse this trend leading to expansion, which is typical of nanoparticles shorter than 10 nm (Ref. [12]). In fact, the surface atoms are found to undergo the largest displacements depending on the kind of covering species. Thus as the size increases the effects of the surface deformations lose their weight in determining the overall configuration.
2. The size increase and, more importantly, the surface coverage induce a better (more “ordered”) structural organization of the NWs. Thus it is possible to select specific adsorbates that help in obtaining well ordered and crystallized NWs.
3. NWs grown along the $[010]$ direction and with (101) and (001) derived surfaces have a higher crystallinity than NWs grown along the $[001]$ direction and with (100) and (010) surfaces. Hence, by changing the exposed surfaces and the growth direction it is possible to tune the NW crystalline strength against variations of the size and of the surface configuration.
4. Bare and hydrated NWs show the band gap blue shift due to the size con-

finement. The band gap shift depends on the morphology since the bare NWs grown along the [010] direction do not show an appreciable variation of the gap as the NWs of comparable size elongated in the [001] direction. The band gap blue shift is a function of the crystallinity of the NW, since all the hydrated NWs have a higher shift than the respective bare counterparts.

5. The charge densities of the electronic states lying in the “bulk” band gap region are found to involve the surface atoms. Thus we expect that TiO₂ NWs show a high photocatalytic activity. The surface hydration of the NWs can tune the availability of internal channels for the transport of photoelectrons. This result can be generalized by stating that it is possible to find functionalizing adsorbates that increase the charge transport properties of the NWs conduction bands.
6. The bare NWs have VBM and CBM energies that allow, in principle, the production of H₂ and O₂ from the water splitting. This ability is found to increase on decreasing the size of the NWs elongated in the [001] direction. Thus the quantum confinement can effectively be used to enhance the photocatalytic performances of 1D TiO₂ nanostructures.
7. The surface hydroxyl groups cannot be considered as deep hole traps in the oxidation reactions of TiO₂ NWs. The O 2p electronic states of these groups have binding energies which overlap with those of the O 2p states coming from the surface region of the TiO₂ NWs.
8. Surface hydrogenation leads to occupied states at the bottom of the CBM energies of the NWs grown in the [001] direction. Thus we expect that TiO₂ NWs increase their conductance upon surface hydrogen adsorption and be designed as hydrogen sensors as already proved for TiO₂ nanotubes (Ref. [40]). However, the TiO₂ NWs sensing ability can be a function of the morphology, since the NW grown in the [010] direction does not show such occupied states.
9. At the end, we found that the surface hydration is the most stable configuration for all the NWs. This results highlights the importance of the stabilizing role

played by the terminal hydroxyl groups in the synthesis process or in the working environment of the TiO_2 NWs.

Conclusions

In this thesis we have performed first-principles DFT calculations on TiO_2 nanostructures. Firstly, we have considered zero-dimensional nanocrystals (0D NCs) with different surface coverages and then we have studied one-dimensional nanowires (1D NWs) of different size, morphology and surface termination.

In the study of 0D NCs we have modeled different synthesis conditions and typical work environments of TiO_2 nanoparticles by considering naked (free standing) NCs, hydrogen covered NCs (representative of extreme acidic conditions), and water covered NCs (moderate aqueous environments). From a thorough analysis of the experimental findings we identified the relevant ranges of variation of the main structural and electronic properties. The comparison with our calculations allowed us to interpret some controversial properties of TiO_2 NCs. The bare stoichiometric NC undergoes a global structural contraction whereas surface coverage induces volumetric expansion. The contraction of the bare NC occurs in each direction, thus the same trend is expected for TiO_2 NCs not subjected to an external pressure. On the contrary, the interaction with adsorbates produces an expansion which is more evident along the basal direction than on the (001) surfaces. This explains the observed expansion of the cell parameter a and the slight contraction of c . All the NCs show the contraction of the first shell Ti-O bond length, but only hydration leads to a 1:1 ratio of the first and second shell coordination numbers, i.e. the observed rearrangement of the Ti-O bond lengths in the octahedron. Thus, from the hydrated NC, we link these two results to two surface bonds of different nature: (i) Ti-OH bonds, with the hydroxylic radical adsorbed *on* the undercoordinated Ti of the surface, lead to short Ti-O bonds; (ii) OH, adsorbed *in* the surface of NCs as bridging groups between Ti atoms, induce long Ti-O bonds. The surface coverage

prevents a pronounced reconstruction of the surface, thus leading to a more bulk-like organization of the whole structure. In particular, the hydrated NC more closely reproduces the observed variations with respect to the bulk structural properties.

Although not unambiguously determined, the small exciton radius of TiO_2 ($0.35 < R_{ex} < 1.9$ nm) makes difficult the observation of quantum confinement effects. The diameter of our NCs is thus well suited ($2R_{NC} \sim 1$ nm) to detect such possible effects. In fact, the quantum confinement of the electronic states can be deduced from the tendency to discretization of the electronic levels and from the blue shift of the band gap. This shift and the shape of the electronic density of states depend on the NC crystallinity, since we showed that each surface coverage induces a different local and hence global spatial reconstruction. Such result agrees with recent experimental observations [67]. However the decrease of the NC dimension down to the nanoscale enhances the surface role, as well. Hence, quantum confinement effects can be hidden in presence of particular surface morphologies. For example, hydration stabilizes all the dangling bonds to higher binding energies than the valence states of the NC, whereas the chemical reduction of the same NC with hydrogen coverage induces intra-gap states.

We have found that both oxygen desorption and reduction with hydrogen of titanium atoms induce occupied electronic states in the range $0.11 - 0.40$ eV below the conduction levels. These states are Ti 3d in atomic character and are spatially localized in restricted regions of the NCs. Adsorption of oxygen decreases the number of these states from the deepest energetic levels on, similarly to the effect induced by dopamine bidentate ligands on defect sites [116]. Hence we have identified with ab-initio calculations two sources of defect states in TiO_2 NCs, which are usually detected in experimental nanosamples. Furthermore, we have found that no complete charge transfer occurs from these defect sites to the hydroxylic groups, as experimentally observed for surfaces [115], which can be an important information to take into account when dealing with expected photocatalytic performances of TiO_2 nanosamples.

From the study of 0D NCs, we have also pointed out the importance of the surface hydration in stabilizing TiO_2 NCs. This result is consistent with the experimental evidence that truncated bipyramidal NCs are characteristic of moderate acidic environments and that the first layer of water coverage on TiO_2 nanosamples

is preferentially constituted of dissociated water.

1D NWs constitute the second class of TiO_2 nanostructures studied in this thesis, through a detailed investigation of the structural and electronic properties from first-principles calculations. We have shown that these properties depend on the diameter size, on the surface coverage, and on the morphology (namely, growing direction and lateral surfaces) of the NWs. These informations can be useful to outline a theoretical background of knowledge, readily available for the experimental research on new TiO_2 nanomaterials and devices. We also proposed an interpretation of some currently debated experimental findings on TiO_2 nanostructures.

The bare NWs have an inward contraction which decreases their size whereas the surface coverage induces an outward expansion. Hence the final configuration is the result of two competing phenomena. On one hand, the own trend of TiO_2 anatase to exhibit volume reduction on decreasing the diameter size. On the other hand the presence of specific adsorbates can compensate or even reverse this trend leading to expansion, which is typical of nanoparticles shorter than 10 nm. In fact, the surface atoms are found to undergo the largest displacements depending on the kind of covering species. Thus as the size increases the effects of the surface deformations lose their weight in determining the overall configuration. The size increase and, more importantly, the surface coverage induce a better (more “ordered”) structural organization of the NWs. Thus it is possible to select specific adsorbates that help in obtaining well ordered and crystallized NWs. TiO_2 NWs grown along the [010] direction and with (101) and (001) derived surfaces have a higher crystallinity than NWs grown along the [001] direction and with (100) and (010) surfaces. Hence, by changing the exposed surfaces and the growth direction it is possible to tune the NW crystalline strength against variations of the size and of the surface

As found for 0D NCs, bare and hydrated NWs show the band gap blue shift due to the size confinement. The band gap shift depends on the morphology since the bare NWs grown along the [010] direction do not show an appreciable variation of the gap as the NWs of comparable size elongated in the [001] direction. The band gap blue shift is a function of the crystallinity of the NW, since all the hydrated NWs have a higher shift than the respective bare counterparts. The charge densities of the electronic states lying in the “bulk” band gap region are found to involve the surface atoms. Thus we expect that TiO_2 NWs show a high photocatalytic activity.

The surface hydration of the NWs can tune the availability of internal channels for the transport of photoelectrons. This result can be generalized by stating that it is possible to find functionalizing adsorbates that increase the charge transport properties of the NWs conduction bands.

The bare NWs have valence band maximum and conduction band minimum energies that allow, in principle, the production of H_2 and O_2 from the water splitting. This ability is found to increase on decreasing the size of the NWs elongated in the [001] direction. Thus the quantum confinement can effectively be used to enhance the photocatalytic performances of TiO_2 1D nanostructures.

The surface hydroxyl groups cannot be considered as deep hole traps in the oxidation reactions involving TiO_2 NWs. The O 2p electronic states of these groups have binding energies which overlap with those of the O 2p states coming from the surface region of the TiO_2 NWs. Hence, we can ascribe the experimental differences reported on the nature of the hole trap site in nanostructured TiO_2 to the competing presence of oxygens of hydroxyl terminal groups and of the surface or subsurface of TiO_2 .

Surface hydrogenation leads to occupied states at the bottom of the conduction band maximum energies of the NWs grown in the [001] direction. Thus we expect that TiO_2 NWs increase their conductance upon surface hydrogen adsorption and be designed as hydrogen sensors as already proved for TiO_2 nanotubes. However, the TiO_2 NWs sensing ability can be a function of the morphology, since the NW grown in the [010] direction does not show such occupied states. At the end, we found as in the case of TiO_2 0D NCs that the surface hydration is the most stable configuration for all the NWs. This result highlights the importance of the stabilizing role played by the terminal hydroxyl groups in the synthesis process or in the working environment of the TiO_2 NWs.

Our investigation of TiO_2 nanostructures, performed by means of DFT calculations, revealed the importance of treating explicitly the presence of adsorbates on the surface, in order to reproduce and mimic feasible configurations of TiO_2 nanomaterials in the typical conditions where they are employed. Throughout the thesis, the deep dependence of the structural and electronic properties of TiO_2 nanomaterials on the surface termination, the size, and even the morphology has gotten across. We believe that this thesis can constitute a readily available source of knowledge

and suggestions for those experimentalists interested in designing new TiO_2 nanodevices, by optimizing their performance in the very numerous ensemble of applications where TiO_2 is already applied or can potentially be.

Bibliography

- [1] B. Oregan and M. Grätzel, *Nature* **353**, 737 (1991).
- [2] M. Ni, M. K. H. Leung, D. Y.C. Leung and K. Sumathy, *Renew. Sustain. Energy Rev.* **11**, 401 (2007).
- [3] H. Sakai, R. Baba, K. Hashimoto, Y. Kubota and A. Fujishima, *Chem. Lett.* **24**, 185 (1995).
- [4] A. Fujishima, T.N. Rao and D.A. Tryk, *J. Photochem. Photobiol. C: Photochem. Rev.* **1**, 1 (2000).
- [5] I. Poullos, P. Spathis and P. Tsoumparis, *J. Environ. Sci. Health* **34**, 1455 (1999).
- [6] P.-C. Maness, S. Smolinski and W.A. Jacoby, *Appl. Environ. Microbiol.* **65**, 4094 (1999).
- [7] T. L. Thompson and J. T. Yates Jr., *Chem. Rev.* **106**, 4428 (2006).
- [8] X. Chen and S. S. Mao, *Chem. Rev.* **107**, 2891 (2007).
- [9] U. Diebold, *Surf. Sci. Rep.* **48**, 53 (2003).
- [10] O. Carp, C. L. Huisman and A. Reller, *Prog. Solid State Chem.* **32**, 33 (2004).
- [11] M. Fernández-García, A. Martínez-Arias, J. C.Hanson and J. A. Rodriguez, *Chem. Rev.* **104**, 4063 (2004).
- [12] V. Luca, *J. Phys. Chem. C* **113**, 6367 (2009).

- [13] V. Swamy, D. Menzies, B. C. Muddle, A. Kuznetsov, L. S. Dubrovinsky, Q. Dai and V. Dmitriev, *Appl. Phys. Lett.* **88**, 243103 (2006).
- [14] L. X. Chen, T. Rajh, Z. Wang and M. C. Thurnauer, *J. Phys. Chem. B* **101**, 10688 (1997).
- [15] L. X. Chen, Tijana Rajh, W. Jäger, J. Nedeljkovic and M. C. Thurnauer, *J. Sync. Radiat.* **6**, 445 (1999).
- [16] V. Luca, S. Djajanti and R. F. Howe, *J. Phys. Chem. B* **102**, 10650 (1998).
- [17] K. L. Yeung, A. J. Maira, J. Stolz, E. Hung, N. K. Ho, A. C. Wei, J. Soria, K. Chao and P. L. Yue, *J. Phys. Chem. B* **106**, 4608 (2002).
- [18] K. L. Yeung, S. T. Yau, A. J. Maira, J. M. Coronado, J. Soria and P. L. Yue, *J. Catal.* **219**, 107 (2003).
- [19] T. Rajh, L. X. Chen, K. Lukas, T. Liu, M. C. Thurnauer and D. M. Tiede, *J. Phys. Chem. B* **106**, 10543 (2002).
- [20] K.J. Hameeuw, G. Cantele, D. Ninno, F. Trani, G. Iadonisi, *J. Chem. Phys.* **124**, 024708 (2006).
- [21] M. Niederberger, M. H. Bart and G. D. Stucky, *Chem. Mater.* **14**, 4364 (2002).
- [22] N. Serpone, D. Lawless and R. Khairutdinov, *J. Phys. Chem.* **99**, (1995).
- [23] S. Monticone, R. Tufeu, A. V. Kanaev, E. Scolan and C. Sanchez, *Appl. Surf. Sci.* **162-163**, 565 (2000).
- [24] K. M. Reddy, S. V. Manorama and A. R. Reddy, *Mater. Chem. Phys.* **78**, 239 (2002).
- [25] L. Zhao and J. Yu, *J. Colloid Interface Sci.* **304**, 84 (2006).
- [26] T. Toyoda and I. Tsuboya, *Rev. Sci. Instrum.* **74**, 782 (2003).
- [27] A. Fujishima, T. N. Rao and D. A. Tryk, *J. Photochem. Photobiol. C* **1**, 1 (2000).

- [28] J. Soria, J. Sanz, I. Sobrados, J. M. Coronado, A. J. Maira, M. D. Hernández-Alonso and F. Fresno, *J. Phys. Chem. C* **111**, 10590 (2007).
- [29] D. A. Panayotov and J. T. Yates Jr., *Chem. Phys. Lett.* **436**, 204 (2007).
- [30] T. Berger, O. Diwald, E. Knözinger, F. Napoli, M. Chiesa and E. Giamello, *Chem. Phys.* **339**, 138 (2007).
- [31] M. Adachi, Y. Murata, J. Takao, J. Jiu, M. Sakamoto and F. Wang, *J. Am. Chem. Soc.* **126**, 14943 (2004).
- [32] Y. Mao, M. Kanungo, T. Hemraj-Benny and S. S. Wong, *J. Phys. Chem. B* **110**, 702 (2006).
- [33] B. Koo, J. Park, Y. Kim, S.-H. Choi, Y.-E. Sung and T. Hyeon, *J. Phys. Chem. B* **110** 2006.
- [34] S. Limmer and G. Cao, *Adv. Mater.* **15**, 427 (2003).
- [35] G. Centi and S. Perathoner, *Catal.* **20**, 367 (2007).
- [36] A. N. Enyashin and G. Seifert, *Phys. Stat. Sol. (b)* **242**, 1361 (2005).
- [37] F. Alvarez-Ramirez and Y. Ruiz-Morales, *Chem. Mater.* **19**, 2947 (2007).
- [38] D. Zhang, P. Liu and C. Liu, *J. Phys. Chem. C* **112**, 16729 (2008).
- [39] S. Meng, J. Ren and E. Kaxiras **8**, 3266 (2008).
- [40] O. K. Varghese, D. Gong, M. Paulose, K. G. Ong, E. C. Dickey and C. A. grimes, *Adv. Mater.* **15**, 624 (2003).
- [41] F. Fabregat-Santiago, E. M. Barea, J. Bisquert, G. K. Mor, K. Shankar and C. A. Crimes, *J. Am. Chem. Soc.* **130**, 11312 (2008).
- [42] V. V. Sysoev, B. K. Button, K. Wepsiec, S. Dmitriev and A. Kolmakov, *Nano Lett.* **6**, 1584 (2006).
- [43] G. K. Mor, O. K. Varghese, M. Paulose, K. Shankar and C. A. Grimes, *Sol. Energy Mater. Sol. Cells* **90**, 2011 (2006).

- [44] M. Paulose, O. K. Varghese, G. K. Mor, C. A. Grimes and K. G. Ong, *Nanotechnology* **17**, 398 (2006).
- [45] O. K. Varghese, D. Gong, M. Paulose, K. G. Ong and C. A. Craig, *Sensors and Actuators B* **93**, 338 (2003).
- [46] M. Born and J. R. Oppenheimer, *Ann. Phys. (Leipzig)* **84**, 457 (1927).
- [47] P. Hohenberg and W. Kohn, *Phys. Rev.* **136**, B864 (1964).
- [48] W. Kohn and L. Sham, *Phys. Rev.* **104**, A1133 (1965).
- [49] N. W. Ashcroft and N. D. Mermin, *Solid State Physics*, Holt Saunders Philadelphia (1976).
- [50] J. P. Perdew, in *Electronic Structure of Solids 91*, Ed. P. Ziesche and H. Eschrig (Akademie Verlag, Berlin, 1991) p. 11.
- [51] P. Giannozzi, S. Baroni, N. Bonini, M. Calandra, R. Car, C. Cavazzoni, D. Ceresoli, G.L. Chiarotti, M. Cococcioni, I. Dabo, A. Dal Corso, S. Fabris, G. Fratesi, S. de Gironcoli, R. Gebauer, U. Gerstmann, C. Gougoussis, A. Kokalj, M. Lazzeri, L. Martin-Samos, N. Marzari, F. Mauri, R. Mazzarello, S. Paolini, A. Pasquarello, L. Paulatto, C. Sbraccia, S. Scandolo, G. Sclauzero, A. P. Seitsonen, A. Smogunov, P. Umari, and R. M. Wentzcovitch, *J. Phys.: Condens. Matt.* **21**, 395502 (2009).
- [52] D. Vanderbilt, *Phys. Rev. B* **41**, 7892 (1990).
- [53] P. R. Feynman, *Phys. Rev.* **56**, 340 (1939).
- [54] B. G. Pfrommer, B. Cot, S. G. Louie, and M. L. Cohen, *J. Comput. Phys.* **131** 233 (1997).
- [55] C. Burda, X. Chen, R. Narayanan and M. A. El-Sayed, *Chem. Rev.* **105**, 1025 (2005).
- [56] J. C. Lu, P. Chang and Z. Fan, *Mater. Sci. Eng. R* **52**, 49 (2006).

- [57] J. Polleux, N. Pinna, M. Antonietti, C. Hess, U. Wild, R. Schlögl and M. Niederberger, *Chem. Eur. J.* **11**, 3541 (2005).
- [58] C. Liu and S. Yang, *Am. Chem. Soc. Nano* **3**, 1025 (2009).
- [59] T. Sugimoto, X. Zhou and A. Muramatsu, *J. Colloid Int. Sci.* **259**, 53 (2003).
- [60] H. Zhang, M. Finnegan and J. F. Banfield, *Nano Lett.* **1**, 81 (2001).
- [61] C. H. Cho, M. H. Han, D. H. Kim and D. K. Kim, *Mater. Chem. Phys.* **92**, 104 (2005).
- [62] S. Han, S.-H. Choi, S.-S. Kim, M. Cho, B. Jang, D.-Y. Kim, J. Yoon and T. Hyeon, *small* **1**, 812 (2005).
- [63] Y. Gao and S. A. Elder, *Mater. Lett.* **44**, 228 (2000).
- [64] S. Yang and L. Gao, *J. Am. Ceram. Soc.* **88**, 968 (2005).
- [65] G. Li, L. Li, J. Boerio-Goates and B. F. Woodfield, *J. Am. Chem. Soc.* **127**, 8659 (2005).
- [66] H. Zhang and J. F. Banfield, *J. Phys. Chem. B* **104**, 3481 (2000).
- [67] N. Satoh, T. Nakashima, K. Kamiruka and K. Yamamoto, *Nature* **3**, 106 (2008).
- [68] R. F. Egerton, *Physical Principles of Electron Microscopy*, Springer New York (2005).
- [69] G. Vlaic and L. Olivi, *Croat. Chem. Acta* **77**, 427 (2004).
- [70] F.-T. Chau, Y.-Z. Liang, J. Gao and X.-G. Shao, *Chemometrics*, Wiley-Interscience Hoboken (2004).
- [71] T. Bezrodna, G. Puchkovska, V. Shymanovska, J. Baran and H. Ratajczak, *J. Mol. Struct.* **700**, 175 (2004).
- [72] T. Bezrodna, G. Puchkovska, V. Shymanovska, I. Chashechnikova, T. Khalyavka and J. Baran, *Appl. Surf. Sci.* **214**, 222 (2003).

- [73] D. A. Panayotov and J. T. Yates Jr., Chem. Phys. Lett. **410**, 11 (2005).
- [74] A. A. Levchenko, G. Li, J. Boerio-Goates, B. F. Woodfield and A. Navrotsky, Chem. Mater. **18**, 6324 (2006).
- [75] C. Kormann, D. W. Bahnemann and M. R. Hoffmann, J. Phys. Chem. **92**, 5196 (1988).
- [76] M. Anpo, T. Shima, S. Kodama and Y. Kubokawa, J. Phys. Chem. **91**, 4305 (1987).
- [77] A. H. Yuwono, J. Xue, J. Wang, H. I. Elim, W. Ji, Y. Li and T. J. White, J. Mater. Chem. **13**, 1475 (2003).
- [78] D. Pan, N. Zhao, Q. Wang, S. Jiang, X. Ji and L. An, Adv. Mater. **17**, 1991 (2005).
- [79] J. Joo, S. G. Kwon, T. Yu, M. Cho, J. Lee, J. Yoon and T. Hyeon, J. Phys. Chem. B **109**, 15297 (2005).
- [80] Y. Lei, L. D. Zhang and J. C. Fan, Chem. Phys. Lett, **338**, 231 (2001).
- [81] K. Das, S. K. Panda and S. Chaudhuri, J. Cryst. Grow. **310**, 3792 (2008).
- [82] T. Berger, M. Sterrer, O. Diwald, E. Knözinger, D. Panayotov, T. L. Thompson and J. T. Yates Jr., J. Phys. Chem. B **109**, 6061 (2005).
- [83] A. Fujishima, X. Zhang and D. A. Tryk, Surf. Sci. Rep. **63**, 515 (2008).
- [84] N. Serpone, D. Lawless, R. Khairutdinov and E. Pelizzetti, J. Phys. Chem. **99**, 16655 (1995).
- [85] D. Lawless, N. Serpone and D. Meisel, J. Phys. Chem. **95**, 5166 (1991).
- [86] R. F. Howe and M. Grätzel, J. Phys. Chem. **91**, 3906 (1987).
- [87] O. I. Micic, Y. Zhang, K. R. Cromack, A. D. Trfunac and M. C. Thurnauer, J. Phys. Chem. **97**, 7277 (1993).

- [88] P. Salvador, J. Phys. Chem. C **111**, 17038 (2007).
- [89] A. S. Barnard and L. A. Curtiss, Nano Lett. **5**, 1261 (2005).
- [90] J. Wu, S. Hao, J. Lin, M. Huang, Y. Huang, Z. Lan and P. Li, Cryst. Growth & Des. **8**, 247 (2008).
- [91] P. Persson, J. C. M. Gebhardt and S. Lunell, J. Phys. Chem. B **107**, 3336 (2003).
- [92] A. S. Barnard, S. Erdin, Y. Lin, P. Zapol and J. W. Halley, Phys. Rev. B **73**, 205405 (2006).
- [93] W. F. Zhang, M. S. Zhang, Z. Yin and Q. Chen, Appl. Phys. B **70**, 261 (2000).
- [94] I. Nakamura, N. Negishi, S. Kutsuna, T. Ihara, S. Sugihara and K. Takeuchi, J. Mol. Catal. A: Chem. **161**, 205 (2000).
- [95] M. Ni, M.K.H. Leung, D.Y.C. Leung and K. Sumathy, Renew. Sustainable Energy Rev. **11**, 401 (2007).
- [96] J. P. Perdew and Y. Wang, Phys. Rev. B **45**, 13244 (1992).
- [97] A. Mordecai, *Nonlinear Programming: Analysis and Methods*, Dover Publishing, 2003.
- [98] J. K. Burdett, T. Hughbanks, G. J. Miller, J. W. Richardson Jr. and J. V. Smith, J. Am. Chem. Soc. **109**, 12 (1987).
- [99] A. Iacomino, G. Cantele, D. Ninno, I. Marri and S. Ossicini, Phys. Rev. B **78**, 075405 (2008).
- [100] S. Dzwigaj, C. Arrouvel, M. Breysse, C. Geantet, S. Inoue, H. Toulhoat and P. Raybaud, J. Catal. **236**, 245 (2005).
- [101] A. S. Barnard and P. Zapol, Phys. Rev. B **70**, 235403 (2004).
- [102] M. J. Lundqvist, M. Nilsing, P. Persson and S. Lunell, Int. J. Quantum Chem. **106**, 3214 (2006).

- [103] H. C. Choi, Y. M. Jung and S. B. Kim, *Vib. Spectrosc.* **37**, 33 (2005).
- [104] S. Erdin, You Lin, J. W. Halley, P. Zapol, P. Redfern and L. Curtiss, *J. Electroanal. Chem.* **607**, 147 (2007).
- [105] M. Fernández-García, X. Wang, C. Belver, J. C. Hanson and J. A. Rodriguez, *J. Phys. Chem. C* **111**, 674 (2007).
- [106] V. N. Koparde and P. T. Cummings, *J. Phys. Chem. C* **111**, 6920 (2007).
- [107] A. G. Thomas, W. R. Flavell, A. K. Mallick, A. R. Kumarasinghe, D. Tsoutsou, N. Khan, R. L. Stockbauer, S. Warren, T. K. Johal, S. Patel, D. Holland, A. Taleb and F. Wiame, *Phys. Rev. B* **75**, 035105 (2007).
- [108] R. Sanjinés, H. Tang, H. Berger, F. Gozzo, G. Margaritondo and F. Lévi, *J. Appl. Phys.* **75**, 2945 (1994).
- [109] Ming-Yu Kuo, C-L Chen, C-Y Hua, H-C Yang and P. Shen, *J. Phys. Chem. B* **109**, 8693 (2005).
- [110] A. Iacomino, G. Cantele, F. Trani, D. Ninno, I. Marri and S. Ossicini, accepted by 2009 MRS Spring Meeting Proceedings.
- [111] S. H. Szczepankiewicz, A. J. Colussi and M. R. Hoffmann, *J. Phys. Chem. B* **104**, 9842 (2000).
- [112] S. Leytner and J. T. Hupp, *Chem. Phys. Lett.* **330**, 231 (2000).
- [113] S. H. Szczepankiewicz, J. A. Moss and M. R. Hoffmann, *J. Phys. Chem. B* **106**, 7654 (2002).
- [114] T. Yoshihara, R. Katoh, A. Furube, Y. Tamaki, M. Murai, K. Hara, S. Murata, H. Arakawa and M. Tachiya, *J. Phys. Chem. B* **108**, 3817 (2004).
- [115] M. A. Henderson, W. S. Epling, C. H. F. Peden and C. L. Perkins, *J. Phys. Chem. B* **107**, 534 (2003).
- [116] L. de la Garza, Z. V. Saponjic, N. M. Dimitrijevic, M. C. Thurnauer and T. Rajh, *J. Phys. Chem. B* **110**, 680 (2006).

- [117] G. Makov and M. C. Payne, Phys. Rev. B **51**, 4014 (1995).
- [118] Z-W. Qu and G-J. Kroes, J. Phys. Chem. C **111**, 16808 (2007).
- [119] H-J. Zhai and L-S. Wang, J. Am. Chem. Soc. **129**, 3022 (2007).
- [120] H. Yu, J. Yu and B. Cheng, J. Mol. Catal. A: Chem. **253**, 99 (2006).
- [121] Q. Wang, Z. Wen and J. Li, Inorg. Chem. **45**, 6944 (2006).
- [122] M. Kitano, R. Mitsui, D. R. Eddy, Z. M. A. El-Bahy, M. Matsuoka, M. Ueshima and M. Anpo, Catal. Lett. **119**, 217 (2007).
- [123] X. Feng, K. Shankar, O. K. Varghese, M. Paulose, T. J. Latempa and C. A. Grimes, Nano Lett. **8**, 3781 (2008).
- [124] K Yu, J. Zhao, X. Zhao, X. Ding, Y. Zhu and Z. Wang, Mater. Lett. **59**, 2676 (2005).
- [125] V. G. Pol, Y. Langzam and A. Zaban, Langmuir **23**, 11211 (2007).
- [126] A. S. Attar, M. S. Ghamsari, F. Hajiesmaeilbaigi, S. Mirdamadi, K. Katagiri and K. Koumoto, J. Phys. D: Appl. Phys. **41**, 155318 (2008).
- [127] H.-S. Shim, S.-I. Na, S. H. Nam, H.-J. Ahn, H. J. Kim, D.-Y. Kim and W. B. Kim, Appl. Phys. Lett. **92**, 183107 (2008).
- [128] M. Dürr, A. Schmid, M. Obermaier, S. Rosselli, A. Yasuda and G. Nelles, Nat. Mater. **4**, 607 (2005).
- [129] B. Tan and Y. Wu, J. Phys. Chem. B **110**, 15932 (2006).
- [130] S. H. Kang, S.-H. Choi, M.-S. Kang, J.-Y. Kim, H.-S. Kim, T. Hyeon and Y.-E. Sung, Adv. Mater. **20**, 54 (2008).
- [131] K. Zhu, T. B. Vinzant, N. R. Neale and A. J. Frank, Nano Lett. **7**, 3739 (2007).
- [132] R. Wang, C. Ruan, D. Kanayeva, K. Lassiter and Y. Li, Nano Lett. **8**, 2625 (2008).

- [133] P. B. Allen, Nano Lett. **7**, 6 (2007).
- [134] J. Jiu, S. Isoda, F. Wang and M. Adachi, J. Phys. Chem. B **110**, 2087 (2006).
- [135] J. Polleux, N. Pinna, M. Antonietti and M. Niederberger, Adv. Mater. **16**, 436 (2004).
- [136] Q. Wei, K. Hirota, K. Tajima and K. Hashimoto, Chem. Mater. **18**, 5080 (2006).
- [137] W. Daoud and G. K. H. Pang, J. Phys. Chem. B **110**, 25746 (2006).
- [138] T. Berger, T. Lana-Villarreal, D. Monllor-Satoca and R. Gómez, J. Phys. Chem. C **112**, 15920 (2008).
- [139] L. X. Chen, T. Rajh, Z. Wang and M. C. Thurnauer, J. Phys. Chem. B **101**, 10688 (1997).
- [140] S. U. M. Khan and T. Sultana, Sol. Energy Mater. Sol. Cells **76**, 211 (2003).
- [141] J. Jitputti, Y. Suzuki and S. Yoshikawa, Catal. Comm. **9**, 1265 (2008).
- [142] F. Dong, W. Zhao and Z. Wu, Nanotechnology **19**, 365607 (2008).
- [143] H. J. Monkhorst and J. D. Pack, Phys. Rev. B **13**, 5188 (1976).
- [144] A. Iacomino, G. Cantele, F. Trani and D. Ninno, Submitted to J. Phys. Chem. C.
- [145] V. Shklover, M.-K. Nazeeruddin, S. M. Zakeeruddin, C. Barbé, A. Kay, T. Haibach, W. Steurer, R. Hermann, H.-U. Nissen and M. Grätzel, Chem. Mater. **9**, 430 (1997).
- [146] J.-N. Nian and H. Teng, J. Phys. Chem. B **110**, 4193 (2006).
- [147] P. Wen, H. Itoh, W. Tang and Q. Feng, Langmuir **23**, 11782 (2007).
- [148] G. Caputo, C. Nobile, T. Kipp, L. Blasi, V. Grillo, E. Carlino, L. Manna, R. Cingolani, P. D. Cozzoli and A. Athanassiou, J. Phys. Chem. C **112**, 701 (2008).

- [149] A. S. Barnard and P. Zapol, Phys. Rev. B **70**, 235403 (2004).
- [150] S.-D. Mo and W. Y. Ching, Phys. Rev. B **51**, 13023 (1995).
- [151] R. Asahi, Y. Taga, W. Mannstadt and A. J. Freeman, Phys. Rev. B **61**, 7459 (2000).
- [152] L. Thulin and J. Guerra, Phys. Rev. B **77**, 195112 (2008).
- [153] J. H. Snook, L. A. Samuelson, J. Kumar, Y.-G. Kim and J. E. Whitten, Org. Electron. **6**, 55 (2005).
- [154] Y.-T. Lin, T.-W. Zeng, W.-Z. Lai, C.-W. Chen, Y.-Y. Lin, Y.-S. Chang and W.-F. Su, Nanotechnology **17**, 5781 (2006).
- [155] A. Petrella, M. Tamborra, M. L. Curri, P. Cosma, M. Striccoli, P. D. Cozzoli and A. Agostiano, J. Phys. Chem. B **109**, 1554 (2005).
- [156] L. Kavan, M. Grätzel, S. E. Gilbert, C. Klemenz and H. J. Scheel, J. Am. Chem. Soc. **118**, 6716 (1996).
- [157] F. M. Hossain, L. Sheppard, J. Nowotny and G. E. Murch, J. Phys. Chem. Solids **69**, 1820 (2008).
- [158] N. Umezawa, A. Janotti, P. Rinke, T. Chikyow and C. G. Van de Walle, Appl. Phys. Lett. **92**, 041104 (2008).
- [159] M. Grätzel, Nature **414**, 338 (2001).
- [160] L. A. Lyon and J. T. Hupp, J. Phys. Chem. B **103**, 4623 (1999).